UNIVERSITÀ DEGLI STUDI DI ROMA "TOR VERGATA"

FACOLTA' DI SCIENZE MATEMATICHE NATURALI E FISICHE

DOTTORATO DI RICERCA IN FISICA

XXI CICLO

Cadmium Sulfide Quantum Dots: Growth and Optical Properties

Silvano Del Gobbo

A.A. 2008/2009

Docente Guida/Tutor: Prof. Wolfgang Richter

Coordinatore: Prof. Piergiorgio Picozza

Contents

Chapter 1

Introduction

In recent years, there has been a rapid development of the growth techniques of nanostructured materials, and a particular breakthrough was given by the introduction of colloidal growth techniques [1]. These techniques allow to grow by affordable facilities a wide range of nanostructured materials, metals and semiconductors, with high crystallinity, reduced size and with narrow size distribution. The availability of such materials has drawn many attention of the research which is actually focusing the efforts in view of their future technological applications.
In this thesis, the optoelectronic and optovibrational properties of cadmium sulfide quantum dots are studied. Nanostructured CdS has promising future applications as in the realization of optoelectronic devices such as tunable light emitting diodes [2], and in the realization of new high efficiency solar cells, usually in coupling with other materials (TiO_2 or organic molecules) [3, 4]. Moreover, nanostructured cadmium sulfide functionalized with bio-molecules was already successfully used as fluorescent probe in biology in substitution of the molecular fluorescent probes [5]. However, in order to fully exploit the potential technological applications, the study of the physical properties of such materials is of crucial importance.
Optical spectroscopies, electron microscopies (SEM and TEM) and X-ray diffraction are the most common used techniques to investigate semiconductor quantum dots. In this study, optical and electron transmission microscopies are used to probe the morphology of the material, while the optical techniques of absorbance and photoluminescence spectroscopies are used to investigate the electronic properties. The vibrational properties are studied instead by Raman spectroscopy. Due to the diffraction limits, the spatial resolution of the optical spectroscopies is limited to a few hundreds of nanometers. Therefore, the spatial resolution is not sufficient to probe a single nanostructure in a sample containing many closely packed nanostructures and the collected optical signal will be averaged over many nanostructures according to their size distribution. However, to have a well defined and narrow size distribution will be very helpful in the interpretation of the spectra. By the means of colloidal growth [1], it is possible to grow quantum dots with a sufficiently narrow size distribution. The growth of cadmium sulfide (CdS) quantum dots developed here consists in the thermolysis ($\sim$260 °C) of cadmium stearate in presence of hydrogen sulfide in a high temperature boiling point solvent 1-octadecene (1-ODE). The growth is regulated by the presence of the surfactating molecule trioctylphosphine oxide (TOPO). The TOPO molecules bind covalently on nanocrystal surface creating a hydrophobic coating shell preventing from a too rapid growth, from their coalescence and makes them solvable in the organic solvent (1-ODE). Nanocrystals with a determined size and a narrow size distribution can be obtained properly adjusting the growth parameters such as temperature, precursors concentrations, and principally the surfactant concentration and reaction time. This

method is used to grow several sets of quantum dots samples with different sizes.
The electronic properties of CdS quantum dots are studied by optical absorption and photoluminescence spectroscopies. By absorption spectroscopy, information regarding the electronic states in quantum dots can be obtained. Moreover, exploiting the relation existing between band gap and quantum dot radius [6], from the energy of the first absorption transition it is possible to determine the mean diameter of the quantum dots. The emissive properties of the quantum dots are probed by photoluminescence spectroscopy and from the energy of PL band (band-gap transition) an estimation of the nanoparticles diameter can be obtained. Based on the width of absorbance and photoluminescence bands, the width of nanoparticles size distributions can be estimated also.
The nanostructures morphology, size and size distribution is determined by TEM microscopy. The lower resolution images are used to measure the diameter of a large number of nanoparticles in order perform a statistical analysis. In this way the mean diameter and the width of the size distribution can be obtained.
The main goal of the work is the study of vibrational properties of CdS quantum dots by Raman spectroscopy. So far, only few theoretical models have been developed to explain the quantum confinement of phonons in nanostructures. At the same time, not much experiments have been carried out for the same purpose. For computational reasons, the calculations of lattice dynamics by a direct approach are restricted, to very small quantum dots only [7, 8], hence, models based on a macroscopic approach are often preferred. The models based on a macroscopic approach are commonly known as dielectric continuum model [9]. Due to the elevated surface-volume ratio, in Raman spectra of nanostructures there is an important contribution of the surface modes. Surface modes have been also described by a similar macroscopic approach [10]. Finally, we can cite the $\vec{q}$ relaxation model [11] which is a semiempirical model used to explain the asymmetry of the peaks, but it can not explain the apparition of multiple peaks features. These models remains however only modellizations, and they still need an experimental verification. Experimentally, the phonon quantum confinement in these materials have been already investigated by Raman spectroscopy. In older publications, Raman scattering measurements were performed mainly on II-VI quantum dots embedded in glassy matrix [12–16]. While, more recently, Raman investigations were carried out on II-VI quantum dots embedded in polymeric [17] or in gelatin matrix [18, 19]. Very few reports on Raman measurements performed directly on powder-like quantum dots are instead available [20, 21]. However, the largest part of the studies were done mainly on CdSe quantum dots since easier to grow with the standard methods, or on ternary II-VI or core/shell II-VI quantum dots because more relevant from the technological point of view.
To carry out a systematic study of the vibrational properties of quantum dots by Raman spectroscopy, several CdS quantum dots samples are purposely grown with different average sizes. The as grown and successively purified quantum dots samples, have a gel-like consistence due to the TOPO coating layer. Therefore they are not very suitable to a spectroscopic study by μ-Raman, and for this reason it is necessary to replace the TOPO layer by another type of molecules. For this purpose, the thioglycolic acid (TGA) seems to be the suitable molecule. The TGA-coating layer makes the CdS quantum dots hydrophillic and with a powder-like consistence. To avoid thermal effects or even damage of the samples, the μ-Raman measurements must be performed using very low laser powers (on the sample).
In the Raman spectra of CdS quantum dots, a decrease (red-shift) of the phonon frequency with respect to the bulk CdS frequency is expected. In particular, the red-shift is expected to be more pronounced for the smallest quantum dots, while at the size increase of nanocrystals, the

phonon frequency will approach progressively to the bulk value. This red-shift is caused by the lattice expansion and by a subsequent weakening of the bonds which causes a reduction of the resonance frequency. Beyond the red-shift, the quantum confinement is visible as an asymmetric broadening of the phonon line and by the apparition of a new peak 20-30 wavenumbers lower than LO peak. Some reports assign this peak to surface modes [22–24]. Other reports describe this mode instead as a consequence of new selection rules arising from the reduced dimensionality [20, 25]. Both the interpretations can be considered correct since the distinction between surface and bulk in nanocrystals is rather small. The experiments have the aim to cross check the predictions based on the dielectric continuum model and on the surface phonon theory with the experimental results. According to [17, 23, 24], a surface mode at $\sim$270 cm^{-1} is expected in the Raman spectra of CdS quantum dots. A comparison between the experimental and theoretical surface mode frequency will be carry out, moreover, a relation between surface mode and the size of the nanoparticle will be investigated.
In conclusion, the goal of this thesis work is to develop a method to grow CdS quantum dots with the wanted physical characteristics (e.g. narrow size distribution) suitable for a systematic study of vibrational properties.

Chapter 2

Structural and Physical Properties of Cadmium Sulfide

2.1 Structural Properties

Cadmium sulfide can crystallize in four different crystalline structures; the hexagonal structure (wurtzite), the cubic structure (zinc blende), the cubic rock salt structure and the distorted rock salt structure. Among these four crystalline structures, the wurtzite, which can be found in nature as rare Greenockite mineral is the thermodynamically most stable and thus the most common. CdS with zinc-blende modification is a metastable structure [26], however it can be still found in nature as the as much rare mineral Hawleyite. The rock salt modification can exist only under high pressure condition, i.e. subjecting the hexagonal CdS to pressures ranging from 2.6 to 4.2 GPa. At this pressure the two modifications coexist [27]. At higher pressure, the rock salt structure transforms into the KCN-like distorted rock salt structure having $Pmmm$ symmetry. These two last modifications coexist in a hydrostatic pressure ranging from 60 to 68 GPa [28]. The two most important crystalline structures, i.e. the wurtzite and the zinc blende structures are shown in the figures 2.1.

Modifications	space group		Lattice parameters (Å)
	(Hermann-Mauguin)	(Schönflies)	
Wurtzite	$P63mc$	C_{6v}^4	$a = 4.1348$, $c = 6.7490$
Zinc blende	$F\bar{4}3m$	T_d^2	$a = 5.818$
Rock salt	$Fm\bar{3}m$	O_h^5	$a = 5.32$
Dist. rock salt	$Pmmn$	D_{2h}^1	$a = 3.471(8)$, $b = 4.873(7)$, $c = 3.399(7)$

Table 2.1: *Space groups in international crystallographic notation (Hermann-Mauguin) and Schönflies notation relative to the four lattice modifications. The crystallographic parameters are taken from [28, 29] (X-ray diffraction data).*

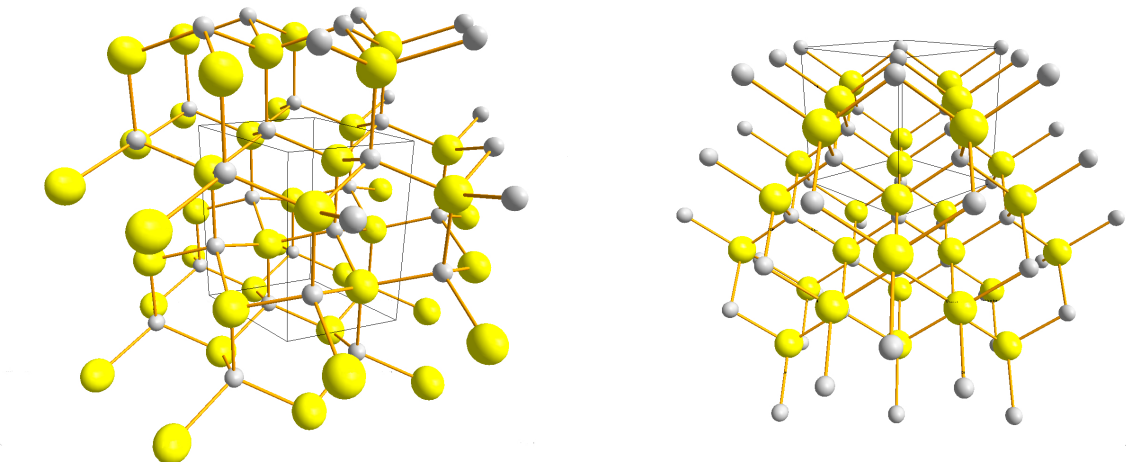

Figure 2.1: *Pictures of hexagonal wurtzite (left) and zinc-blende (right) cadmium sulfide crystalline structures elaborated from crystallographic data taken from [28, 29]. The grey spheres represent the cadmium atoms while the yellow spheres the sulfur atoms. The hexagonal and cubic elemental cells are the boxes traced with dashed lines.*

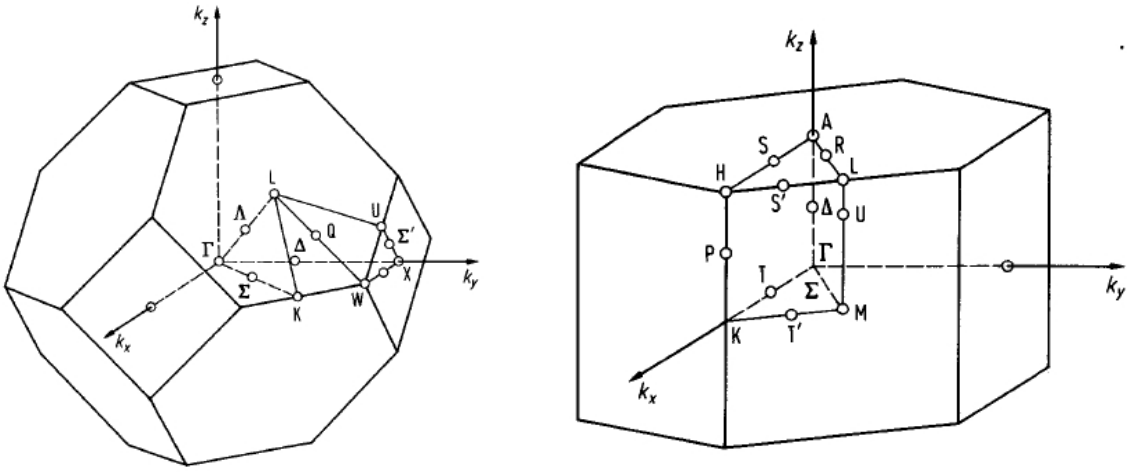

Figure 2.2: *Brillouin zone of zinc-blende (left) and wurtzite (right) lattice with the highest symmetry directions depicted by capital letters*

2.2 Electronic Properties

Cadmium sulfide in both in hexagonal (Wurtzite) either in cubic modification (zinc blende) is a direct band gap semiconductor with the smallest bad gap at the center of the Brillouin zone Γ, see figures 2.3 and 2.4. In the hexagonal allotropic modification, the topmost valence band Γ_5 + Γ_1 due to crystal field perturbation and spin-orbit coupling is split into three spin-degenerate states Γ_9, Γ_7 and Γ_7 [30, 31]. Therefore there are three possible optical transitions at E_{g0}, $\Gamma_{9V} \rightarrow \Gamma_{7C}$ (2.5537 eV), $\Gamma_{7C} \rightarrow \Gamma_{7V}$ (2.5686 eV), $\Gamma_{7C} \rightarrow \Gamma_{7V}$ (2.632 eV). In the cubic modification, the effect due to crystal field perturbation is much less relevant. Neglecting the spin-orbit interaction, at Γ point the conduction band is constituted by the non degenerated state Γ_{1c}, while the valence band by a twofold-degenerated state Γ_{5v} and a non degenerate state Γ_{1v}. Such levels give rise to a single optical transition $\Gamma_{1C} \rightarrow \Gamma_{15c}$ [32]. Including the spin-orbit interaction, the sixfold degenerated valence band is split into fourfold-degenerated states with $J = 3/2$ (Γ_8) and other twofold-degenerated states with $J = 1/2$ (Γ_7). The two levels are separated by the spin-orbit split Δ [33]. In hexagonal CdS, the main bang gap relative to the transition between the critical points $\Gamma_{9V} - \Gamma_{7C}$ is of 2.4812 eV. This value has been obtained by optical ellipsometry measurements [31]. By density functional theory calculations, in the local density approximation, using a self-interaction-corrected pseudopotentials [34], a band gap value of 2.5 eV is obtained. Measurements performed on cubic CdS give, for the main band gap (transition $\Gamma_{1V} \rightarrow \Gamma_{15C}$) a value of 2.48 eV at 1.8 K [32], while, always from the same kind of LDA calculation used for hexagonal CdS [34], the calculated band gap is of 2.4 eV.

Even though the physical properties of the CdS in cubic modification are interesting from the physical point of view, they will not be dealt henceforth, and the interest will be focused exclusively on the hexagonal CdS.

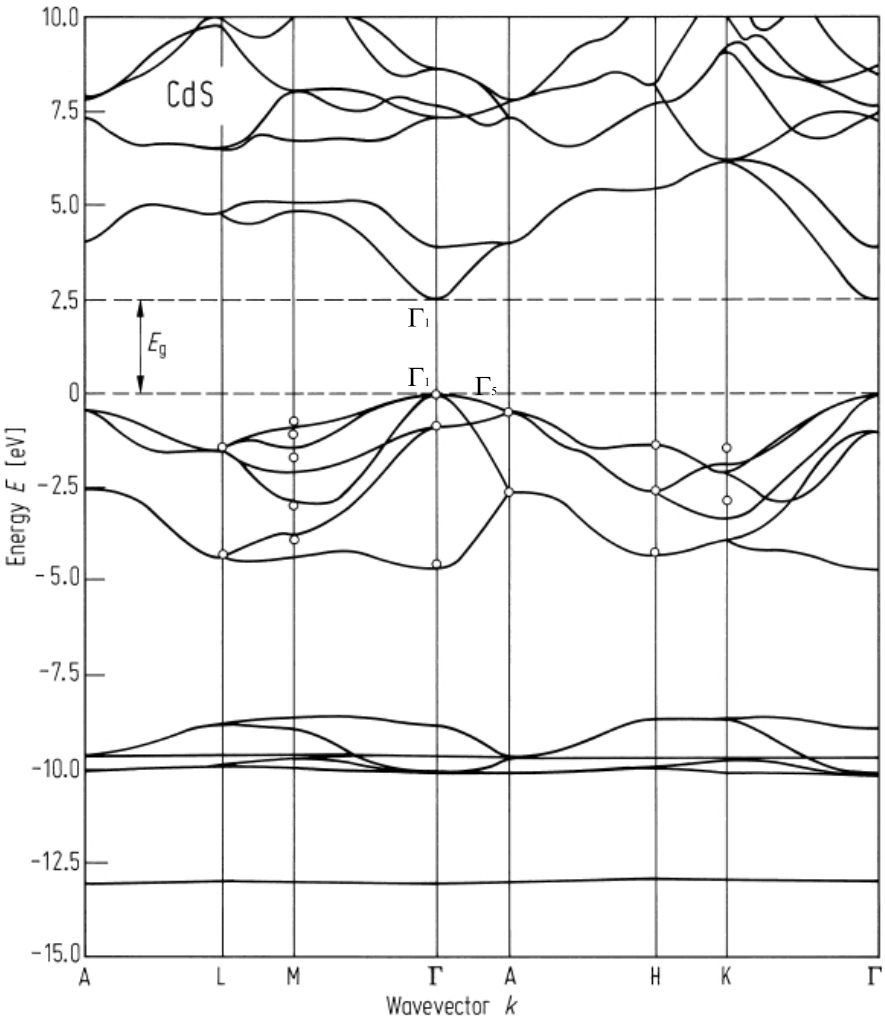

Figure 2.3: *Wurtzite CdS electronic band structure calculated by density function theory (DFT) in the self interaction corrected local density approximation (LDA) [34]. Notice that critical points of the smallest band gap E_{g0} are indicated by Γ_1 and Γ_5 symbols instead of Γ_9 and Γ_7 since the spin-orbit interaction is here neglected.*

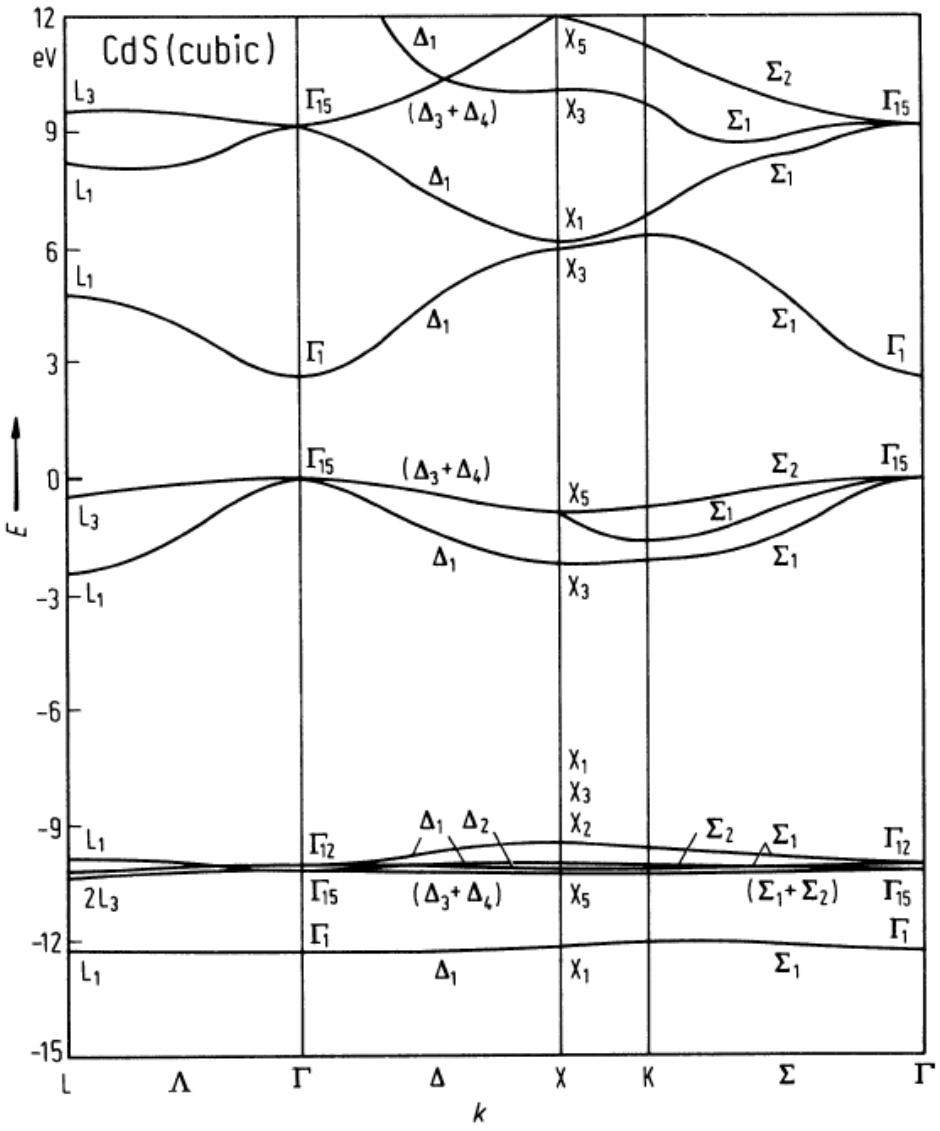

Figure 2.4: *Zinc-blende CdS electronic band structure calculated by Band structure from a first-principles OPW calculation [35]. The calculation does not include the spin-orbit interaction.*

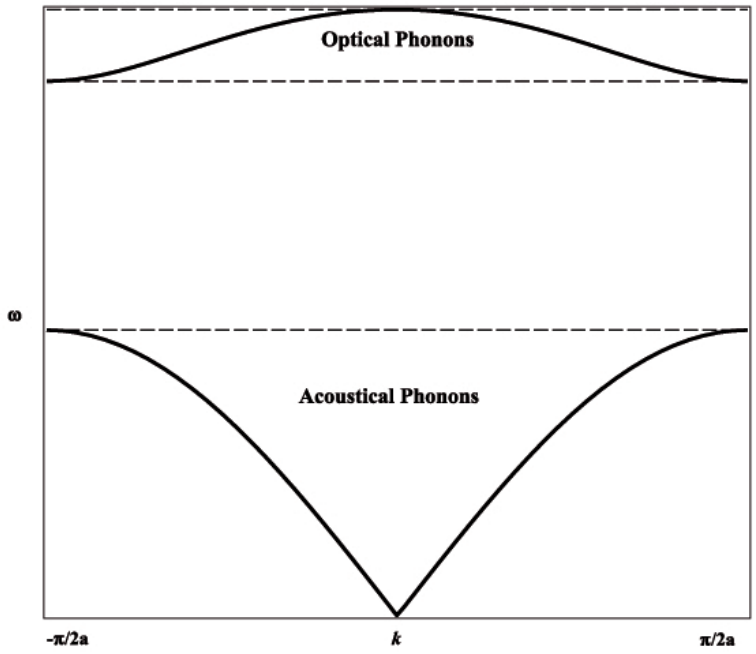

Figure 2.5: *Acoustical and optical branches of linear atomic chain phonons dispersion, within the first one-dimensional Brillouin zone. The curves were calculated using cadmium sulfide physical parameters.*

2.3 Vibrational Properties of Wurtzite CdS

The work carried out in this thesis is strongly based on the study of vibrational properties of wurtzite CdS quantum dots by Raman scattering spectroscopy. Therefore, it is of fundamental importance to know accurately the physics at the basis of lattice vibration starting from the concept of phonon, then passing to the crystal symmetry and making use of a geometrical tool such as the group theory.

2.3.1 Concept of Phonon

A vibrational wave propagating in a solid is usually described quantummechanically by the particle "phonon" obeying to the Bose-Einstein statistic. The phonons can be divided in two categories, the acoustical and optical. The acoustic phonons are collective translations of atom chains along a particular crystallographic direction, while the optical phonons are compressions-relaxations or shearing compressions-relaxations of adjacent atoms propagating along a crystallographic direction. Among acoustic and optical phonons, we can still distinguish between transverse and longitudinal modes indicated respectively as TA, LA for acoustic and TO and LO for optical phonons. Considering a linear atomic chain of atoms with mass M, the acoustic phonons are described by the semiclassical differential equation

$$M\frac{\partial^2 u_n}{\partial t} = -\beta(2u_n - u_{n+1} + u_{n-1}) \tag{2.1}$$

where u is the atomic displacement with the index of the n-th atom, and β is the elastic constant. The solution is the dispersion of ω in function of wavevector $\vec{k}$

$$\omega = \sqrt{\frac{4\beta}{M}}|\sin\frac{1}{2}ka| \tag{2.2}$$

where k is the wavevector and a is the one-dimensional lattice constant. In a similar way, considering a linear diatomic chain constituted by n atoms having masses m and M, and assuming for simplicity that

only the nearest neighbor atoms interacts, the equations of motion are the following coupled differential equations

$$m\frac{\partial^2 u_{2n}}{\partial t} = \beta(u_{2n+1} - 2u_{2n} + u_{2n-1}) \tag{2.3}$$

$$M\frac{\partial^2 u_{2n+1}}{\partial t} = \beta(u_{2n+2} - 2u_{2n+1} + u_{2n}) \tag{2.4}$$

where β is always the elastic constant. The common solution of equations 2.3 provides the following eigenvalues

$$\omega^2 = \beta\left(\frac{1}{m} + \frac{1}{M}\right) \pm \beta\sqrt{\left(\frac{1}{m} + \frac{1}{M}\right)^2 - \frac{4\sin^2(\frac{1}{2}ka)}{mM}} \tag{2.5}$$

where k is the phonon wavevector and a is the one dimensional lattice constant. Equation 2.5 is thus the optical phonon dispersion relation. In figure 2.5 the optical and acoustic phonon dispersions are shown. k ranges in the first monodimensional Brillouin zone, i.e. from $-\pi/a$ to π/a. The dashed lines (from the bottom) are the constant values $\sqrt{2\beta/M}$, $\sqrt{2\beta/m}$ and $\sqrt{2\beta(1/m + 1/M)}$ respectively. In spite of its simplicity, such 1D modellization will result helpful to understand the lattice dynamics even in 3D crystals.

2.3.2 Phonon Symmetry

Even though the phonon is a quantum mechanical concept, it can be associated to the classical mechanic concept of normal modes. The normal modes are a pattern of motions in which all elements of the system (atoms) move sinusoidally with the same frequency. The geometry of normal modes is related to the crystal symmetry, thus the group theory is used to assign a symmetry to normal modes. In the general case, a group G is a set of abstract elements $G_1, G_2, ...$ satisfying a set of four mathematical operations [36]. To put in use the group theory, to every group element can be assigned a square matrix representing a symmetry operation in the 3D-space, in particular, these matrices make a coordinates change. The set of matrices are known as representation of the group and they can be 1-, 2- or 3-dimensional depending on the type of symmetry operation. It does exist however a so-called irreducible representation from which all the other can be built.

Almost all the most used and most studied semiconductors crystallize essentially in two types of crystalline structures, cubic which divides in diamond-like (C, Si, Ge) and zinc-blende (III-V and II-VI semiconductors) and the hexagonal Wurtzite (II-VI and III-V). Some exceptions are represented for example by TiO_2 which is tetragonal, the elemental Se and Te which are trigonal. III-V and II-VI semiconductors may crystallize either in zinc-blende both in wurtzite structures depending on the physical growth conditions and on the type of material. As we have already seen in section 2.1, in II-VI semiconductors the wurtzite structure is far more stable than the zinc-blende therefore this is the favorite structure in which these materials crystallize. Also for II-VI nanocrystals one founds that the most stable structure is the wurtzite, however in particular conditions it is even possible to grow zinc-blende nanocrystals [37–39].

Cadmium sulfide, as the other II-VI compounds is commonly know to have wurtzite structure which belongs to point group C_{6v}^4 containing the symmetry elements representing the operations of translation, reflection and rotation.In table 2.2 can be found all the irreducible representation of C_{6v} group. It can be seen how the A_1, E_1, E_2 modes transform like the three sets of quadratic functions. In particular, $x^2 + y^2$ and $x^2 - y^2$ are ellipsoid equations and thus they can transform like the polarization ellipsoids. In hexagonal structure there are four atoms per unit cell and using the characters table, the group theory predicts 9 optical phonon modes denoted by the following sum of irreducible representations $A_1 \bigoplus E_1 \bigoplus 2B_1 \bigoplus 2E_2$ near $\vec{k} = 0$ where one A_1 and one E_1 are acoustic so

C_{6v}	E	C_2	$2C_3$	$2C_6$	$3\sigma_v$	$3\sigma_v^{'}$	*quadratic functions*
A_1	1	1	1	1	1	1	x^2+y^2, z^2
A_2	1	1	1	1	-1	-1	-
B_1	1	-1	1	-1	1	-1	-
B_2	1	-1	1	-1	-1	1	-
E_1	2	-2	-1	1	0	0	xz, yz
E_2	2	2	-1	-1	0	0	x^2-y^2, xy

Table 2.2: *Character table for irreducible representations of the crystallographic point group* C_{6v}

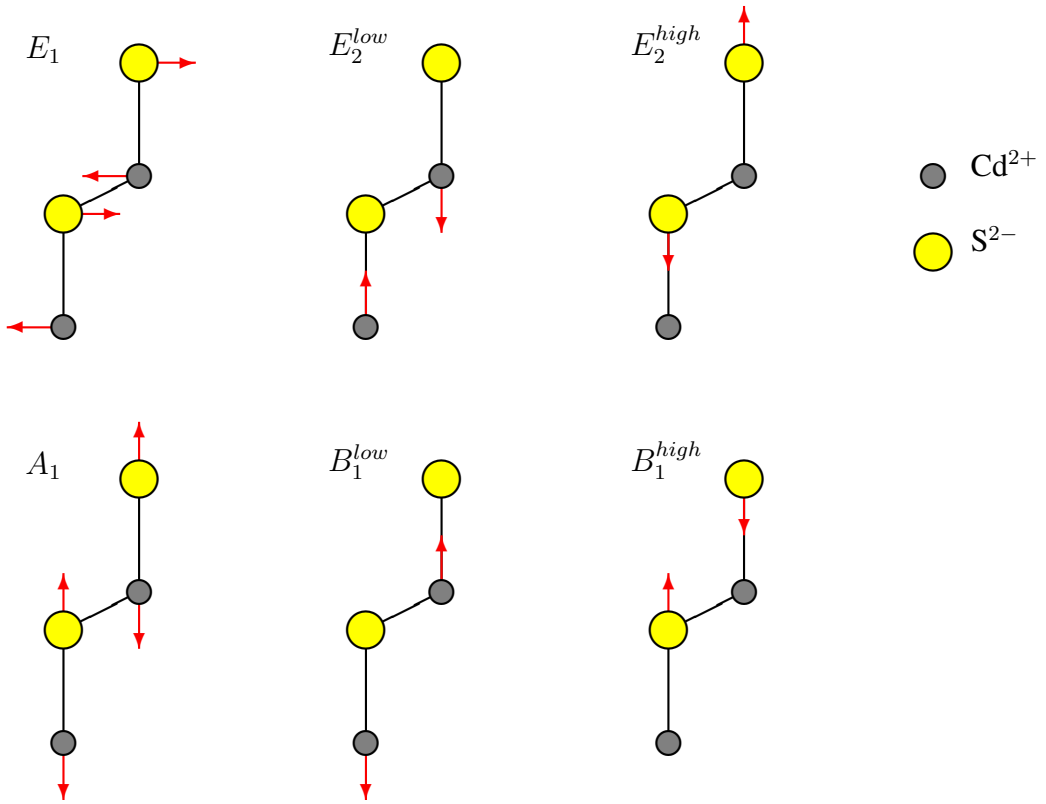

Figure 2.6: *Relative motions of the atoms in wurtzite unit cell corresponding to the optical vibrations.*

they have been excluded from the count. The optical A_1 and one E_1 modes are polar modes due to the vibration of two different atoms (Cd and S) with different charges produces a dipole moment, hence they will result to be IR active. In addiction, the presence of a dipole moment causes a splitting of the two modes into longitudinal (LO) and transversal (TO). The two E_2 modes and similarly B_2 modes are named E_2^{high} and E_2^{low} (B_1^{high} and B_1^{low}) and even though having the same symmetry they have a large difference in frequency $\omega_{E_2^{high}} > \omega_{E_2^{low}}$, since in the case of ($E_2^{high}$ there will be a compression between atoms instead of a shearing force like in E_2^{low} where the restoring force will be much higher than in the first case. A_1 and E_1 modes are double degenerate and are Raman and IR active. The two twofold E_2 modes (E_2^{high} and E_2^{low}) are only Raman active, while the two B_1 modes are neither Raman nor IR active and are termed silent modes. The normal modes are visualized in figure 2.6.

2.3.3 Phonon Dispersion of Wurtzite CdS

As already seen in subsection 2.3.1, the dispersion relations 2.2 and 2.5 are the frequency eigenvalues in dependence of the phonon wavevector $\vec{k}$ which varies within the first monodimensional Brillouin zone ($-2\pi/a < k < 2\pi/a$). For real 3D crystals, the concept of phonon dispersion is analogue. Nevertheless, the wavevector $\vec{k}$ varies in specified directions of the first three-dimensional Brillouin zone, say, the points of highest symmetry indicated by capital letters in figures 2.2. Referring to figure 2.7 and considering the phonons propagating along the c axis, i.e. the direction $\Gamma \rightarrow A$, it can be observed that there are three acoustic modes, $A_1(LA)$ and two degenerated $E_1(TA)$. Considering optical modes, there is one $A_1(LO)$, two degenerated $E_1(TO)$, one B_1^{low} and one B_1^{high} and finally two degenerated E_2^{low} and E_2^{high}. Since the $\vec{k}$ is a vector in the reciprocal space, the crystallographic directions are represented in the reciprocal space by 6 points of the highest symmetry in the first Brillouin zone, see figure 2.2. It can be observed that the phonon dispersion is constituted by acoustic and optical branches. The acoustical branches have frequency zero at Γ point while their dispersion increases in the other directions. At Γ point ($\omega = 0$) a translation of the entire crystal results. In first order Raman scattering processes, only phonons at $\vec{k} \approx 0$ are scattered, therefore, only phonons with wavevector close to Γ point one must be considered. The first order acoustic phonons at $\vec{k} \approx 0$ are not easily observable by Raman scattering since their frequencies result to be very small ($< 5\, cm^{-1}$), thus very close to the elastic scattering. However, higher second and/or higher order scattering processes become observable since their frequency result n times the frequency of the first order process. First order acoustic phonons are observable only by Brillouin scattering and they will not be investigated in this work. The total count of phonon branches, acoustic and optical, at Γ point does not match with the predicted 12 modes, this can be explained by the fact that $E_1(TA)$, $E_1(TO)$, E_2^{low} and E_2^{high} are there twofold degenerated. To notice also the splitting due to the anisotropic macroscopic electric field in the crystal of the A_1 and E_1 modes produces longitudinal and transversal optical branches for both modes. Longitudinal modes result to have higher energy than the transversal. In E_2 an B_1 modes, another kind of splitting occurs. Here the splitting is not due to the macroscopic electric field, rather to difference in energy between restoring and shearing force which give rise to *high* and *low* modes respectively. In this case the splitting is much larger than in the case of TO and LO phonons so that the *low* branches lie among the acoustic modes. To notice that in figure 2.7 the electronic symmetry notation was used. However, phonon normal modes are usually named by the Schönflies notation, and for this reason in table 2.3 the correlation between the two symmetry notations is reported.

Schönflies notation	Electronic notation
A_1	Γ_1
A_1	Γ_1
B_1	Γ_4
B_2	Γ_7
E_1	Γ_5
E_2	Γ_5

Table 2.3: *Correspondence between electronic notation and Schönflies notation.*

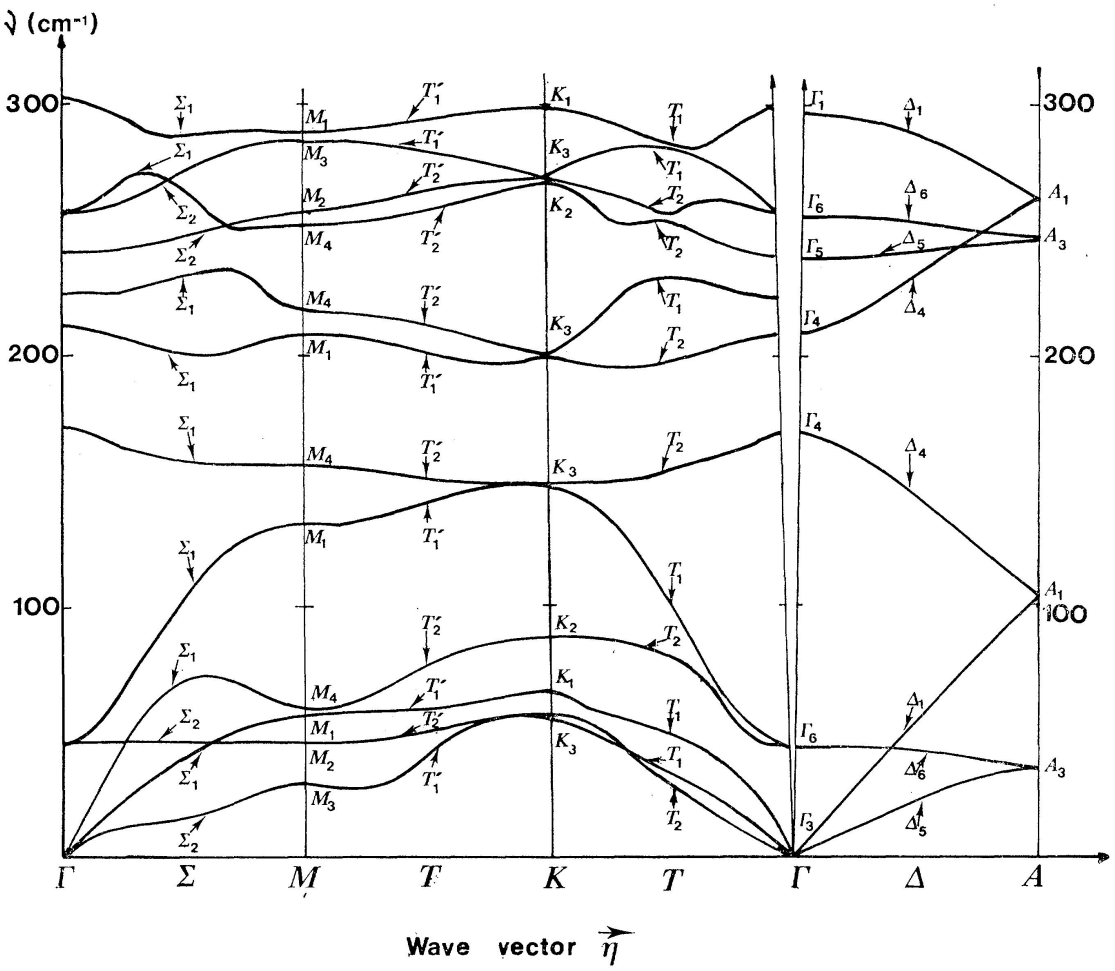

Figure 2.7: *Wurtzite CdS phonon dispersion curves from [40]. The dispersion was obtained by a computational mean starting from $\vec{k} = 0$ phonon frequencies obtained by Raman spectroscopy and experimental dielectric constant.*

2.3.4 Raman Selection Rules

To interpret and to predict Raman spectra it is very helpful to adopt the Porto notation. This notation takes the form $\vec{k}_i(\vec{e}_i,\vec{e}_s)\vec{k}_s$ where k_i and k_s are the wavevectors of incident and scattered radiation. The polarization of the incoming and scattered radiation are represented by the $\vec{e}_i$ and $\vec{e}_s$ unitary vectors respectively. By Raman spectrometers, several geometrical configurations can be used, for example, of very common use are the configuration $z(x,x)\bar{z}$ and $z(x,y)\bar{z}$. In this configuration, the incoming and scattered radiation are parallel while the polarizations of the incoming and scattered light are parallel in the first case, perpendicular in the second. Obviously, they are both perpendicular to the z axis.
Of fundamental importance is the knowledge of Raman selection rules which can be determined by a simple calculation with vectors and matrices (tensors). The scattered light power is proportional to the second-rank tensor $\Re$ (Raman tensor) through the equation, see Chapter 4

$$dS \propto |\hat{e}_S \cdot \Re \cdot \hat{e}_L|^2 \tag{2.6}$$

where $\vec{e}_i$ and $\vec{e}_s$ are described above. Making use of the group theory it was found that only A_1, E_1 and E_2 are Raman active modes and each has an associated Raman tensor or tensors. The

Mode	Scattering geometry	Raman tensors	Allowed coupling
E_2	low	$\begin{pmatrix}0&d&0\\d&0&0\\0&0&0\end{pmatrix}$ $\begin{pmatrix}d&0&0\\0&-d&0\\0&0&0\end{pmatrix}$	Γ_9-Γ_7
	high		
E_1	TO	$\begin{pmatrix}0&0&0\\0&0&c\\0&c&0\end{pmatrix}$ $\begin{pmatrix}0&0&-c\\0&0&0\\-c&0&0\end{pmatrix}$	Γ_7-Γ_7
	LO		Γ_9-Γ_7
A_1	TO	$\begin{pmatrix}a&0&0\\0&a&0\\0&0&b\end{pmatrix}$	Γ_7-Γ_7
	LO		Γ_9-Γ_9

Table 2.4: *Normal modes with relative Raman tensors and allowed coupling with electronic terms elaborated from [30]*

labels in the brackets beside the phonon mode symmetry symbol indicate the direction of the induced electric dipole in the case of polar phonon modes.
Given a particular scattering geometry, In order to determine whether a mode is allowed or forbidden by symmetry in a particular scattering geometry, i.e. whether it is Raman active or not, the relation 2.6 can be exploited. The scattering geometries $z(\vec{e}_L,\vec{e}_S)\bar{z}$, may be used in crossed polarization $\vec{e}_S = (1,1,0)$ and $\vec{e}_L = (-1,1,0)$ and in parallel polarization $\vec{e}_S = \vec{e}_L = (1,1,0)$. Using the equation 2.6, one can obtain the following vectorial operation for phonon modes with the two polarization configurations. With the crossed scattering configuration $z(x,y)\bar{z}$, the scattering cross section for the three different modes can be calculated as follow

$$S_{E_2} \propto \left|\begin{pmatrix}1\\1\\0\end{pmatrix}\begin{pmatrix}0&d&0\\d&0&0\\0&0&0\end{pmatrix}\begin{pmatrix}-1\\1\\0\end{pmatrix}\right|^2 + \left|\begin{pmatrix}1\\1\\0\end{pmatrix}\begin{pmatrix}d&0&0\\0&-d&0\\0&0&0\end{pmatrix}\begin{pmatrix}-1\\1\\0\end{pmatrix}\right|^2 = d^2 \tag{2.7}$$

$$S_{E_1} \propto \left|\begin{pmatrix}1\\1\\0\end{pmatrix}\begin{pmatrix}0&0&c\\0&0&0\\c&0&0\end{pmatrix}\begin{pmatrix}-1\\1\\0\end{pmatrix}\right|^2 + \left|\begin{pmatrix}1\\1\\0\end{pmatrix}\begin{pmatrix}0&0&0\\0&0&c\\0&c&0\end{pmatrix}\begin{pmatrix}-1\\1\\0\end{pmatrix}\right|^2 = 0 \tag{2.8}$$

$$S_{A_1} \propto \left| \begin{pmatrix} 1 \\ 1 \\ 0 \end{pmatrix} \begin{pmatrix} a & 0 & 0 \\ 0 & a & 0 \\ 0 & 0 & b \end{pmatrix} \begin{pmatrix} -1 \\ 1 \\ 0 \end{pmatrix} \right|^2 = 0 \tag{2.9}$$

It can be seen that with the crossed scattering geometry only E_2 modes will be allowed. A similar calculation can be done for the parallel scattering geometry $z(x,x)\bar{z}$

$$S_{E_2} \propto \left| \begin{pmatrix} 1 \\ 1 \\ 0 \end{pmatrix} \begin{pmatrix} 0 & d & 0 \\ d & 0 & 0 \\ 0 & 0 & 0 \end{pmatrix} \begin{pmatrix} -1 \\ 1 \\ 0 \end{pmatrix} \right|^2 + \left| \begin{pmatrix} 1 \\ 1 \\ 0 \end{pmatrix} \begin{pmatrix} d & 0 & 0 \\ 0 & -d & 0 \\ 0 & 0 & 0 \end{pmatrix} \begin{pmatrix} 1 \\ 1 \\ 0 \end{pmatrix} \right|^2 = d^2 \tag{2.10}$$

$$S_{E_1} \propto \left| \begin{pmatrix} 1 \\ 1 \\ 0 \end{pmatrix} \begin{pmatrix} 0 & 0 & c \\ 0 & 0 & 0 \\ c & 0 & 0 \end{pmatrix} \begin{pmatrix} 1 \\ 1 \\ 0 \end{pmatrix} \right|^2 + \left| \begin{pmatrix} 1 \\ 1 \\ 0 \end{pmatrix} \begin{pmatrix} 0 & 0 & 0 \\ 0 & 0 & c \\ 0 & c & 0 \end{pmatrix} \begin{pmatrix} 1 \\ 1 \\ 0 \end{pmatrix} \right|^2 = 0 \tag{2.11}$$

$$S_{A_1} \propto \left| \begin{pmatrix} 1 \\ 1 \\ 0 \end{pmatrix} \begin{pmatrix} a & 0 & 0 \\ 0 & a & 0 \\ 0 & 0 & b \end{pmatrix} \begin{pmatrix} 1 \\ 1 \\ 0 \end{pmatrix} \right|^2 = a^2 \tag{2.12}$$

In this case it turns out that only E_2 and A_1 modes are allowed for symmetry. From these vectorial calculations is thus possible to predict the allowed Raman scattering modes for phonons having $\vec{q} \sim 0$. All the allowed Raman modes of hexagonal CdS with relative frequencies are reassumed in table 2.5. Nevertheless, experimentally such theoretical prediction are not always respected. It may happen that in a specific scattering configuration, a mode forbidden by symmetry is visible in the spectra. This can be explained by the fact that wanted geometry is never perfectly respected and contributions from other configurations are present. This is usually caused by the non perfect parallelism between the axis of incoming and scattered light z and $\bar{z}$ which might be produced by laser light misalignment or sample tilting.

Scattering geometry	E_2^{low}	E_2^{high}	$E_1(TO)$	$E_1(LO)$	$A_1(TO)$	$A_1(LO)$
$z(x,x)\bar{z}$	41.8	255.7				303.6
$z(x,y)\bar{z}$	41.8	255.7				
$x(z,z)\bar{x}$				306.9	234.7	
$x(y,y)\bar{x}$	41.8	255.7			234.7	
$x(y,z)\bar{x}$			242.6			

Table 2.5: *Frequencies in cm^{-1} of Raman allowed modes of bulk CdS at 77 K taken from [41]. The empty places mean that the mode is forbidden in that scattering geometry.*

2.4 Confinement of Electrons in Semiconductor Nanocrystals

The electronic structure of semiconductor crystals is described correctly by the band theory where the electron states are not distributed in discrete levels as in atoms and molecules [42], rather form continuous bands, namely conduction and valence bands, which are separated by an energy gap E_g.
In nanostructured semiconductors, the band structure model is no longer sufficient to explain the electronic structure and other models must be taken into account. Quantum confinement occurs when the De Broglie wavelengths of electron and hole λ_e, λ_h and the Bohr radius of an exciton a_B are in the order or are larger than the spatial dimension of the crystal. This situation can hold for one, two or three direction in the space. Therefore one can have 1-, 2- and 3-dimensional quantum confinement depending whether the structure is 2-dimensional, 1-dimensional or 0-dimensional.
The effects of low dimensionality are immediately visible in the density of states (DOS) of a semiconductor nanoparticle, see figure 2.8. At the diminishing of the size, the continuous bands become discrete, i.e. they assume an atom-like aspect. At the same time, the aperture of the band gap is observed. In a first approximation, one can imagine the potential energy barriers to be infinite, thus, the energetic levels for a quantum well (2-D confinement) become

$$E_n = \frac{\pi^2 \hbar^2}{2m_{e,h} l^2} n^2 \quad n = 1, 2, 3... \tag{2.13}$$

where l is the size along the confinement direction, $m_{e,h}$ is the total mass of electron and hole ($m_e + m_h$), and n is an integer quantum number. The dispersion relation will have the form

$$E(k) = E_n + \frac{\hbar^2 (k_x^2 + k_y^2)}{2m_{e,h}} \tag{2.14}$$

these equations are valid only considering the quantum well as a 1-D box with infinite potential barriers and x, y infinite in the not confinement directions. Nevertheless, these equations gives only approximate energy values, as well as of dispersion relation and electronic wavefunctions for a real quantum well. The situation becomes even more complicated for lower dimensionality, especially for 0-D nanostructures. From here to the end of the chapter, only quasi 0-dimensional semiconductor crystals will be discussed, and the attention will be focused especially on cadmium sulfide quantum dots.

2.4.1 Absorption bands

Almost every theoretical model used to describe a quasi 0-D nanocrystal assume the structures to have a spherical shape. Obviously, this does not respect the reality but the calculations does not differ too much from more elaborated calculations taking into account the exact geometry. This fact holds especially in very small quantum dots with few atoms [43].
In modeling electronic properties of quantum dots the electron-hole formalism is always invoked, and the formation of an electron-hole pair is viewed as an exciton. It is worth to remark that the so called exciton in nanocrystals is not different from the electronic transition in a molecule (HOMO-LUMO transition) or even better, from an electronic transition in an atom

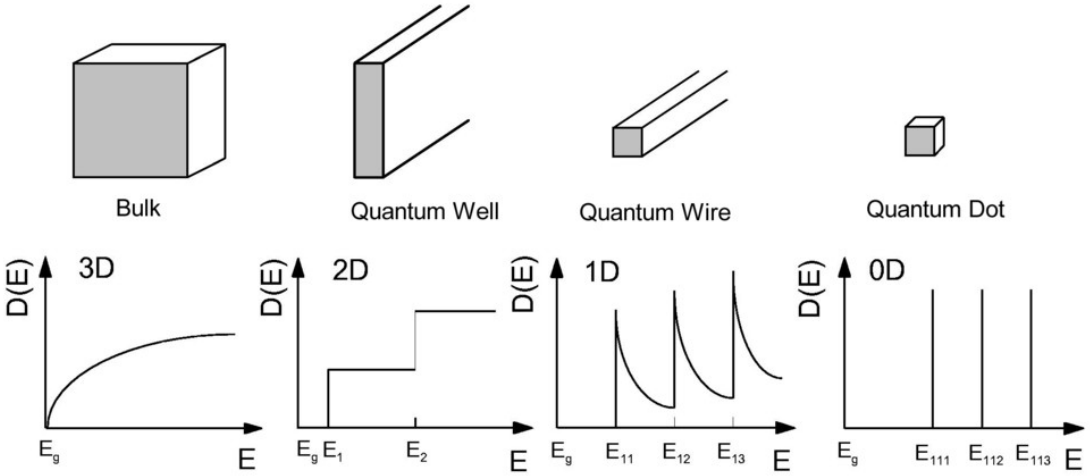

Figure 2.8: *Density of states of a semiconducting material for bulk, $2-D$, $1-D$ and $0-D$ crystals. Differently from bulk, where the density of states is continuous ($\rho(E) \propto \sqrt{E-E_F}$), in a $2-D$ crystal it becomes a step function while in $1-D$ crystal it has the following expression $\rho(E) \propto 1/\sqrt{E-E_F}$. Quite different is the situation in quasi $0-D$ structures where DOS is a set of Dirac-delta functions $\rho \propto \delta(E-E_F)$.*

from whose the nomenclature of electronic states has been mutuated. Conversely, substantial differences do exist with the concept of exciton in bulk semiconductor crystal which is a pseudo-particle arising from the $e^- - h^+$ Coulombian interaction and having energetic levels few meV below the valence band.
It is useful to distinguish between two cases, the weak confinement regime applicable when the radius of the nanoparticle r is small but still larger than the exciton Bohr radius $a_B = \varepsilon\hbar^2/\mu e^2$ and the strong confinement regime applicable when $r \ll a_B$.
The interaction between hole and electron can be described by the following Hamiltonian

$$H = -\frac{\hbar^2}{2m_e^*}\nabla_e^2 - \frac{\hbar^2}{2m_h{}^*}\nabla_h^2 - \frac{e^2}{\varepsilon\left|\vec{r}_e - \vec{r}_h\right|} \tag{2.15}$$

the application of this hamiltonian on the wavefunction yields the following energy eigenvalues

$$E_n(\vec{k}) = E_g + \frac{\mu e^4}{2\varepsilon\hbar^2 n^2} + \frac{\hbar^2\vec{k}^2}{2M} \tag{2.16}$$

where $M = m_e^* + m_h^*$ and $\vec{k}$ is the wavevector of the exciton pseudo-particle. In the *weak confinement* regime, the quantization of exciton center of mass motion occurs and the last term of equation 2.16, exciton kinetic energy, must be replaced by the term which is the solution of the free particle in spherical box. It follows that

$$E_{nml} = E_g + \frac{\mu e^4}{2\varepsilon\hbar^2 n^2} + \frac{\hbar^2\chi_m^2 l}{2Mr^2} \tag{2.17}$$

where χ_{nml} are the roots of the spherical Bessel functions, M is the sum of the mass of electron and hole, and nml are discrete quantum numbers. In this equation, the second term is the Rydberg energy E_{Ry} accounting the electrostatic energy of the exciton. The energy levels are

characterized by the quantum number n arising from the $e^- - h^+$ Coulombian interaction giving the hydrogen-like terms $(1S, 2S, 2P, 3S, 3P, 3D...)$, and by the quantum numbers l and m of the angular momentum of the $e^- - h^+$ center of mass giving the terms $(1s, 1s, 1p..., 2s, 2p, 2d...)$. In the *strong confinement* regime there are no bound excitonic states just because of $r \ll a_B$ The motion of electron and hole may be considered uncorrelated therefore, in a first approximation, the Coulombian term in equation 2.17 can be neglected in respect of the last term of kinetic energy. The expression of exciton energies becomes thus

$$E_{nl} = E_g + \frac{\hbar^2 \chi_{nl}^2}{2Mr^2} \tag{2.18}$$

where χ_{nl}^2 are always the Bessel function roots, E_g is the band-gap of the bulk material, while M is the mass of the electron. This equation produces a set of discrete energetic levels having symbols $1s_h1s_e$, $1p_h1p_e$, $1d_h1d_e$ and so on. These symbols are always matched by the spin multiplicity number appearing as subscript.
A more correct approach is to introduce the electron-hole interaction potential $\frac{e^2}{|\vec{r}_e - \vec{r}_h|}$ and a confinement potential $U(\vec{r})$ which takes into account the finite potential barrier due to the quantum dot surface. Calculation of this type are reported in [6, 43–46] which provide the following energy level for the lowest excited state $1s1s$

$$E_{nl} = E_g + \frac{\pi^2 \hbar^2}{2\mu r^2} - 1.786\frac{e^2}{\varepsilon r} - 0.248E_{Ry}^* \tag{2.19}$$

where $\mu = 1/m_e^* + 1/m_h^*$ is the reduced mass of the electron-hole couple, ε is the dielectric constant of the material and E_{Ry}^* is the exciton Rydeberg energy. The coefficients appearing in the third and fourth terms of the second member are derived from the Bessel functions roots. The third term $e^2/\varepsilon r$ is the Coulombian interaction between hole and electron while the last term is a further correction. However, it can be given a more general expression of equation 2.19 from which the nanocrystal band gap energy can be calculated [43].

$$E_{exc} = E_g + \left(\frac{e^2}{2\varepsilon r}\right)\left[A_1 + \frac{\mu e^2 r}{\varepsilon \hbar^2}A_2 + \left(\frac{\mu e^2 r}{\varepsilon \hbar^2}\right)^2 A_3 + ...\right] \tag{2.20}$$

The coefficients A_1, A_2, A_3, ... are described by the Bessel functions roots. They may assume different values from state to state. It is trivial that the higher the number of utilized coefficient is the higher is the accuracy in describing an excited state.
In order to take into account the non-infinite potential barrier and the different dielectric constant between nanocrystals and the media in which they are imbedded ($\varepsilon_{semic.} > \varepsilon_{media}$), a potential U has been introduced [47]. This new potential brings further corrective terms which decrease the exciton energy. The effect however becomes appreciable especially when $\varepsilon_1 \gg \varepsilon_2$, $m_h \gg m_e$ and $a_h < a < a_e$.

Further to quantum-size effects, real absorption spectra are characterized by other features reflecting the presence of light and heavy hole branches near $\vec{k} = 0$ and the splitting due to spin-orbit interaction which is strong in semiconductors with heavy atoms such as CdS. Moreover, in some materials there is an anisotropy of the hole and electron mass tensors i.e. the value of the reduced mass is changes in different directions of the space. Therefore, to a have a more accurate description of the absorption spectra the approach of calculation must be modified, in particular, introducing a hole kinetic energy operator (Luttinger Hamiltonian). Calculations

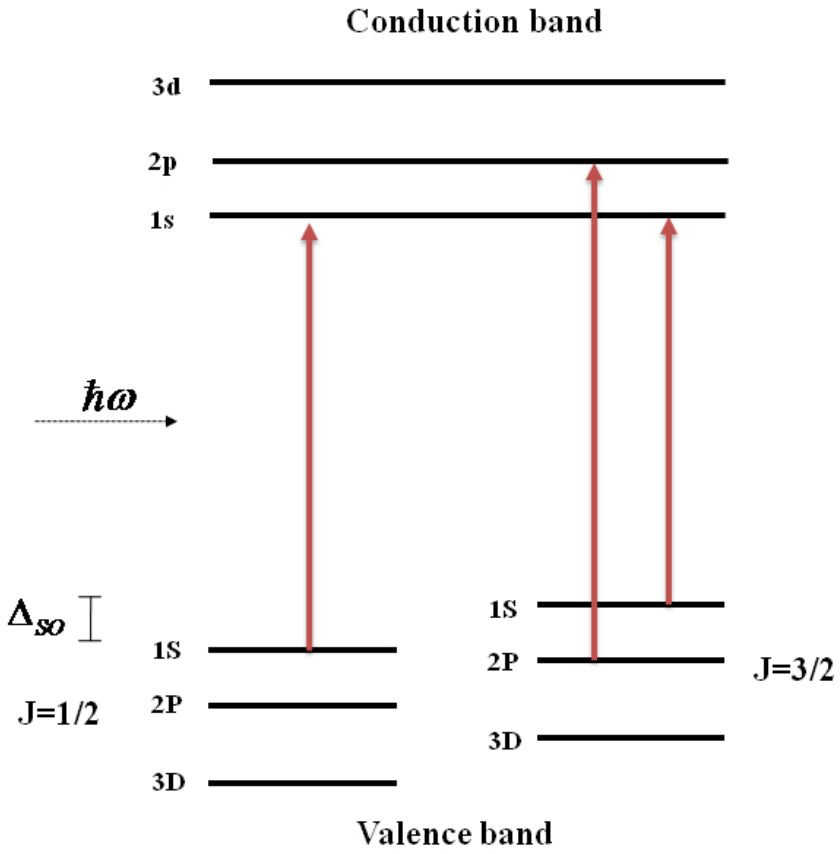

Figure 2.9: *Electronic levels in a generic II-VI semiconductor quantum dot. The red arrows represent the three most intense transitions usually observed in room temperature absorption experiments. The splitting of the valence bands levels is due to the spin-orbit interaction.*

which account such correction have been performed in [48–50] provide new hole energetic levels hence, new transition diagrams. The hole wavefunctions are linear combinations of different states and in adjoint to l, the $(l+2)$ quantum number also appears because the Hamiltonian couples with $\Delta l = 0, \pm 2$ quantum numbers. There will be in turn the following selection rules

$$nl \rightarrow n^*(l, l+2)_F \tag{2.21}$$

Where the quantum number n^* is relative to the excited state , while $F = l + J$ is the total angular momentum quantum number. Finally, it is worth to remark that due to hole wavefunction mixing, the selection rules will allow also transitions even when $\Delta n \neq 0$, hence new extra absorption peaks will appear. Calculations of this type for CdS quantum dots are reported in [51, 52]. According to [52], the valence hole levels of CdS quantum dots, or more in general of

Transition number	Electronic symbol
1	$1S_{3/2}1s$
2	$2S_{3/2}1s$
3	$2S_{1/2}1s$
4	$1P_{3/2}1p$
5	$1P_{1/2}1p$
6	$2S_{3/2}2s$

Table 2.6: *Optical transitionsin II-VI semiconductor quantum dots.*

II-VI quantum dots, can be derived from the bulk valence band of the zinc-blende modification whose electronic structure was already discussed in section 2.2. Similarly to what happens in bulk crystal, the spin-orbit interaction splits the band in two non degenerated levels with spin multiplicity $3/2$ and $1/2$. Yet, in quantum dots the situation is far more complicated since the quantum confinement further splits these holes states in several discrete levels. These atomic-like levels come out from the use of Luttinger-Hamiltonian combined with a spherical potential in the spherical band approximation. As result, a mixing between the bulk valence bands occurs. While this mixing is weak in bulk excitons, it is significant in quantum dots. The fundamental result is that parity and the total hole angular momentum, $F = l + J$, are the only good quantum numbers for the hole envelope function, while l and J are not conserved. Thus, as direct consequence a valence band mixing occurs producing hybrid hole states. As example, it can be seen that the first excited pair state $1S_{3/2}1S_e$ contains three hole components: ($F = 3/2$, $J = 3/2$, $l = 0$), ($F = 3/2$, $J = 3/2$, $l = 2$), and ($F = 3/2$, $J = 1/2$, $l = 2$).
This complicate electronic structure manifests in low temperature absorption spectra ($T \approx 4\,K$) which excitonic terms relative to II-VI semiconductor quantum dots are shown in table 2.6 [43]. Nevertheless, at room temperature ($T = 300\,K$) the absorption spectra are characterized by the three most intense transitions $1S_{3/2}1s$, $2S_{1/2}1s$ and $1P_{3/2}1p$ only [43, 52]. These transitions are illustrated by the diagram of figure 2.9.

2.4.2 Photoluminescence Emission

II-VI and III-V bulk semiconductors posses a high intrinsic photoluminescence quantum efficiency due to direct band transitions [42]. It has been demonstrated that in semiconductor

quantum dots or more in general, in semiconductor nanostructures, the luminescence emission results to be enhanced in respect with the same material in bulk [53]. In general, photoluminescence occurs when a system is excited to a higher energy level by absorbing a photon, and then spontaneously decays to a lower energy level emitting a photon. To conserve energy, the emitted photon cannot have more energy than the exciting photon, unless two or more excitation photons act simultaneously. Usually, when the excitation is undergone by one photon, the emission energy is lower than the exiting energy, therefore an intermediate non-radiative downward transitions must occur. Photoluminescence is divided into two types depending on the nature of the ground and the excited states. In molecules, when the excited state is a singlet, the electron in the higher-energy orbital has the opposite spin orientation as the second electron in the lower orbital. These two electrons are said to be paired. In a triplet state these electrons are unpaired, that is, their spins have the same orientation. Return to the ground state from an excited singlet state does not require an electron to change its spin orientation. A change of spin orientation is needed for a triplet state to return to the singlet ground state. Fluorescence is the emission which results from the return to the lower orbital of the paired electron. Such transitions are quantum mechanically allowed and the emissive rates are typically near 10^8 s^{-1}. These high emissive rates result in fluorescence lifetimes near 10^{-8} s or 10 ns. Phosphorescence is the emission which results from transition between states of different multiplicity, generally a triplet excited state returning to a singlet ground state. Such transitions are not allowed and the emissive rates are much slower than for singlet states. Typical phosphorescent lifetimes range from milliseconds to seconds, depending primarily upon the importance of deactivation processes other than emission. In semiconductor quantum dots and more in general in semiconductors, it has never been observed Phosphorescence phenomena, therefore, here in advance the photoluminescence will be referred exclusively to the fluorescence process. The two fundamental parameters involved in the photoluminescence processes are the lifetime and the quantum yield. The meaning of these parameters can be better understood by the diagram in figure 2.10. In this diagram, the individual relaxation processes leading to the relaxed S_1 state are not explicitly illustrated. Conversely, there are illustrated the emission rate Γ and its rate of radiationless decay to the ground state S_0. The photoluminescence quantum yield is the ratio of the number of photons emitted to the number absorbed. The fraction of emitters (quantum dots) that decays through radiative and non-radiative emissions is given by

$$\Phi = \frac{\Gamma}{\Gamma + k_{nr}} \tag{2.22}$$

Where k is the nonradiative rate constant which together with Γ depopulate the excited state. The quantum yield can be close to unity if the radiationless rate of deactivation is much smaller than the rate of radiative decay, that is $k \ll \Gamma$. The lifetime τ of the excited state is defined by the average time the emitters spend in the excited state prior to return to the ground state.

$$\tau = \frac{1}{\Gamma + k_{nr}} \tag{2.23}$$

where k_{nr} is the nonradiative rate constant. The lifetime of the emitter in the absence of nonradiative processes is called intrinsic lifetime τ_0, and is given by

$$\tau_0 = \frac{1}{\Gamma} \tag{2.24}$$

This leads to the familiar relationship between the quantum yield and the lifetime

$$\Phi = \frac{\tau}{\tau_r} \tag{2.25}$$

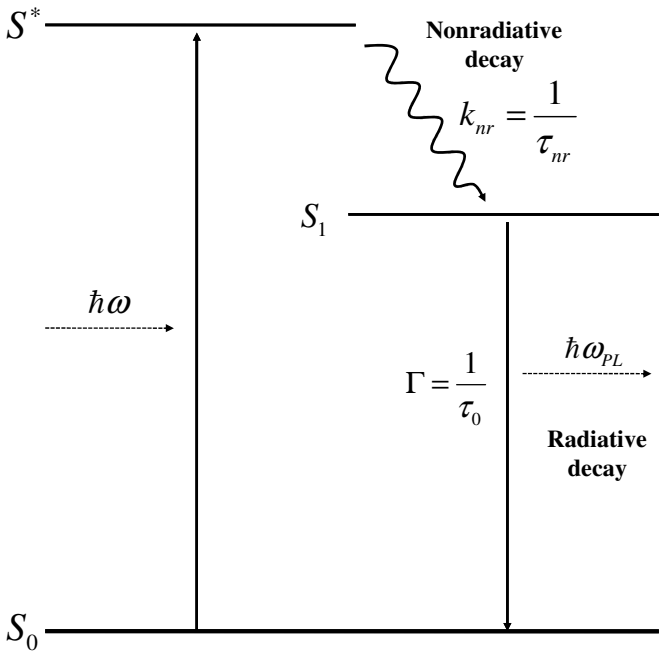

Figure 2.10: *Photoluminescence diagram showing radiative and non-radiative processes.*

where τ_r is the lifetime of the electronic state which decays radiatively. In semiconductor quantum dots, the electronic state lifetime τ, and consequently the quantum yield is determined by the non-radiative lifetime. The non-radiative decay, expressed by rate constant k_{nr}, is due to a series of recombination competitive paths $k_{nr} = \sum_i k_i$. In nanocrystals, due to the high surface-volume ratio an important role in radiative recombination is played by the surface defects as well as by the surface intrinsic electronic states which are however in competition with other recombination paths such as the ones induced by volume defect, impurities and the Auger process [43]. The quantum dots luminescence is thus very sensitive to surface composition and structure. Adsorbed organic molecules that have redox potentials inside the cluster "band gap" also act as surface traps, and charge transfer to these species from crystallites, conversely, adsorbed organic molecules with redox potential much larger than the quantum dot band-gap can transfer the excited state to the nanocrystal if previously excited by a photon [54].
Similarly to other II-VI, cadmium sulfide quantum dots show to posses strong photoluminescence properties [55]. In figure 2.11 are reported the diagrams of electronic levels involved in the photoluminescence emission respectively of bulk and cluster cadmium sulfide. The photoluminescence of bulk cadmium sulfide arises from the presence of shallow electronic levels just below and above the valence band respectively $\sim 10^{-2}$ eV. These shallow levels are created by the presence in the crystal of localized impurities or atomic vacancies which are able to trap electrons or holes. The situation in nanocrystals is rather different. Because of strong localization within the crystallite, electrons and holes have kinetic energies partially independent from temperature (a significant fraction of an eV). In addition, going back to what was previously said, there is a electron-hole Coulomb attraction of ~ 0.3 eV. Therefore to localize carriers,

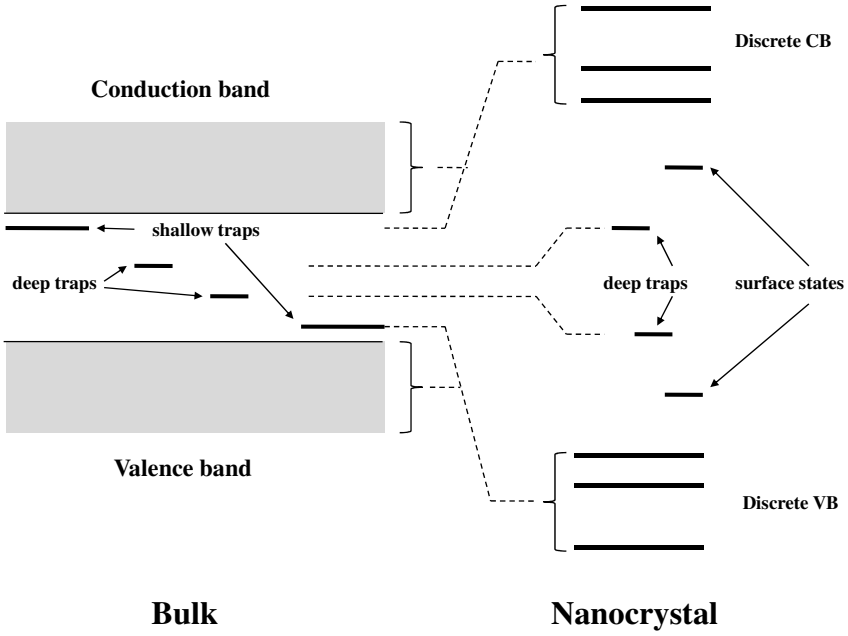

Figure 2.11: *Simplified scheme of electronic levels respectively for a bulk (left) and cluster (right) II-VI semiconductor taken from [55].*

a much deeper attractive potential is needed. In figure 2.11 it is shown a correlation diagram between the deep traps in bulk crystal and to deep traps of nanocrystal. Similarly to the band gap, the deep trap states D_+ and D_- have the energies affected by quantum confinement, i.e. they result to be size dependent. A similar argument can be used for the shallow levels S_+ and S_-. In CdS, the decay from shallow and deep trap states gives rise to a broad low energy photoluminescence band. The direct decay from the band gap gives rise to a high energy band close in energy to the first absorption transition $1S_{3/2}1s$. In CdS, the energy of this band is however red-shifted with respect to the $1S_{3/2}1s$ transition. According to [56], this red-shift is due, at least partially, to a strong coupling with the phonon field. The other causes of red-shift must be searched in the inhomogeneous broadening and nonresonant excitation of the nanocrystals [43]. In bulk CdS the shallow and deep traps are generated by the presence of impurities or nonstoichiometries which cause a thermal excess of carriers. Thus, here the photoluminescence is generated by the recombination of photogenerated minority carriers with previously existing majority carriers. In nanocrystals the mechanism is thought to be analogue [55]. It was observed that vacancies of S^{2-} on the nanocrystal surface (equivalent to a Cd^{2+} excess) sensibly enhance the photoluminescence quantum yield. In addiction, molecular electron-acceptors bond on the surface quench very efficaciously the photoluminescence. The photoluminescence is indeed depleted when electron-accepting molecules (e.g. pyridine, thiophenol) replace the long chain surfactating molecules, e.g. TOPO and fatty acids which ar less effective electron acceptors. In conclusion, core deep traps together with surface states contributions to trap free carriers extending their lifetime and enhancing their quantum yield.

2.5 Confinement of Phonons

Contrarily to the successful models existing to describe the electronic structure, A fully exhaustive model to describe quantum confinement of phonons in 2-, 1- and 0-dimensional nanostructures does not exist. The recent progresses in lattice dynamics calculations [7, 8] are still limited to very small nanocrystallites (few atoms). Therefore, the actual lattice dynamics calculations are essentially based on macroscopic models which also facilitate the calculation of phonon-related observable properties. The so called "dielectric continuum model", is purely theoretical method based on the solution of Poisson problem for a dielectric body (nanostructure) immersed in vacuum surrounding. Another different approach to interpret Raman spectra is the "$\vec{q}$-relaxation model". It was developed to explain the asymmetry of phonon lines occurring in spectra, it is however a semiempirical model since it make use of parameters obtained experimentally, e.g. the bulk phonon dispersion. Finally, the reduced size effects can be viewed in term of surface mode. Due to the elevate surface/volume ratio, the surface modes are expected to give a strong contribution.

2.5.1 Wavevector-Relaxation Model

The $\vec{q}$-relaxation model was proposed by Richter [11] to explain the phonon line red-shift and the asymmetric broadening observed in microcrystalline silicon. This model was born formerly to interpret phonon confinement in 0-D nanocrystals. Later it was extended also to 1-D and 2-D nanostructures. As it was seen in subsection 2.3.3, in bulk semiconductor crystals the selection rules allow the scattering only for phonons having $\vec{q} \approx 0$, i.e. very close to Γ point. Conversely, in nanostructure the selection rules are considered to be relaxed, i.e. the phonons which contribution to scattering lie in the interval $|\vec{q} - \vec{q}_0| \lesssim 1/d$. Considered a spherical nanoparticle of diameter d, a plane-wave-like phonon wavefunction cannot exist within the particle because the phonon cannot propagate beyond the crystal surface. In view of this, one must multiply the phonon wavefunction $\Psi(q_0, r)$ with a confinement function or an envelope function $W(r, d)$ which decays to a very small value close to the boundary. Gaussian confinement functions are the most used as envelop functions [11], thus one can write $W(r, d) = \exp \alpha r^2/d^2$. The coefficient α determines how fast the function decays. $W(r, d)$ is however in the real space, thus to relate it to the phonon dispersion, it must be transformed in the reciprocal space. This can be done by the Fourier transform of $W(r, d)$ [57]

$$C(\vec{q_0}, \vec{q}) = \frac{Ad}{(2\pi)^{3/2}} \exp\left[-\frac{d^2}{4}(\vec{q} - \vec{q_0})^2\right] \tag{2.26}$$

This function overlaps the modes at different wavelengths and if all these modes will contribution equally to the Raman spectrum, the spectral lineshape is given by

$$I(\omega) = \int_{\vec{q}} |C(\vec{q}, \vec{q}_0)|^2 \frac{\gamma}{\left(\omega - \omega(\vec{q})\right)^2 + \gamma^2} d\vec{q} \tag{2.27}$$

where $\omega(\vec{q})$ is the phonon dispersion and γ is the damping coefficient. According to [11, 21, 57], $\omega(\vec{q})$ has been estimated with different functions, in particular, a calculation for phonons in CdS nanocrystals in [21] it has been used the following dispersion relation

$$\omega(\vec{q})^2 = A^2 + B^2\sqrt{1 + \cos(qa/2)} \tag{2.28}$$

where a is a lattice parameter and A and B are semiempirical parameters which can be calculated from the phonon dispersion relation curve obtained by neutron scattering measurements or by *ab initio* calculations. In order to simplify the calculations, in [21] the phonon density of states has been included in 2.27 approximated by $D(\omega, \vec{q}) \sim [\omega(\vec{q}_0) - \omega(\vec{q})]^{3/2}$. This allow to integrate only in one dimension from 0 to 2π.
This model has the quality to be rather simple and intuitive, nevertheless it does not work properly in very small nanoparticles spectra [21]. Moreover, even though it can interpret quite well the asymmetric broadening and the red-shift of Raman lines, it does not explain at all the apparition of multi-peaks features as well as the surface modes.

2.5.2 Continuum Model

The continuum model, or better dielectric-continuum model is based on a macroscopic approach. It assumes a nanocrystal of spherical shape with radius R with a dielectric constant $\varepsilon(\omega)$ being embedded in another dielectric $\varepsilon_m(\omega)$ or in vacuum ε_0. Assuming the media as isotropic and homogeneous, the problem is reduced to write down and solve analytically the coupled differential equations [58].

$$(\omega^2 - \omega_{TO}^2)\vec{u} = \beta_{LO}\vec{\nabla}(\vec{\nabla}\cdot\vec{u}) - \beta_{TO}\vec{\nabla}\times(\vec{\nabla}\times\vec{u}) + \frac{\alpha}{\rho}\vec{\nabla}\varphi \tag{2.29}$$

$$\nabla^2\varphi = \frac{4\pi\alpha}{\varepsilon_\infty}\vec{\nabla}\cdot\vec{u} \tag{2.30}$$

where φ is the macroscopic electrostatic potential and $\alpha = \sqrt{(\varepsilon_0 - \varepsilon_\infty)\rho\omega_{TO}^2/4\pi}$ with ρ reduced mass density. β_L^2 and β_T^2 are phenomenological parameters estimated from bulk phonon dispersion relation. The solution of this problem provides an analytical expression for the atomic displacement $\vec{u}$ as well as for the LO and TO phonon dispersion and the phonon lifetime in function of the nanocrystal radius R

$$\omega_n^2 = \omega_{LO}^2 - \beta_L^2\left(\frac{\mu_n}{R}\right)^2 \tag{2.31}$$

$$\omega_n^2 = \omega_{TO}^2 + \beta_T^2\left(\frac{\nu_n}{R}\right)^2 \tag{2.32}$$

$$\gamma = \frac{\omega_{LO}^2 - \omega_{TO}^2}{\beta_T^2}R^2 \tag{2.33}$$

where μ_n and ν_n are the nodes of Bessel functions j_1 for LO and TO modes respectively. Therefore, the spatial confinement will produce discrete spectra obeying to the selection rules for Raman active modes $l = 0, 2; n = 1, 2, 3, ...$ where l and n are the spherical quantum numbers. In literature are already present publications which try to explain the experimental spectra with the theory reported above. In [20], based on the theory developed in [9], a cross check between theory and experimental data was carried out. In this case a fairly good agreement was obtained, but the study was carried out only for nanoparticles of only one average size. Therefore a more exhaustive investigation is needed.

2.5.3 Surface Phonons

As it was seen in the former subsection, the continuum model provides the normal modes of a dielectric small enough sphere which oscillates in its entireness. Nevertheless, the reduced dimensionality does not allow anymore to discern between surface an bulk, thus surface modes can be considered as an effect of quantum confinement as well. At the interface between a semiconductor and air or vacuum, the dielectric properties of the material changes in respect with the bulk ones. In polar semiconductors, surface phonons result to have frequency values between the ω_{LO} and ω_{TO}. However, due to the low surface volume ratio, in bulk semiconductors the surface phonons do not give a significant contribution to the scattering. In nanostructures, and especially in quantum dots, the surface volume ratio grows dramatically resulting in an important contribution to the scattering coming from the surface. As simplest case of surface vibrations, the plane surface will be taken into account. In the case of semiconductor-vacuum plane interface, the surface phonons dispersion relation is given by

$$\omega^2(q) = \frac{1}{2}\left[\left(\omega_q^2 + \omega_{LO}^2\right) \pm \sqrt{\left(\omega_q^2 + \omega_{LO}^2\right)^2 - 4\omega_q^2\omega_{srf}^2}\right] \tag{2.34}$$

where

$$\omega_q^2 = \frac{\varepsilon_\infty + 1}{\varepsilon_\infty}(ck)^2 \tag{2.35}$$

$$\omega_{LO}^2 = \frac{\varepsilon_0}{\varepsilon_\infty}\omega_{TO}^2 \tag{2.36}$$

$$\omega_{srf}^2 = \omega_{TO}^2\frac{\varepsilon_0 + 1}{\varepsilon_\infty + 1} \tag{2.37}$$

are respectively the light dispersion relations in the material, the limit value of TO and LO phonons frequencies (bulk frequencies) and the limit value of surface phonon frequency (infinite plane surface) [59]. Equation 2.34 and equations 2.35 are plotted in figure 2.12. The curves have been calculated using the literature values of CdS dielectric constants ε_∞, ε_0 [31], ω_{LO} and ω_{TO} [41]. In figure 2.12, the functions $\omega_1(q)$ and $\omega_2(q)$ are the solution 2.34 respectively with $-$ and $+$ signs before the square root [59]. The function $\omega_2(q)$ approaches the surface phonon frequency value $\omega_{srf} = 293.6$ cm^{-1} in the limit of large wavenumbers. Conversely, the function $\omega_1(q)$ deviates from the longitudinal phonon frequency $\omega_{LO} = 302.2$ cm^{-1} at the growing of k. Even though this model is relative to a plane interface between a dielectric with $\varepsilon(\omega)$ and the vacuum, it is useful to visualize the behavior of surface phonon even when the interface is no longer plane. From the experimental value of surface mode frequency ω_{SO}, a rough estimation of magnitude of wavevector $|\vec{k}|$ can be obtained. Rearranging the equation 2.34 in terms of ω_q one gets

$$\omega_q^2 = \frac{\omega_2^4 - \omega_2^2\omega_{LO}^2}{\omega_2^2 - \omega_{srf}^2} \tag{2.38}$$

where ω_2 is the function showed in figure 2.12. ω_2 coincides with the experimentally observed frequency of the surface mode ω_{SO}. Inserting in this expression the values of ω_{LO}=302.2 cm^{-1}, ω_{srf}=293.58 cm^{-1} (calculated above) and $\omega_2 \approx 270$ cm^{-1} (experimental), one gets the ω_q expressed in cm^{-1}. Dividing ω_q by the light dispersion in the material $[(\varepsilon_\infty + 1)/\varepsilon_\infty]^{1/2} \approx 1.1$ one finally obtains the wavevector in cm^{-1} (see graphic of figure 2.12). The wavevector is related to the periodicity of the of the surface mode, and consequently to the diameter of the spherical nanoparticle through the relation $\vec{k} \sim 2\pi/d$ [11]. Inserting the numerical values of frequencies

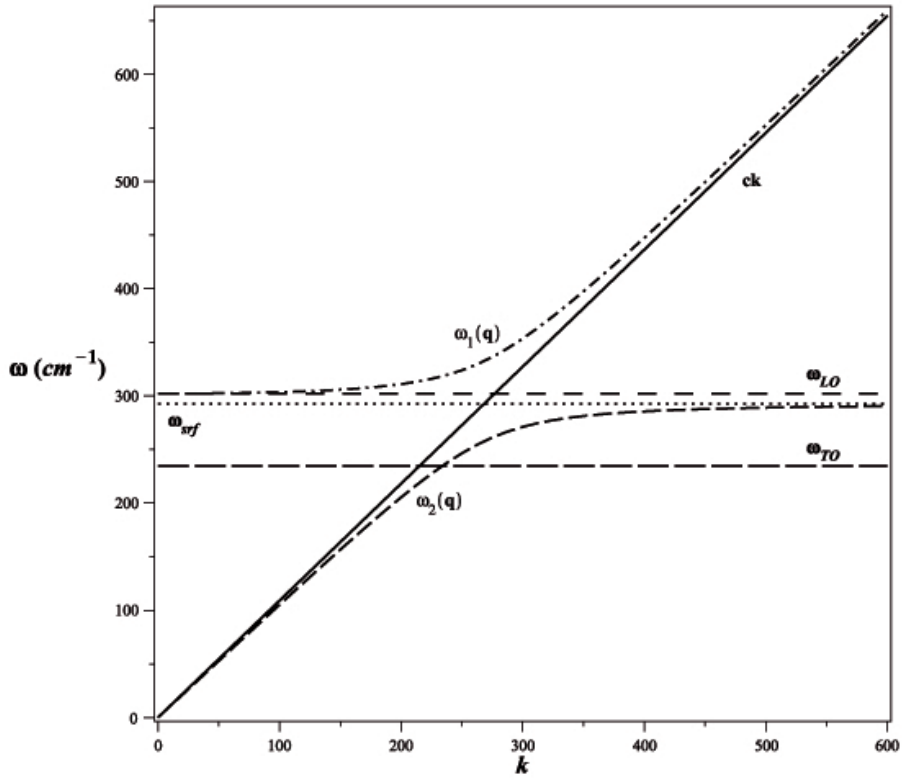

Figure 2.12: *Plot of equations 2.34, 2.35,* ω_{LO}*,* ω_{TO} *and* ω_{srf}*.* ck *is the dispersion of light inside the material,* ω_{LO} *and* ω_{TO} *are the frequencies of longitudinal and transversal phonons respectively, while* ω_{srf} *(dotted line) is the limit value of surface phonons frequency.* $\omega_1(q)$ *and* $\omega_2(q)$ *are the phonon dispersion relations at the varying of linear momentum* k*.* k *is expressed for convenience in* cm^{-1}*.*

reported above, one finds that the order of magnitude of the periodicity is in the range of 1-2 nm. It has a value comparable with the dimension of the studied nanocrystals. The upper relation can not be used to estimate the diameter, however, it is useful understand whether the light is able to select the surface phonon wavevector and provide information about the periodicity of the mode.

A more accurate calculation requires to take into account the symmetry possessed by the quantum dots, which for simplicity it has assumed to spherical. In the case of non plane interface, the boundary conditions change and the model must be readapted. According to [59] and [10], the interface between a dielectric sphere with $\varepsilon(\omega)$ and the surrounding dielectric media with ε_m, can be modelled as a dielectric sphere embedded in a dielectric surrounding. Similarly to the case of flat surface, the problem to determine the surface normal modes of a spherically symmetric crystal reduces thus to solve a boundary problem expressed by the Laplace equation $\nabla\phi = 0$, where ϕ is the electrostatic potential. In the more general case of two dielectrics, the surface modes of a small enough sphere are determined by the condition [10, 59, 60]

$$\frac{\varepsilon(\omega)}{\varepsilon_m} = -\frac{l+1}{l}, \quad l = 1,\ 2,\ 3, ... \tag{2.39}$$

where $\varepsilon(\omega)$ is the dielectric function of the material, while ε_m is the dielectric constant of the surrounding medium. Expressing $\varepsilon(\omega)$ in function of ω, the condition 2.39 becomes

$$\varepsilon_\infty \frac{\omega^2 - \omega_{LO}^2}{\omega^2 - \omega_{TO}^2} = -\frac{l+1}{l}\varepsilon_m, \quad l = 1,\ 2,\ 3, ... \tag{2.40}$$

rearranging equation 2.40, the expression of the surface phonon frequency in dependence of the quantum number l can be obtained [60]

$$\omega_l = \sqrt{\frac{(l\varepsilon_\infty\varepsilon_0 + (l+1)\varepsilon_\infty\varepsilon_m)\omega_{LO}^2}{l\varepsilon_\infty\varepsilon_0 + (l+1)\varepsilon_m\varepsilon_0}}, \quad l = 1,\ 2,\ 3, \dots \tag{2.41}$$

where ε_0 and ε_∞ are the static and infinite-frequency dielectric constants of the material. Thus, in Raman spectra the surface modes are expected to appear as spaced multi-peaks according to the function 2.41 reported in figure 2.13 Equation 2.41 does not depend explicitly from the radius of the sphere R, thus it can be applied without problems to arbitrarily small dielectric spheres. Furthermore, it results to be even simplified for very small dielectric spheres since it is possible to neglect the retardation effects due to the finite value of speed of light. From the plot in figure 2.14 (left hand side), it can be seen that the surface modes will be located where $\varepsilon(\omega) < 0$. This condition holds only in a particular frequency range where k is imaginary and the longitudinal waves decay exponentially. Thus, the waves can not propagate into the bulk and only the surface modes can exist. It will result thus, that for a certain symmetry mode we will have $\omega_{TO} < \omega_l < \omega_{LO}$. It can be observed how the ω with $l = 1,\ 2,\ 3, ...$ and ω_{srf} depend on the matrix material, in particular, the frequencies shift toward lower frequencies at the increasing of ε_m. The ratio between the intensity of the surface mode peak and the bulk mode increase at the decreasing of the particle size. This can be explained simply by the fact that, at the decreasing of the size the surface-volume ratio will increase drastically enhancing the surface phonons contribution. The mode ($l = 1$) is expected to have the highest intensity [10] since it is a dipolar oscillation and has the strongest interaction with the electromagnetic field. In Raman spectra of CdS quantum dots, but more in general in Raman spectra of II-VI

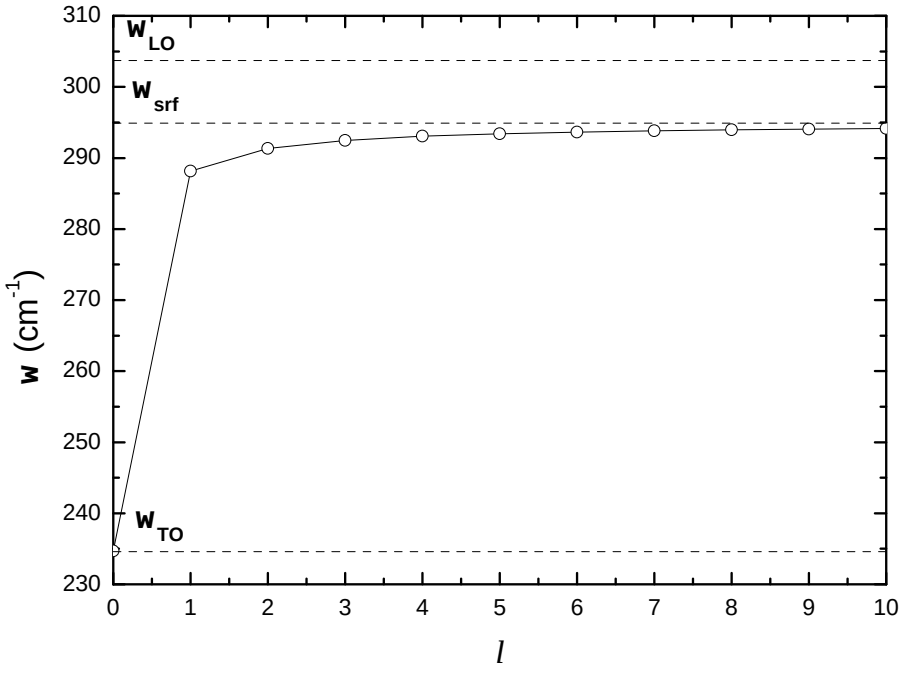

Figure 2.13: *Calculated dependence of cadmium sulfide surface mode (ω_l) from quantum number l for three values of ε_m.*

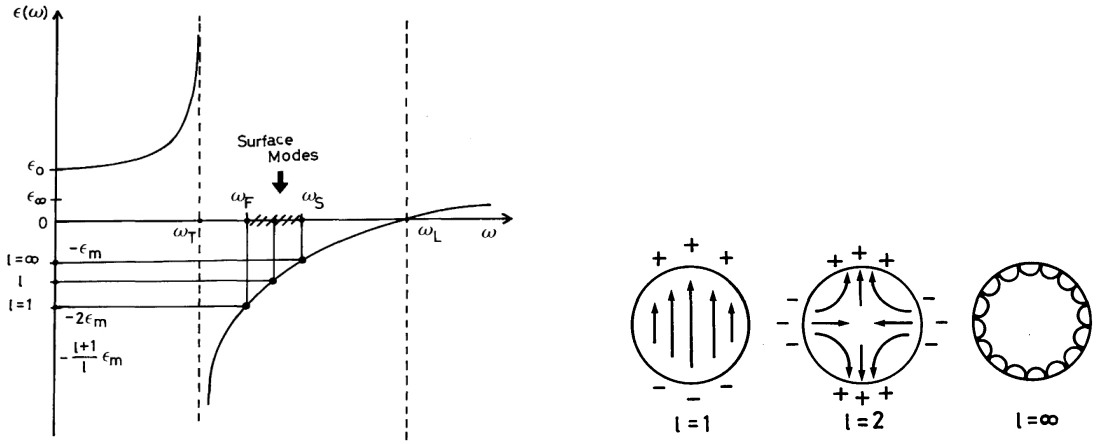

Figure 2.14: *(Left hand side) Plot of the imaginary part of $\varepsilon(\omega)$ in function of the frequency ω taken from [10]. At the values of quantum number l ranging in the interval $1 < l < \infty$, values of surface modes frequencies ranging from ω ($l = 1$) to ω_{srf} correspond. (Right hand side) Electrostatic field patterns in a sphere approximating a nanoparticle taken from [10, 59]. It can be seen how the mode becomes more and more localized on the surface at the increasing of the quantum number l.*

quantum dots, this mode appears as a shoulder of the LO mode with intensity much lower than the bulk mode (LO) [16, 17, 23]. One finds from the Raman scattering experiments, that such modes appears at $\sim$270 cm^{-1}. It can be assigned to the spherical surface mode with $l = 1$, just because as discussed above, it is the surface mode with the highest intensity.

Chapter 3

Growth of CdS Quantum Dots

The semiconductor nanocrystals (quantum dots) can be grown following numerous synthetic approaches. The most widely used methods are the epitaxial growth, the colloidal growth in all its variants, the electrodeposition from solutions [61], sonochemical growth [62], microwave-induced deposition [63], etc. Among these techniques, the first two have however a larger importance. The epitaxial growth can be carried out by Metal Organic Vapor Phase Epitaxy (MOVPE), or by metal beam epitaxy (MBE). These two techniques were originally developed to grow very thin layer of semiconductors and later quasi 2-dimensional nanostructures. Nevertheless, with proper strategies, epitaxial growth can be used also to grow quasi 1- and quasi 0-dimensional nanostructures. The quasi 0-dimensional nanostructures, are grown exploiting the Stranski-Krastanow and Volmer-Weber principles [64, 65]. They are based on the self organization of nanostructure induced by the lattice mismatch existing when two different materials are grown epitaxially. IV and III-V semiconductor quantum dots were grown successfully by self-organized growth [66–68], and according to some reports [69–71], II-VI semiconductor quantum dots were also grown by self-organized growth. The quantum dots produced by these methods have irregular shape, broad size distribution an large size (often referred as quantum islands). Only recently these problems have been solved by using lithography-prepatterned substrates [72]. The epitaxial growth requires however large and expensive facilities and extreme environmental condition (vacuum, clean atmosphere, etc.) which make increase the production cost.
By the colloidal growth it is possible to grow a wide spread of semiconducting materials quantum dots as well as metal quantum dots. By controlling the growth physical and chemical parameters, it is possible to finely control the growth and thus to obtain quantum dots with small size, narrow size distribution and desired stoichiometry. Therefore, the colloidal growth presents numerous advantages in respect to epitaxial growth, and it was chosen to grow the CdS quantum dots.

3.1 Introduction to Colloidal Growth

The colloidal growth is based essentially on the decomposition of the metal precursor in a liquid medium, and the successive controlled recombination of the metals (ions). The colloidal growth can be carried out in organic, aqueous, polymeric or in a molten glassy matrix. In the organic media, the decomposition of organic metal precursor occurs via thermal pyrolysis [1, 73, 74], whereas in aqueous media the compound is formed precipitating it by the saturation of the inor-

ganic salt solution [75–77]. Similar principles are involved in the growth performed in polymer or gelatin matrices [78]. However, in any case, the growth needs to be properly controlled in order to have nanostructures. This is done mainly using in the reaction environment suitable surfactant molecules which coat the just formed nanoparticle surface controlling their growth, coalescence, oxidation and make them soluble in the solvent. For the synthesis in organic media the surfactant molecules are usually long chain organic fatty acids, phosphonic acids, amines, thiols or organic phosphine and their oxides which bind covalently on the surface with their polar atoms (e.g. O, N, S, P) and create an hydrophobic shell around the nanoparticle. For the syntheses in aqueous media, the surfactants used are commonly short-chain organic molecules (2-3 atoms of carbon) such as thioalcohols, thiocarboxylic acids, dithiols, thioglycols, and thioglycerols. These molecules have the reverse function of the long-chain organic molecules, in fact they bind covalently on nanoparticles surface by their sulfur atom creating around them a hydrophillic shell constituted by -OH, -COOH and/or -SH group itself which make the nanoparticles solvable in water.
In respect with epitaxial techniques the colloidal growth has several advantages such as low cost facilities (only standard chemistry glassware is needed), possibility to produce large amount of material, small sizes, high cristallinity and surface modifiable nanoparticles can be produced. Nevertheless, the main advantage is that the growth can be size selective varying parameter as temperature, precursors type and their concentration, surfactant type and its concentration but mainly varying the reaction time. From a comparison between colloidal growth in organic and aqueous media one finds that the crystallinity of the produced nanoparticles is higher in the organic media synthesis rather than in aqueous synthesis because of the higher temperatures used (above 300- 400 °C vs ambient T). Nevertheless in this case the synthesis is much more sophisticated due to the use of high boiling point solvents, inert atmosphere, oxygen free environment and injection techniques. However, latest reports [79–81] show that is possible to growth high crystallinity nanocrystals also in aqueous media. This is done using the so called hydrothermal technique where the growth is realized in autoclave at high temperature above $100\,^{\circ}C$ and high pressure. Concerning the crystallinity of the grown nanocrystals, this method is competitive with the organometallic synthesis.
In this work of thesis all CdS quantum dots samples have been prepared by colloidal growth in organic media because this kind of synthesis ensures a high quality nanocrystals. Moreover, it mainly allows to control in a very good way the nanoparticle size which is fundamental for the type of investigation done on those samples.

3.2 Chemical-Physics Principles of Colloidal Growth

3.2.1 Thermodynamics of Colloidal Growth

The first experimental data based model which describes the process of colloidal growth was the LaMer's model [82]. This model was formerly developed for a slow rate process but it can be successfully applied also to faster processes, like the growth in organic media at high temperature [73].
The LaMer's model divides the monodisperse growth in four phases shown in figure 3.1; the injection, the nucleation, the growth and the ripening. The entire process begins with the injection of one of the precursor (the second is already in the vessel), as result one has a concentration

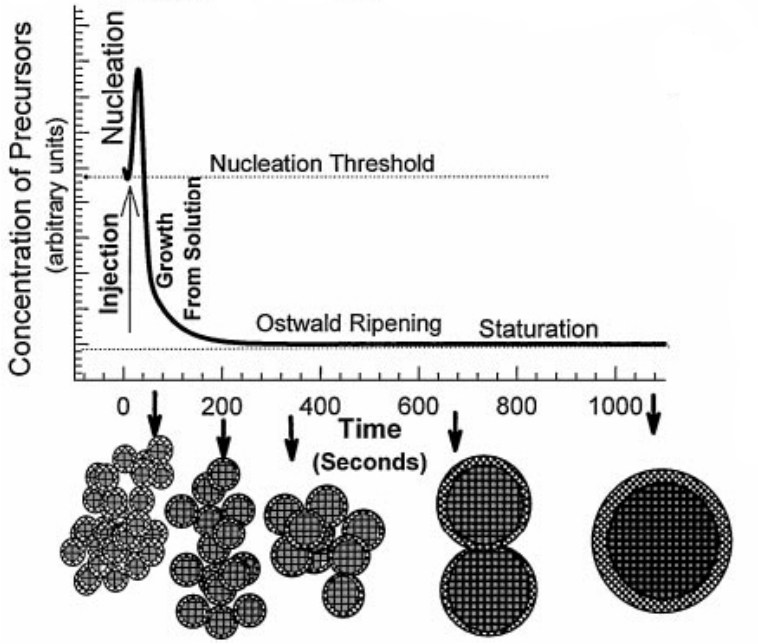

Figure 3.1: *Cartoon depicting the process of growth according to LaMer's model [82]. The spheres at the bottom of the graphic represent the evolution in diameter of the nanocrystals, starting from small nucleation clusters to largest nanocrystals. Elaborated from [73].*

burst in the reaction vessel reflecting the rapidity of the injection. When the concentration of the precursors reach a certain value, one has the supersaturation condition

$$\Delta\mu = \mu_{solid} - \mu_{liquid} = kTln\frac{C}{C_0} \tag{3.1}$$

where μ_{solid} and μ_{liquid} are the chemical potentials of the bulk solid and liquid monomer, C and C_0 are the real and equilibrium concentration of the monomer respectively and kT is the thermal energy. Equation 3.1 is however valid only assuming the solution as ideal.
When the value of supersaturation concentration C_{SS} (nucleation threshold) is overcome the nucleation process takes place. In the nucleation there is the formation of a new phase consisting in very small atoms aggregates (hundreds of atoms) called nuclei whose continually form and redissolve in a dynamic equilibrium. Thermodynamically, the nucleation occurs when at constant T, the Gibbs free energy ΔG is < 0. Its expression is

$$\Delta G(r) = -n(\mu_{solid} - \mu_{liquid}) + 4\pi r^2\gamma \tag{3.2}$$

where r is the radius of the droplet, γ the surface tension coefficient and n the number of atoms contributing to the formation of the cluster. Keeping in mind that $n = 4/3\pi r^3\rho$, the equation 3.2 can be written as

$$\Delta G(r) = -\frac{4}{3}\pi r^3\rho(\mu_{solid} - \mu_{liquid}) + 4\pi r^2\gamma \tag{3.3}$$

where ρ is the density of the material. In the first term there is the contribution of the supersaturation and the volume of the droplets while in the second, the contribution given by the

surface tension. In order to have thermodynamic stability of the new phase (solid clusters), $\mu_{crystal} < \mu_{solution}$ must be valid. The minus sign before the first term of equation 3.2 allows a gain of free energy. At small radii, the surface effect is dominant making the $\Delta G(r)$ rise, while at larger radii the it decreases becoming negative. The function $\Delta G(r)$ therefore has a maximum at a certain critical radius r^* given by

$$\frac{\partial \Delta G(r)}{\partial r} = 0 \tag{3.4}$$

$$r^* = \frac{2\gamma V_{cry}}{\Delta\mu} \tag{3.5}$$

where V_{cry} is the volume of the crystal. Equation 3.4 is known as the Gibbs-Thomson equation which gives the condition of equilibrium between the solid phase (clusters) and the solution. Yet, it is more often reported in terms of concentration of precursors in equilibrium with the solid phase (nanocrystals) as

$$C(r) = C(\infty) \exp\left(\frac{2\Omega_{solid}\gamma}{Rk_bT}\right) \tag{3.6}$$

where C_∞ is the concentration of monomer (in molecules per unit volume) that would be in equilibrium with a flat bulk solid, and Ω_{solid} is the molecular volume of the solid material. This equilibrium is however metastable and if some atom joins or leaves the nanocrystal, it is immediately perturbed making decrease or increase $\Delta G(r)$. This will bring to a growth of clusters in the first case, and to a redissolving of them in the second. It is then straightforward from the expression of critical radius 3.4 that the critical free energy is

$$\Delta G^* = \frac{16\pi}{3}\frac{\gamma^3 V^2}{\Delta\mu} \tag{3.7}$$

where V is the volume of the nanoclusters. Equation 3.7 gives the energy barrier that must be crossed in order the growth takes place. To notice that the critical free energy is inversely proportional to the square of the supersaturation $\Delta\mu$.

Once such barrier is overcome, the material provided by the precursors decomposition join the small clusters and the nanocrystals start to grow. This stage of the reaction proceeds until all the free precursors are consumed, i.e. $C \to 0$. The nanocrystals size distribution depends strongly on the initial nuclei size distribution, in particular on the time over they are formed. It is thus straightforward that injection time plays an important role for this aspect, thus, the shorter is the injection time, the narrower will be the size distribution.

At the end of the growth, when both precursors have been consumed, a thermodynamic equilibrium between the nanoparticles and the solution will be established. However, this is a dynamic equilibrium. Due to the higher surface energy possessed by smaller nanoparticles, they slowly disappear providing new material for the larger ones which further grow. This process, known as Ostwald ripening starts at longer times when the precursors concentration tends to an equilibrium constant value (close to zero), see figure 3.1. Quantitatively the process is expressed as follow

$$C(r) = C(\infty) \exp\left(\frac{\lambda_c}{r}\right) \tag{3.8}$$

The former equation relates the solubility of nanoparticles to their radius. $C(\infty)$ is the solubility of the bulk material while the constant λ_c is the capillary length expressed as

$$\lambda_c = \frac{2k_a\gamma\Omega_m}{3k_vRT} \tag{3.9}$$

where, Ω_m is the molar volume of the dispersed phase, γ is the interfacial tension, R is the universal gas constant, T is the absolute temperature and k_a and k_v are the area and volume shape factors respectively. The Ostwald ripening theoretically brings thus to a more uniform size distribution but also to larger nanoparticles so that for very long ripening times bulk-like crystals can be obtained (radius above 10 nm of radius).

3.2.2 Kinetics of Colloidal Growth

In the description of monodisperse growth kinetics, the sequence of the rate determining steps is constituted by the diffusion of the monomer in the solution, in the interfacial layer and finally the dynamics of the reaction at the nanocrystal surface. The diffusion through the spherical interfacial layer is the process which mostly affect the velocity of diffusion. The monomer diffuses in this zone according to Fick's first law

$$J = 4\pi r^2 D\nabla r \tag{3.10}$$

Where J is the flow of matter through the imaginary spherical barrier, r is the radius of the nanocrystal while D is the diffusion coefficient. Integrating it between r and $r+\delta$, where δ is the thickness of the interfacial layer, and rearranging, one gets the following expression for first-order rate reaction [83]

$$\frac{C_i - C_e}{C_b - C_i} = \frac{D}{kr}\left(1 + \frac{r}{\delta}\right) \tag{3.11}$$

where C_i and C_e are the initial and equilibrium concentrations of the monomer, while C_b is the concentration bulk concentration of the monomer. For this equation two cases must be distinguished; the diffusion-controlled growth and the reaction-controlled growth. In the first case $D \ll kr$, i.e. the diffusion is much slower than the chemical reaction itself so that the diffusion becomes the rate determining step and the kinetic equation can be written as

$$\frac{dr}{dt} = D\Omega_m\left(\frac{1}{r} + \frac{1}{\delta}\right)(C_b - C_e) \tag{3.12}$$

where Ω_m is the molar volume of the solid. This equation is applicable to the cases where the diffusion of the monomer is very slow as in the growth of nanocrystals in molten polymeric or glassy matrices. Conversely, when the growth is performed in liquid organic solvent in presence of surfactants, the diffusion is much faster, $D \gg kr$, so that it does not represent the rate determining step. With this condition the kinetic equation becomes

$$\frac{dr}{dt} = D\Omega_m\left(C_b - C_e\right) \tag{3.13}$$

The model above is therefore suitable to describe the growth of CdS quantum dots in 1-octadecene, since the diffusion of organo-metallic monomers like cadmium stearate in this kind of solvent

results to be fast [74] so that the process is reaction-controlled. From these findings, the colloidal growth of monodisperse CdS can be dealt similarly to any chemical reaction. Neglecting the presence of the surfactant, a typical reaction involved in quantum dots growth can be written as

$$\mathrm{Cd(SA)_2} + \mathrm{S^{2-}} \xrightarrow{k} \mathrm{CdS} \tag{3.14}$$

The kinetic equation can be immediately derived as follows

$$\frac{d[\mathrm{Cd}]_t}{dt} = -kA(t)[\mathrm{Cd}]_t N(t) \tag{3.15}$$

where k is the interfacial rate constant, $A(t)$ is the surface area, $N(t)$ is number of particles, while $[\mathrm{Cd}]_t$ is the time varying cadmium precursor concentration. Equation 3.15 is valid only assuming that the nucleation is much slower than the mass transfer process (diffusion in the solution)[74].
When the size of nanocrystals reaches the critical value r^*, one has a steady-state where there is no longer formation of nuclei (its number remains constant along time ($N(t) = N_0$), and the precursors decompose only on the already formed nuclei providing them material for the growth. Assuming the particle to have a spherical symmetry, the surface area is $A(t) = 4\pi r(t)^2$ and growth rate equation becomes

$$\frac{dr}{dt} = k\left(\Omega_m([\mathrm{Cd}]_0 - [\mathrm{Cd}]_{eq}) - \frac{N_0 4\pi r^3}{3}\right) \tag{3.16}$$

Here $4[\mathrm{Cd}]_t$ has been replaced by $\Omega_m[\mathrm{Cd}]_0 - [\mathrm{Cd}]_{eq}$. This means that the time dependent cadmium concentration is the difference between cadmium concentration at the beginning and at equilibrium $[\mathrm{Cd}]_{eq}$ which depends on particle radius. Moreover, Ω_m the molar volume of the material while k is the kinetic constant already seen in equation 3.14. The differential equation 3.16 has a complicate and not explicit solution [74] and it will not be reported here but it can be read as follow: The surface area of each nanocrystal increases over time and this tends to accelerate the reaction rate, but at the same time there is a depletion of Cd and S monomers concentration, which causes the growth rate depletion. Therefore, during the initial instants, the particles mean radius grows almost linearly, the radius goes approximately as $r(t) = \sqrt{r_0 + K \cdot t}$ with $r_0 \approx r^*$. At longer growth times it tends asymptotically like $r \sim \sqrt{K \cdot t}$ [43, 84] to its maximum value $r_{max} = (3V_m[\mathrm{Cd}]_0 - [\mathrm{Cd}]_{eq})/N_0 4\pi$. At this point, the Cd left in solution will be only the amount in equilibrium with the solid phase.

3.2.3 Quantum Dots Size Distribution

The very big advantage of the colloidal monodisperse growth is that is possible to grow quantum dots with a very narrow size distribution. This can be achieved tuning properly the concentration or the type of coordinative molecule (surfactant), the precursors concentrations, the temperature of growth and the rapidity of the monomer injection. The size distribution can be further narrowed by solvent-selective precipitation and by ultracentrifugation [85].
According to [84], the size distribution can be determined in a different way during the nucleation and during the growth phase respectively. Figuring out to quench the reaction during the nucleation phase, the nuclei would result to have a gaussian size distribution around the value of critical radius r^*

$$P(r) = P_0 \exp\left(-\frac{4\pi\gamma(r - r^*)^2}{3kT}\right) \tag{3.17}$$

with γ the surface tension. Equation 3.17 can be normalized as follow

$$P(r) = \frac{1}{\sqrt{2\pi}\Delta r} \exp\left(-\frac{4\pi\gamma(r - \langle r\rangle)^2}{2\Delta r}\right) \tag{3.18}$$

where $r^* = \langle r\rangle$ is the average value of radius. It follows immediately the standard deviation of the nanocrystals radius

$$\Delta r = \sqrt{\frac{3kT}{8\pi\gamma}} \tag{3.19}$$

These equations can be used in both direction, i.e. from statistical analysis of TEM images one can determine parameters such as the surface tension γ, the supersaturation value of the chemical potential $\Delta\mu$, the critical free energy ΔG^* thus the critical radius r^*. At the same time they can be helpful in the choice the best growth physical conditions to have a narrow distribution and particles of the desired radius. At the stage where the supersaturation is negligible (few ions in solution) and the total mass of the semiconductor is considered to be constant, other causes will affect the size distribution. The diffusion rate and the reaction rate become important, and the size distribution can not be described by a gaussian anymore. In the diffusion-controlled growth case the size distribution takes the form of the equation derived by in [86]

$$W(u) = \begin{cases} (3^4 e/2^{5/3})u^2 \exp\left(\frac{[-1/(1-2u/3)]}{[(u+3)^{7/3}(1.5-u)^{11/3}]}\right) & \text{if} \quad 0 < u < 1.5 \\ 0 & \text{otherwise} \end{cases} \tag{3.20}$$

where $W(u) = W(r/r^*)$. Equation 3.20 describes the size distribution of nanocrystals grown in a glassy matrix where the diffusion is the rate determining step. Nevertheless, for the colloidal growth in solution, where the growth is mostly reaction-controlled it is more useful to take into account the model derived by Wagner [87]

$$W(u) = \begin{cases} 2^7 3u(2-u)^{-5} \exp\left(\frac{-3u}{(2-u)}\right) & \text{if} \quad 0 < u < 2 \\ 0 & \text{otherwise} \end{cases} \tag{3.21}$$

As it is visible in figure 3.2, the size distribution is asymmetric and it has a mean value $\langle r\rangle = 8/9r^*$ [88]. These two models try to explain the physical origin of the asymmetric size distribution which the nanoparticles will have at the end of the growth. Although, experimentally other phenomena occurs in the process of growth, and the size distribution quoted above may be no longer respected. It is quite common that in the case of colloidal growth (organic media) the size distribution has an asymmetric shape with the tail extending toward larger diameters [89]. This unexpected asymmetric broadening may be caused principally by the slow cooling rate of the growth solution. Referring to the Gibbs-Thomson equation 3.6, it can observe that the precursor concentration goes like $\sim \exp(1/T)$. Therefore, to a temperature decreasing will correspond a sudden increasing of the nanoparticles solubility. In addiction, the smallest nanoparticles will be solved more easily than the largest ones due to their higher surface energy, while the largest ones will be further accreted even though with a decreasing rate. However, the temperature drop is very rapid, especially with the method of aliquot extraction adopted here, see subsection 3.3.4. This will deactivate kinetically the reaction fairly soon freezing the size distribution scenario which is observable in the statistical distribution as an excess of nanoparticles further accreted (larger diameters tail), see paragraph 5.1.2. This behavior is not consistent with the Wagner distribution described by equation 3.21 and the fitting

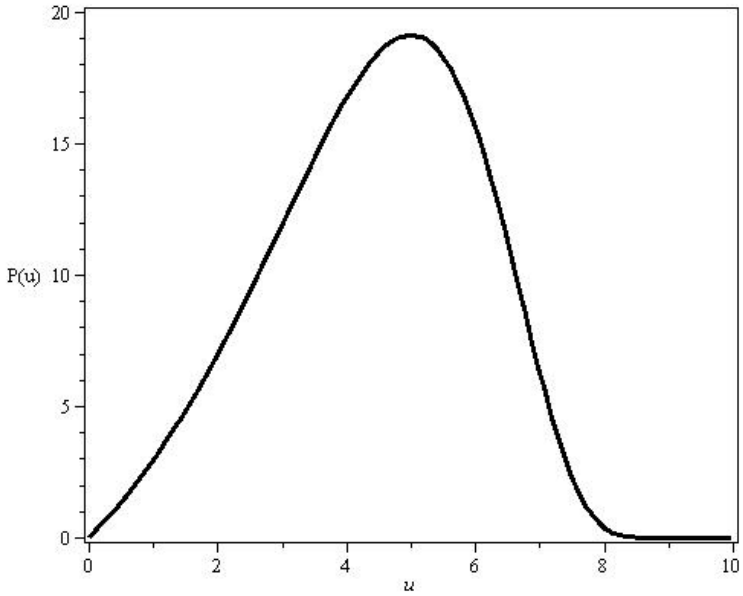

Figure 3.2: *Asymmetric size distribution calculated in* $r^* = 5$ *for reaction-controlled colloidal growth.*

of the experimental data requires the use of other continuous distribution functions. In some publications about quantum dots grown on a substrate by self-organized growth, the Gamma distribution has been used [90, 91]. Concerning quantum dots grown by colloidal methods, Gaussian or asymmetric distributions have been used [89]. The statistical analysis performed on TEM images of CdS nanocrystals grown according the procedures reported in 3.3 shows their asymmetric diameter distribution, see chapter 5. In order to obtain the quantum dots mean diameter values, the statistical diameter data have been fitted with an asymmetric distribution function.

3.3 Experimental

3.3.1 A Review of II-VI Quantum Dot Growth

As already mentioned the II-VI semiconductor nanocrystals are produced using the organic media based monodisperse colloidal growth. After the introduction of such methods since 1993 by Murray et al. [1] several variations have been developed in order to improve the crystallinity of the nanocrystals ad narrow the size distribution.
Such synthesis consisted in the co-pyrolysis of dimethylcadmium and trioctylphosphine selenide (TOPSe) in an high boiling point solvent 1-octadecene using as surfactant trioctylphosphine oxide (TOPO). The selenium organic precursor was prepared solving metallic selenium in trioctylphosphine (TOP) under inert atmosphere then it was subsequently injected by a syringe into the reaction vessel always kept under inert atmosphere. The heat provided by the high temperature $\sim$300 °C allows the metal-organic compounds to decompose providing free Cd and Se which combine giving CdSe nanocrystals. In order to have nanocrystals the use of trioctylphosphine oxide (TOPO) as surfactant molecule was introduced. It binds by a coordinative bond made up by the oxygen lone pairs and empty d orbitals of the cadmium on the

nanocrystals surface. The bond is however weak and easily breakable allowing a subsequent exchange of the coating layer.
The use of dimethylcadmium as Cd precursor is however limited due to its high volatility and to its tendency to decompose into metallic cadmium so that new kind of precursors were introduced. Fatty acids or phosphonic acids cadmium complexes or salts are good replacements of $(CH_3)_2Cd$ thanks to their solubility in high boiling point solvents like 1-octadecene, low volatility at high temperatures (∼300 °C), and at the same time the surfactating properties due to the long chain carbon atoms. They can be easily prepared by the reaction at high temperature in an organic solvent between the organic acids (fatty or phosphonic) and CdO or cadmium inorganic salts of weak conjugated bases (e.g. $(CH_3COO)_2Cd$, $CdCO_3$). The use of organo-phosphonic acids is however limited by their high price. Therefore fatty acids Cd salts are actually the most used in particular stearic acid and oleic acid (18 carbon atoms) due to their structural affinity with 1-octadecene [92].
The preparation of group VI precursors is much more critical than the one for group II precursors, the standard procedure always introduced by [1] consists in solving metallic chalcogen (Se, Te) in TOP forming TOPSe, TOPTe. This reaction must be always performed under inert atmosphere due to the high air sensitivity of TOP and for this reason glove-box must be used in order to prevent TOP oxidation (self-ignition). TOP as its relative oxide TOPO may also have a role as surfactant, because after the release of chalcogen it binds covalently on the nanocrystal surface building up the protective organic shell. Also tributylphosphine (TBP) is sometimes used to prepare chalcogens precursors [39, 93], but TBP is even more air sensitive than TOP and has a negligible effect as surfactant. Even though sulfur belongs to chalcogens group and has similar chemical properties to Se and Te, the precursor is quite different. The first reports on this kind of synthesis [94, 95] took into account the use of trimethylsilane sulfide $(TMS)_2S$ which is still air sensitive as well as very expensive. A more practical and simple method introduced in [96] consists in solving very pure elemental sulfur in 1-octadecene. This method is not air sensitive and can be performed even in air. Going more in detail, the reaction at the basis of this method is the dehydrogenation of the 1-octadecene done by sulfur and the consequent formation of H_2S (hydrogen sulfide) that is the final source of sulfur. The two disadvantages of this method are that the solution to inject into the reaction vessel is already hot (T∼100 °C), making loose the quenching power that a cold solution could have. Moreover, the needed stoichiometry might not be respected since some sulfur will leave the solution as gaseous H_2S.

3.3.2 Chemistry of the Processes

The method used in this thesis to grow CdS nanocrystals has been partially derived from [96]. The chemistry involved in the preparation of cadmium and chalcogen precursors is quite simple. Concerning the preparation of the cadmium precursor, it consists in the reaction at high temperature between CdO and the fatty carboxylic acid, octadecanoic acid, more commonly known as stearic acid (SA). The reaction is carried out in 1-octadecene ($CH_2{=}CH(CH_2)_{15}CH_3$), an high temperature boiling point oleofin (T_b=315 °C) with a molecular structure very similar to the one of stearic acid.
The equation of this chemical reaction is

$$CdO + 2\,C_{17}H_{35}COOH \longrightarrow Cd^{2+}(C_{17}H_{35}COO^{-})_2 + H_2O \tag{3.22}$$

The preparation of the chalcogen precursor, in the specific case sulfur, is done separately solving elemental sulfur S_8 in 1-ODE at moderated high temperatures (∼100 °C). In reality, there is not

only the mere solvation of S_8 molecules, rather one has a series of non-stoichiometric chemical reactions between the same own S_8 and 1-ODE which bring to the formation of hydrogen sulfide (gas) and a mixture of unsaturated oleofins deriving from the former 1-octadecene. According to the general equation valid for all oleofins

$$S_8 + 8\,C_nH_{2n+2} \longrightarrow 8\,H_2S + 8\sum_{i=1}^{n} A_i C_nH_{2n-2i} \tag{3.23}$$

where A_i is a statistical coefficient which decreases at the growing of index i. This coefficient is necessary to account the less and less probable multiple dehydrogenation of the organic molecule. Therefore, one has the dehydrogenation of the oleofin operated by S_8 giving H_2S which is the real sulfur precursor solved in the same organic solvent (1-ODE). Furthermore, to remark that the stoichiometry is more complicated then one the reported in equation 3.23 because the dehydrogenation occurs randomly on the different zones of the molecule or on already partially dehydrogenated 1-ODE molecules.
Once the sulfur solution mixes with the cadmium precursor solution, according to the kinetics of the reaction described in 3.2.2, one has the growth of CdS nanocrystals ruled by the following balance of masses.

$$Cd^{2+}(C_{17}H_{35}COO^{-})_2 + H_2S + TOPO \longrightarrow CdS{-}TOPO + 2\,C_{17}H_{35}COOH \tag{3.24}$$

The TOPO does not really take part to the reaction in the sense that it is not really transformed. However, in the final products it appears bound to the QDs surface anyway thanks to the weak bonds established between the oxygen lone pairs of TOPO and the dangling bonds of Cd on the QDs surface [97]. Also the stearic acid provided by the cadmium stearate decomposition forms a similar bond with the QDs surface. Therefore, it partially contributions to the formation of the organic coating shell, but without deeper investigations it is difficult to estimate the ratio between TOPO and stearic acid on the nanocrystal surface. The quantum dot profile is shown in figure 3.3.

3.3.3 Experimental Setup for the Synthesis

The experimental setup for mono-disperse colloidal growth is relatively simple, so that such kind of synthesis can be carried out in every sufficiently equipped chemistry laboratory.
The glassware used for the synthesis is constituted by a 100 ml multi-necked spherical flask on which are mounted the column refrigerator with gas outlet on top (central flange), the inert gas inlet, a mercury thermometer (scale 300 °C) and a rubber septum (lateral flanges). The flask is positioned into a hollow hemispherical aluminium block in thermal contact with a stirring hotplate. This construction delivers the necessary amount of heat to the solution whose temperature can be brought above 300 °C. In between of the glass flask and the hemispherical hollow aluminium block a glass fiber tissue has been placed in order to have a more uniform distribution of the heat. The hotplate is equipped with a magnetic stirrer which allows to properly stir the organic solution by a teflon coated magnet in order to have no concentration gradients of precursor and surfactant. A vigorous stirring is particularly important during the injection phase.
The injection is done by a 5 ml Pyrex glass syringe equipped the stainless steel needle. The solution is injected into the reaction vessel throughout a natural rubber septum mounted on one of the lateral necks. This will prevent from air contamination of reaction environment. Another similar syringe with a longer needle was used to take aliquots of solution during the growth.

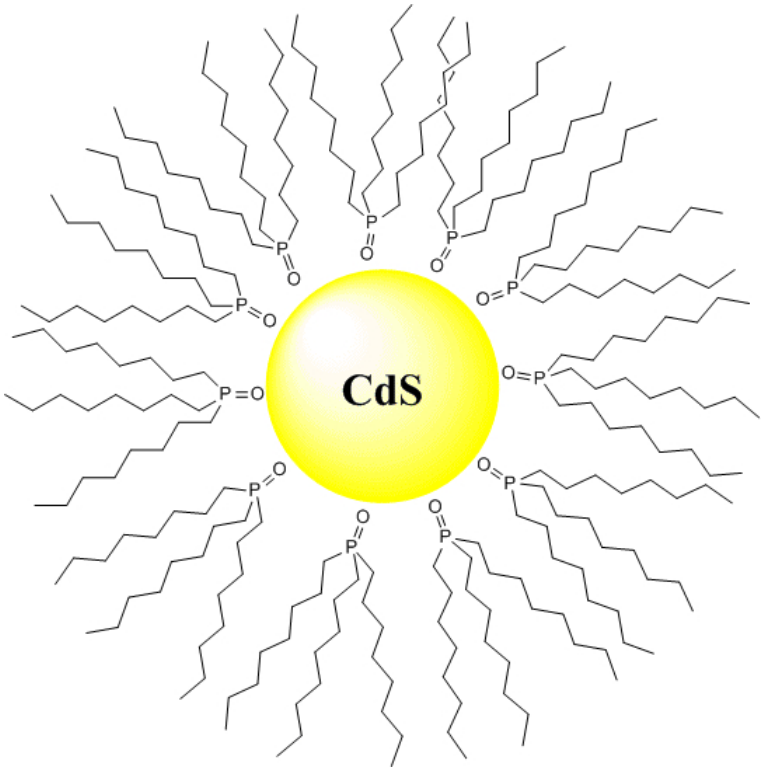

Figure 3.3: *Picture of an ideally spherical CdS quantum dot coated by trioctylphosphine oxide molecules.*

3.3.4 CdS-Nanocrystals Growth

The standard preparation route accounts as a first step, the preparation of the cadmium-stearic acid complex or cadmium stearate. 0.1 mmol of cadmium oxide (CdO) 99.999% metal basis, 2.1 mmol of technical grade stearic acid 90% and 50 ml of technical grade 90% 1-octadecene obtained by Alfa Aesar was loaded in the three necked flask, see see figure 3.4. At this stage, also trioctylphosphine oxide (TOPO) is loaded in the reaction flask even though it will not have a role in the dissolution of CdO. Its presence will be of fundamental importance during the successive growth. The molar ratio of the weighted substances have been calculated in accordance with the stoichiometry of the reactions, see subsection 3.3.2, but a more extended discussion has to be done for the TOPO molar ratio to use. As already discussed in subsection 3.3.2, the TOPO does not really take part to the reaction of nanocrystal formation, however, it will bind by a labile covalent bond on the nanocrystal surface [97, 98]. Therefore its concentration will strongly affect the final size of the nanocrystals. The quantity of TOPO to use in order to have nanocrystals with the wanted size can be estimated making opportune geometrical, chemical and stoichiometric considerations. According to [99], the wurtzite II-VI semiconductor nanocrystals have a complex shape of a hexagonal prism capped with two frustums 3.5, however, to simplify the calculations, here it will be approximated as spherical. Knowing that the TOPO molecules bind exclusively with the cadmium dangling bonds on the surface, from the lattice parameters of CdS it can be calculated the number of free Cd atoms on the surface. They are also in relationship with the volume of the nanocrystal, thus with the amount of cadmium precursor used. With these considerations, it can be established a relationship between the ratio mol(CdO)/mol(TOPO) and the nanoparticle mean radius. Considering that the moles number

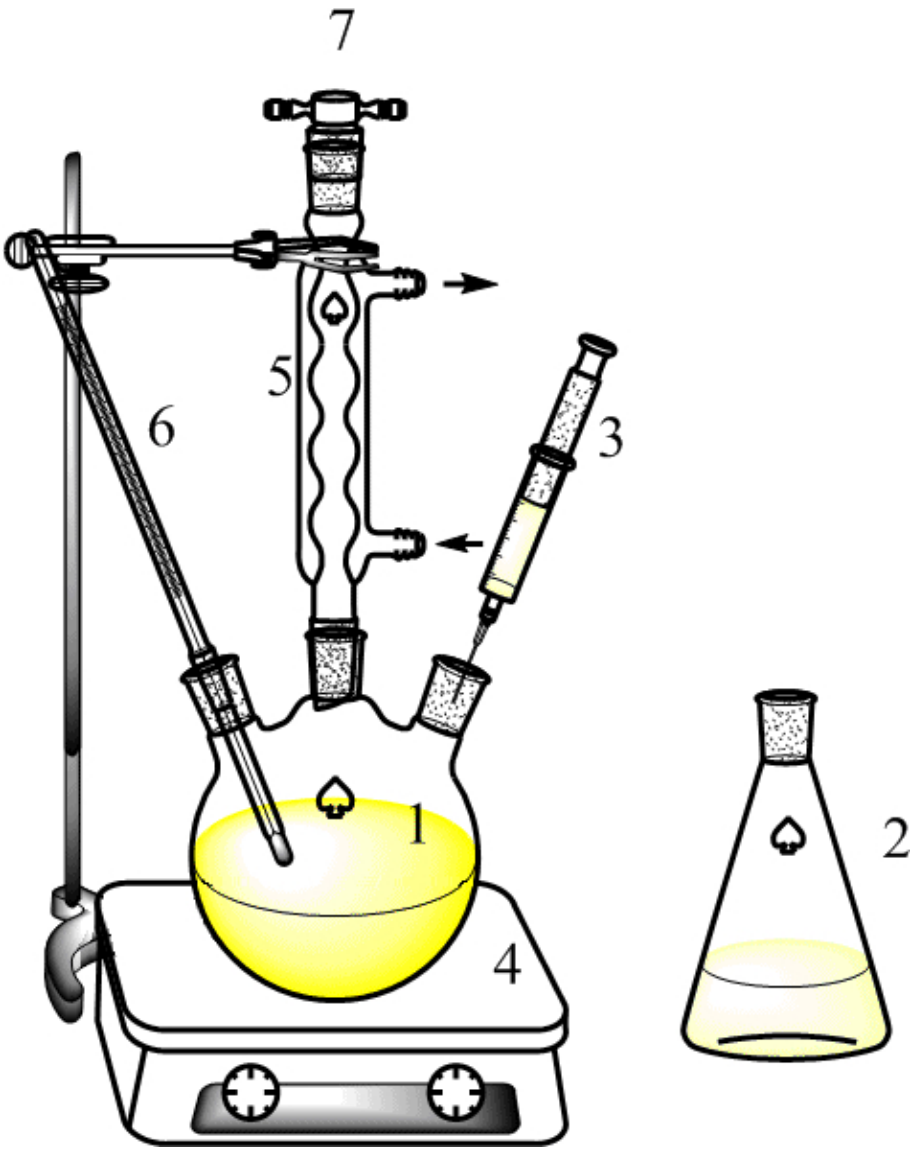

Figure 3.4: *Picture of colloidal growth setup. 1-100 ml spherical flask loaded with a solution of cadmium stearate and trioctylphosphine in 1-octadecene. 2-solution of elemental sulfur S_8 in 1-octadecene at ∼100 °C. 3-Pyrex syringe to inject the sulfur solution. 4-Stirring hot plate, max temperature 300 °C. 5-Flowing water cooled refrigerant column. 6-Mercury thermometer (300 °C full-scale). 7-Inert gas outlet valve.*

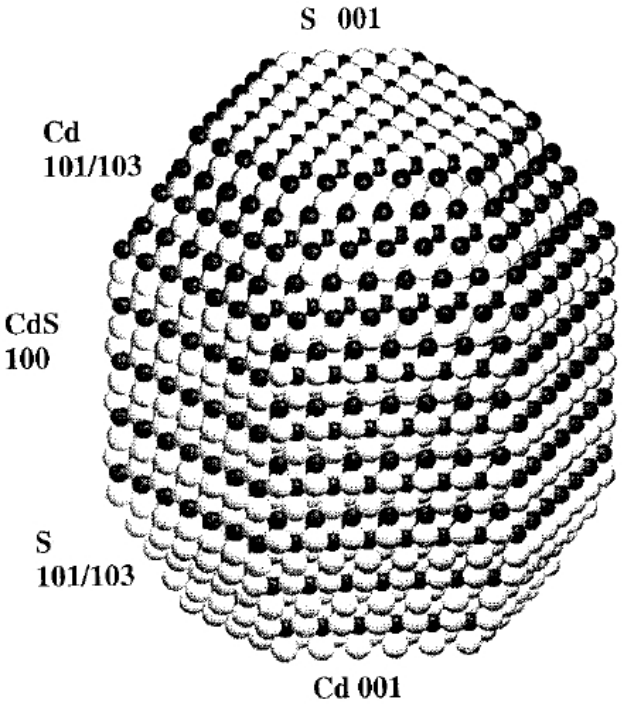

Figure 3.5: *Model of surface stoichiometry in a CdS nanocrystal elaborated from [99]. The cadmium atoms are represented by black spheres, while sulfur atoms by white spheres.*

of TOPO can be expressed as follows

$$\mathrm{mol(TOPO)} = 0.55\,\frac{4\pi R^2}{2aN_A} \tag{3.25}$$

where R is the nanocrystal radius, a is the elemental cell area of wurtzite CdS, N_A is the Avogadro number, and 0.55 is the TOPO coverage factor obtained experimentally in [100]. The moles number of cadmium precursor (CdO) can be obtained by

$$\mathrm{mol(CdO)} = \rho_{\mathrm{CdS}}\frac{4}{3}\frac{\pi R^3}{MW_{\mathrm{CdS}}N_A} \tag{3.26}$$

where ρ_{CdS} is the density of bulk CdS and MW_{CdS} its molecular weight. Dividing equation 3.26 by equation 3.25 and rearranging, one obtains the following expression of the nanocrystals final radius

$$r = \frac{3}{2}\frac{0.55\,MW_{\mathrm{CdS}}}{\rho_{CdS}a}\frac{\mathrm{mol(CdO)}}{\mathrm{mol(TOPO)}} \tag{3.27}$$

By this simple formula, it is thus possible to estimate the number of moles of surfactant, TOPO in the specific case, needed to have completely surface coated nanocrystal of the desired size r. It is necessary to remark that equation 3.27 has been formulated making very rough approximations. It has been assumed that only the 55% of the sites present on the nanocrystal surface (unsaturated Cd atoms) are occupied by a TOPO molecule, that the density of the material used in the formula ρ_{CdS} is the one of bulk CdS, but in reality, ρ_{CdS} is itself function of the nanoparticle radius and finally the elemental cell area a is different for the different crystallographic faces

of the nanocrystal. However, although the rough approximations, the equation 3.27 is still useful to have a molar ratio between Cd precursor and the surfactant (TOPO). Nevertheless, this is valid only at the stage when all the precursors have been consumed, i.e. at the end of the growth process. Yet, it is not useful at all for the early stages of the growth, when the nanocrystals size is more influenced by parameters such as the temperature and precursors concentrations. From the calculus it turns out that 10 mmol of TOPO are necessary to coat nanocrystals with a diameter of 3 nm. Nevertheless, experimentally a slightly higher concentration was used for safety. The TOPO concentration excess is however very small, since an excessively high concentration will inhibit the growth [74].
Once all the reactants are loaded in the reaction pot, the refrigerating column, the nitrogen inlet and the rubber septum are mounted on the flask and the inhomogeneous mixture is heated up to 300 °C under vigorous stirring and in an inert atmosphere of N_2. The mixture has initially an opaque reddish-orange coloration typical of CdO but after about one hour the cadmium oxide is completely dissolved resulting in a transparent solution.
After the phase of cadmium-precursor preparation, the temperature is adjusted to a determinate value suitable for the nanocrystal growth ($\sim$260 °C). The growths of CdS nanocrystals were carried out in order to get nanocrystals of different size and for this purpose two strategies were adopted. One strategy accounts the extraction by a syringe of several solution portions (4-5 ml) taken at consecutive times. In the other strategy, the reaction is brought to accomplishment and the size is supposed to be determined only by the surfactant concentration, hence more growth with different surfactant concentrations must be carried out. In this last case, Ostwald ripening can be also exploited to have a focusing of the size distribution. Experiments have shown however that this kind of growth is not always very reproducible. Even though in every synthesis the same materials are used, the environmental conditions may change from synthesis to synthesis (e.g. small differences of concentration, of temperature and presence of external pollutants) bringing to final products with stoichiometric and morphologic differences. This situation is not advisable for the kind of investigation that will be done on this material since Raman spectroscopy is very sensitive to stoichiometric variations and random errors will be introduced in the measurements. Therefore, to have a set of quantum dots samples grown from the same reaction is widely preferable, and for this reason, the multiextraction strategy was used.
Apart in a small beaker, a solution containing 2 mmol of elemental sulfur was prepared. The elemental sulfur S_8 99.999% metal basis obtained from Sigma-Aldrich has been solved in 1-octadecene. To have a complete dissolution, it is necessary to heat up the solution to $\sim$100 °C. Once all the sulfur is dissolved, the solution assumes a slightly yellow transparent color due to the S_8 molecule, but the solution must be kept at high temperature to avoid the sulfur recrystallizes. In solution one has molecular S_8 and H_2S formed from the reaction between S_8 and the hydrocarbon (1-ODE) and this last compound constitute the source of sulfur. 1 ml plus a small excess of the as prepared solution is sucked by a pyrex glass syringe and swiftly injected throughout the rubber septum into the reaction pot. The solution immediately assumes a light yellow coloration which quickly turns to darker yellows. Always through the rubber septum, by another pyrex glass syringe, several aliquots of the solution (at most 5-6 of $\sim$4 ml) are extracted at different times during the growth and stored in glass test tubes where they quickly cool down. The rest of the solution is left inside the reaction pot allowing the growth to continue.

3.3.5 Extraction and Purification of Nanocrystals

The as grown nanocrystals are dispersed in the organic solvent 1-octadecene which cannot be removed by a simple evaporation due to its high boiling point (250 °C). Moreover, the presence of impurities such as unreacted cadmium precursor (Cd-stearic acid complex), excess of surfactants (TOPO and stearic acid) needs to be removed in order to have a nanocrystal amount ready pure enough to be analyzed by optical techniques.
The purification processes will be applied either to the set of extracted solutions stored in the test tubes both to the solution coming from the flask. The first purification step consist in the filtration via percolation of the solution on order to remove the solid residuum. After that, the solution are washed, usually 3-4 times, by a 1:1 mixture of chloroform/methanol which allows to extract from it the unreacted cadmium stearate, stearic acid as well as the free TOPO. This solvents mixture is ideal because is immiscible with 1-octadecene but it still has the property to solve the organic and metal-organic compounds quoted above. The methanol alone can be used for this purification also but it does not solve as much well the cadmium stearate and the stearic acid. The second purification step consists in the precipitation of the nanocrystal gel. The precipitation is performed by acetone since it is completely miscible with 1-octadecene, while the TOPO coated CdS nanocrystal are completely insoluble in acetone. The precipitation and successively the washing with acetone are repeated several times until any trace of 1-ODE is removed. This can be proved easily dropping the washing acetone on a paper sheet. The acetone evaporates very fast and if an oily residuum is left, traces of 1-ODE are still present in the nanocrystals gel. Once the purification is accomplished, the TOPO-CdS nanocrystals are dried under vacuum to remove the residual acetone then solved in chloroform or toluene and stored in test tubes.

3.3.6 Coating Exchange

As already seen in the previous subsection, the TOPO-coated CdS even after the purification, have a gel-like consistence due to the hydrophobic coating shell. However, thanks to the weak bonds between the TOPO molecules and the quantum dots surface, they can be easily replaced by other molecules. In particular, molecules having in the structure an N atom with lone pair or a -SH group form more stable bonds with the atoms on the nanocrystal surface. According [101], the bonds between the TOPO molecules and the dangling bonds of nanocrystals surface are rather weak and the TOPO molecules can be easily displaced especially by -SH containing molecules which can form very strong bonds with the nanocrystal surface. Therefore, molecules such as thioalcohols, dithiols or thiocarboxylic acids bind strongly on the nanocrystal surface by their -SH group and at the same time expose outward their polar hydrophilic groups making the nanocrystals soluble in water. Furthermore, the replacement of TOPO coating will change also the consistence of the nanocrystals from gel-like to powder-like. The first tentative to replace the TOPO coating layer has not been done using a thiol, rather exploiting a reaction with pyridine. The pyridine is a heterocyclic aromatic compound that thanks to the nitrogen atom lone pair has a weak coordinating action, yet stronger than TOPO. Following [1], a small aliquot of TOPO-CdS quantum dots was left to react at reflux for about 12 hours at $\sim$70 °C under vigorous stirring and dark condition. The quantum dots are precipitated from the resulting solution by hexane and successively treated again with pyridine. The procedure can be repeated several times until all the TOPO molecules have been replaced. Experimentally, this procedure was repeated three times, but even after the third treatment, the resulting material presented a wax-like consistence.

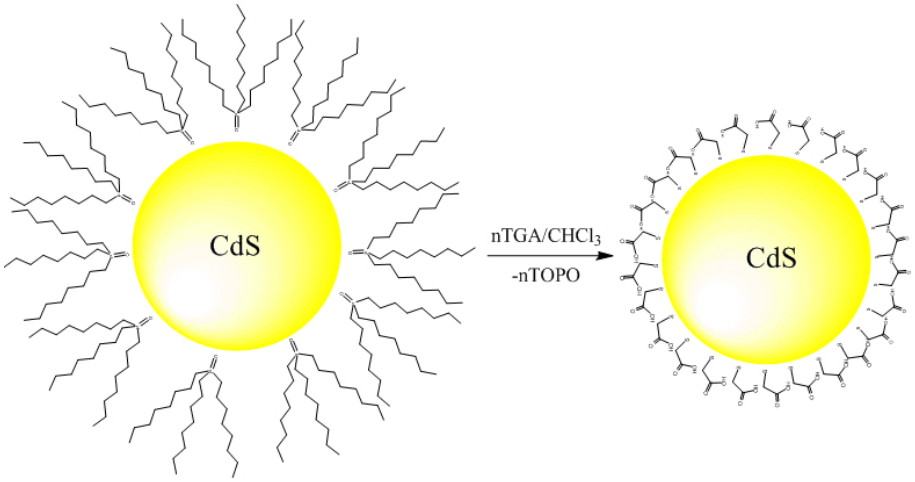

Figure 3.6: *Image depicting the replacement from CdS nanocrystal surface of the trioctylphosphine oxide coating layer by thioglicolic acid.*

A possible explanation is that the pyridine replaced the TOPO but not the stearic acid, which is probably more tightly bonded to the quantum dots surface. This method was thus forsaken in favor of a thiol based reaction. By the knowledge acquired from the literature [101–104], a procedure to obtain powder-like CdS nanocrystals was developed. The methods consists in the replacement of TOPO with thioglycolic acid (TGA) also known as mercaptoacetic acid. The experimental procedure provides to solve a nanocrystals aliquot in chloroform and then to add a moderate excess of thioglycolic acid. An immediate turbidity is observed, this means that the TGA has replaced the TOPO. After some hours of reaction there is a separation of the two phases, liquid and precipitate, and the TGA coated nanocrystals can be thus recovered as a yellow powder at the bottom of the test tube. The supernatant, containing chloroform, TOPO and TGA in excess is wasted. Successively, it is necessary to wash the powder several times by chloroform to remove the excess of TGA, in general 4-5 rinses are sufficient. However, even though this procedure replaces almost completely TOPO with TGA and produces powder-like CdS nanocrystals, to have a complete substitution of the TOPO coating layer, a second exchange must be performed. This is done solving the CdS quantum dots powder in a pH adjusted water solution and adding again TGA, see [101, 102] for details. This second exchange however was not done since not necessary for the aim of this thesis. The as produced CdS-TGA nanocrystals are stored under an organic solvent, e.g. chloroform, and placed in a dark environment to avoid the damage produced by photo-oxidation [105, 106].

3.4 Chemical Compounds

In this section are shown the molecular structures of the organic compounds used for the growth of cadmium sulfide nanocrystals. The molecules in the figures 3.7, 3.8, 3.9, 3.11 and 3.12 are drawn in the simplified IUPAC representation where the hydrogen atoms of the hydrocarbon chain are omitted, the carbon atoms are the apexes of the chains, and the C−C bonds are represented by simple lines.

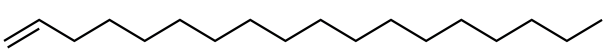

Figure 3.7: *1-octadecene (1-ODE), Alfa Aesar 90% Technical grade.*

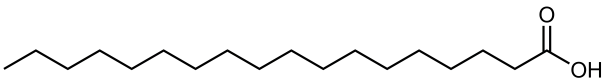

Figure 3.8: *Stearic acid or octadecanoic acid. Alfa Aesar 90% Technical grade*

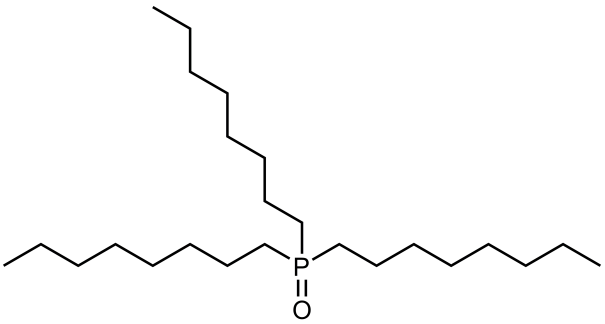

Figure 3.9: *Trioctylphosphine oxide (TOPO), Sigma-Aldrich 90% Technical grade.*

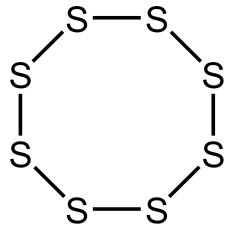

Figure 3.10: *Elemental sulfur S_8, Sigma-Aldrich 99.999% metal basis.*

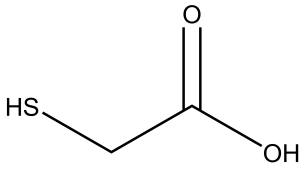

Figure 3.11: *Thioglycolic acid (TGA) or mercaptoethanoic acid, Fluka 98%*

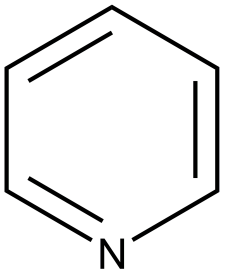

Figure 3.12: *Pyridine, Fluka 98%.*

Chapter 4

Optical Techniques

In semiconductor science, the optical techniques are the most widely used to investigate semiconductors physical properties. It is possible to obtain informations concerning the electronic states, the dielectric function and about vibrational properties of semiconductor crystals. Moreover, they have the advantage on the other techniques (e.g. electronic techniques) to be non destructive and they do not strictly require particular experimental condition like UHV.

4.1 Principles of Raman Scattering

The inelastic scattering produced by the interaction between light and matter was firstly recognized by C.V. Raman [107, 108]. In this process, even when a molecule does not have a proper dipole moment, the light can still interact with it and carries information regarding the vibrational or rotational states. The interaction is viewed as a modulation of the electric field of the outgoing radiation by the time-varying polarizability $\alpha(t)$

$$\alpha E(t) = \left(\alpha_0 + \alpha e^{i\omega_{vib}t}\right) E(t) \tag{4.1}$$

Analogously to molecules, in crystalline solids, the inelastic light scattering is produced by a time-dependent charge fluctuation (modulation of polarizability) which interacts with e.m. radiation exchanging energy. The scattering process can be elastic or inelastic and the two cases are recognized as Rayleigh and Raman scattering respectively. In the first case one has $\hbar\omega_i = \hbar\omega_s$, i.e. the scattered photon will have the same energy of the incident photon. In the inelastic process there is instead an exchange of energy between the incident photon and the matter. The scattered photon will have an energy $\hbar\omega_s$ higher or lower than the incident photon energy. The entire process is described by the following equation

$$\hbar\omega_s = \hbar\omega_i \pm \hbar\omega_L \tag{4.2}$$

where ω_i, ω_s and are the frequency of the incident and scattered radiation while ω_L is the frequency of the phonon. When in equation 4.2 the minus sign appears, one has the so called Stokes process where photon transfers energy to the matter. Conversely, when in equation 4.2 the plus sign appears, one has the Anti-Stokes process where matter transfers energy to the photon. The Stokes and Anti-stokes processes are visible in Raman spectra as lines at the left and right side of the Rayleigh elastic line.

4.1.1 Raman Scattering in Solids

When light passes through a medium it can be transmitted or adsorbed following the standard laws of refraction and diffraction in order that the $\vec{k}$-conservation rule is respected. The small quantity of light which is scattered by phonons can be considered also to respect the $\vec{k}$ conservation rule. This is because the phonons responsible of the scattering are the ones with a linear momentum $\vec{q}$ very close to Γ point of the first Brillouin zone, i.e. the ones with $q \approx 0$. The stokes and anti-stokes processes, in solids can be better viewed in term of linear moments $\vec{k}$ and $\vec{q}$. As it is known from the classical theory, an oscillating dipole $\vec{p}$, which oscillates at a frequency ω produces an electromagnetic radiation of the same frequency. The power emitted dP in a solid angle $d\Omega$ is

$$dP = \frac{< \ddot{\vec{p}}^2 > \sin^2 \phi}{4\pi c^3} d\Omega \tag{4.3}$$

This formula is valid only when the dimensions of the solid angle is smaller than the wavelength of the emitted radiation.
According to classical theory, the dipole moments are induced by an incident electromagnetic radiation having a time varying electric field $\vec{E}_i(t)$

$$\vec{p}(t) = \vec{P}(t) \cdot V = \chi \cdot V \cdot \vec{E}_i(t) = \chi \cdot V \cdot \vec{E}_i^0 e^{i(\vec{k}_i \vec{r} - \omega_i t)} \tag{4.4}$$

χ and V are the electric susceptibility and the volume of the medium. If χ is time and space independent, the emitted radiation has the same frequency of the incident one and the emitted radiation will be in the parallel direction with the incident radiation. Nevertheless, χ of any medium is never time independent due to spatial and temporal fluctuations of the electronic charge. The fluctuation of χ may arises from the presence of defect, impurities and the naturally occurring thermal excitations electronic and vibrational. The most relevant charge fluctuations are however the one induced by atomic vibrations. Atomic vibrations in solids are viewed as phonons, they are described classically as a waves propagating in the lattice in terms of normal coordinates Q_j, with j is the index of the j^{th} phonon mode, see section 2.3.
The atomic displacement caused by phonons perturbs the electronic density, and due to the periodic nature of the oscillation, a modulation of the electrical susceptibility χ results

$$\chi = \chi_0 + \chi(Q_j) e^{i(\vec{k}_j \cdot \vec{r} - \omega_j t)} \tag{4.5}$$

where χ_0 is the static susceptibility, that is without phonons modulation, $\chi(Q_i)$ is the susceptibility modulated by phonons, $\vec{k}_j$ is the wavevector of the j-th phonon mode, while ω_j is the frequency of the j-th mode. By the combination of equation 4.4 and 4.5 one gets the expression of the phonon-modulated dipole moment

$$\vec{p} = \chi V \vec{E}_i^0 e^{i(\vec{k}_i \vec{r} - \omega_i t)} + \chi(Q_j) V \vec{E}_i^0 e^{i[(\vec{k}_i \pm \vec{k}_j) \cdot \vec{r} - (\omega_i \pm \omega_j) t]} \tag{4.6}$$

where $\vec{k}_i$ and ω_i are the wavevector and frequency of the incident photon respectively. Equation 4.6 describe thus classically the light scattering process by the matter. In the second member of equation 4.6, the first term represent the elastic scattering (Raleigh scattering) while the second describes the anelastic scattering and it can be identified as $\vec{p}_s$. The argument of the exponential $(\omega_i \pm \omega_j)$ is the frequency of the scattered light ω_s. It divides in Stokes anti-Stokes energy levels, according to whether the minus or plus sign appears respectively. In common experiments, usually only Stokes scattered radiation is taken into account because of its higher intensity. This

is due to the Bose-Einstein factors, $n+1$ in Stokes and n in anti-Stokes appearing in the expression of scattering cross section $d\sigma/d\Omega$ [30, 42].
Equation 4.6 describes rigorously the scattering process in term of dielectric susceptibility modulation. However, it does not result particularly useful in the phenomenological treatment of light scattering. Making use of the adiabatic or (quasi-static) approximation, in which the lattice is considered to be static in comparison with the oscillation of electronic density, the same susceptibility can be expanded in Taylor series as follows [30]

$$\chi(Q_j, \nabla Q_j, E_a) = \chi^0(\omega_i, \omega_s) + \chi^1(\omega_i, \omega_s) + \chi^2(\omega_i, \omega_s) + \dots \tag{4.7}$$

where the first term $\chi^0(\omega_i)$ is the susceptibility unaffected by any phonon transition, $\chi_1(\omega_i, \omega_s)$ is the first order transition susceptibility involving one phonon, it generates $\omega_i \pm \omega_j$ frequencies. $\chi_2(\omega_i, \omega_s)$ that is the second order transition susceptibility involves a two phonons transition and generates $\omega_i \pm (\omega_j \pm \omega_j)$ frequencies. Normally, in Raman experiments only one phonon processes are detected, other higher order effects involving $\vec{k}$, the electric field or two phonons are usually weak as intensity, but they might become relevant in resonance condition and for some polar materials like CdS.
Considering only the first order Taylor series expansion of $\chi(Q_j)$, and replacing the normal coordinates Q_j with the atomic displacement ξ_l, one can get a very important expression of scattered light intensity

$$I_s \propto |\vec{e}_i \cdot \sum_l (\frac{\partial \chi}{\partial \vec{\xi}_l}) \vec{\xi}_l(\omega_0) \cdot \vec{e}_s|^2 \tag{4.8}$$

with $\vec{e_i}$ and $\vec{e_s}$ unitary vector of the incident and scattered electric field. The quantity $\sum_l (\frac{\partial \chi}{\partial \vec{\xi}_l}) \vec{\xi}_l(\omega_0)$ is a second rank tensor and it is usually recognized as Raman tensor $\Re$. Equation 4.8 can be rearranged in a more readable form

$$I_s \propto |\vec{e}_i \cdot \Re \cdot \vec{e}_s|^2 \tag{4.9}$$

In first approximation $\Re$ is defined as a symmetric tensor even if it represents an anelastic scattering process. This is valid because of the small difference between the frequencies of the incoming and the scattered light. Eventually, asymmetries in $\Re$ will be caused only by the presence of an intrinsic magnetic field in the crystal. By equation 4.9, it is possible to determine the selection rules of Raman scattering of a crystal having the polarization of incident and scattered radiation described by the unitary vectors $\vec{e_i}$ and $\vec{e_s}$ and the Raman tensors relative to each vibration of a determinate symmetry mode which can be determined making use of the group theory.

4.2 Quantum Mechanic Microscopic Theory

So far, the description of scattering process has been only of classical character, but to analyze the microscopic aspect of Raman spectroscopy, a quantum mechanic approach becomes necessary.
First of all it is necessary to state that the electromagnetic radiation having high frequency (UV, visible radiation) can not interact directly with phonons because of the large difference in frequency. Therefore the e.m. radiation will interact only with the electronic states causing a virtual transition. The excited electronic state will decay back in its ground state exchanging

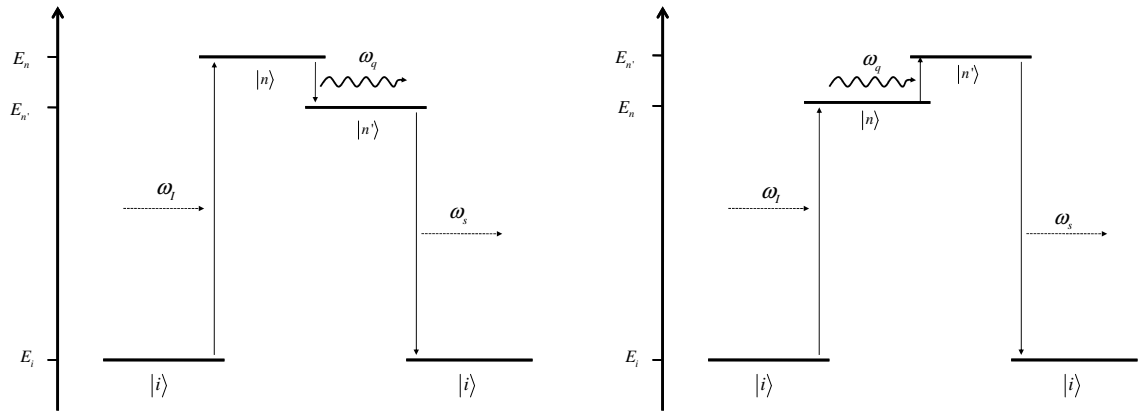

Figure 4.1: *Diagrams of energy levels involved in Raman scattering respectively for Stokes (left) and Anti-Stokes processes (right).*

energy with phonons.
The scattering process can be described by the absorption of a photon of frequency ω_I which brings the initial electronic state $|i\rangle$ to an excited state $|n\rangle$. This state is then scattered to a secondary state $|n'\rangle$ by the emission or absorption of a phonon with frequency $\omega_{\vec{q}}$. The $|n'\rangle$ state will then decay to the former initial state emitting a photon having an energy ω_S which can be > or < than the incident radiation ω_I. The first case where $\omega_I > \omega_S$ is known as Stokes scattering and a phonon is created in the material, while the second where $\omega_I < \omega_S$ is known as anti-Stokes scattering where a phonon is annihilated in the crystal. The two processes are schematized in the following diagram 4.1 The Raman scattering is for definition weak in intensity (scattered power), therefore it is necessary to calculate the scattering probability using a third order perturbation theory. According to [30, 42], the scattering probability of a system going from the initial state $\langle i|$ to the final state $|f\rangle$ can be calculated using Fermi's golden rule. For one phonon scattering six time ordered processes are possible, they are described by as many Feynmann's diagrams and quantum mechanical terms appearing in the scattering probability equation. Approximating the process only with the first Feynmann's term there will be three equations describing the vertexes in the diagram. The first vertex will express the excitation by the incident radiation of the electronic state from $\langle i|$ to $|f\rangle$

$$\sum_{n,n'} \frac{\langle n|H_{eR}(\omega_L)|i\rangle}{[\hbar\omega_L - (E_n - E_i)]} \tag{4.10}$$

where ω_I is the exciting photon frequency and $H_{eR}(\omega_I)$ is the Hamiltonian which describes the interaction between e.m. radiation and the ground electronic state. The second vertex describes the creation or annihilation of a phonon and the decay of the electronic excited state to the intermediate state $|n'\rangle$ as result of the interaction with the phonon

$$\sum_{n,n'} \frac{\langle n'|H_{e-ion}(\omega_0)|n\rangle\langle n|H_{eR}(\omega_i)|i\rangle}{[\hbar\omega_i - (E_n - E_i)][\hbar\omega_i - \hbar\omega_0 - (E_{n'} - E_i)]} \tag{4.11}$$

where H_{e-ion} is the Hamiltonian which describes the interaction between the electron and the phonon. Finally, considering energy conservation in Raman scattering process and applying

Fermi's golden rule, we obtains the following equation for the scattering power

$$P(\omega_S) = \left(\frac{2\pi}{\hbar}\right) \left| \sum_{n,n'} \frac{\langle i|H_{eR}(\omega_S)|n'\rangle\langle n'|H_{e-ion}(\omega_{\vec{q}})|n\rangle\langle n|H_{eR}(\omega_L)|i\rangle}{[\hbar\omega_L - (E_n - E_i)][\hbar\omega_L - \hbar\omega_{\vec{q}} - (E_{n'} - E_i)]} \right|^2 \delta(\hbar\omega_L - \hbar\omega_{\vec{q}} - \hbar\omega_S) \tag{4.12}$$

Here the final energy denominator is converted to a Dirac-delta function to express the conservation of energy an to have the final state $|f\rangle$ the same as initial $\langle i|$.

4.2.1 Resonant Raman Scattering

In Raman scattering, when excitation energy is lower than the band gap of the semiconducting material under investigation, there will be only virtual electronic transition which transfers the excitation to phonons. In the case of bulk cadmium sulfide E_g=2.5 eV), only an exciting radiation wavelength below 495 nm will have an energy above the band gap. When this happens, a resonance regime is established and an enhancement of Raman scattering intensity results. According to microscopic theory, the scattering enhancement occurs when in equation 4.12 one of the two denominator terms becomes very small. For a determinate electronic state n, when $\hbar\omega_i$ is very close to $E_n - E_i$, this intermediate state will dominate in the scattering contribution, therefore 4.12 can be rearranged as follow.

$$P(\omega_S) \approx \left| \frac{\langle 0|H_{eR}(\omega_S)|a\rangle\langle a|H_{e-ion}(\omega_q)|a\rangle\langle a|H_{eR}(\omega_L)|0\rangle}{[E_a - \hbar\omega_L] - [E_a - \hbar\omega_S]} + C \right|^2 \tag{4.13}$$

where the initial and final state are labeled as $|0\rangle$ and $|a\rangle$, E_a is the resonant intermediate state and C is the non-resonant term which adds the contribute from non-resonant states; this term is however much smaller than the resonant one. The Dirac-delta of the equation 4.12 can be drop since the summation over all ω_S has been performed. Two cases of resonance can be distinguished, $E_a = \hbar\omega_L$ and $E_a = \hbar\omega_S$. The first is referred as incoming resonance due to energy of the incoming radiation, while the second as outgoing resonance and it is due to the energy of outgoing radiation. When resonance occurs, one of the two terms at the denominator goes to zero therefore 4.13 should diverge, nevertheless, the electronic intermediate state $|a\rangle$ has a finite lifetime due to non-radiative scattering processes (e.g. defects and impurity scattering) and this will give rise at the denominator a damping term γ which will prevent it to diverge. The resonance enhancement is observed also for multi-LO-phonons, in particular, for II-VI semiconductors is particularly strong. The explanation, proposed in [109] consists in a cascade mechanism.

4.2.2 Multiple Phonons Processes

So far, we have dealt only with the first order Raman scattering processes, however, in many cases the higher order processes become also important. In first order scattering the total moment and energy conservation is very strict and phonons at $\vec{k} \approx 0$ are observable only. Conversely, in higher order processes such rule is not longer so strict and contributes coming from phonons in a wider interval around $\vec{k} \approx 0$ will become visible. Therefore any information regarding the phonons frequencies and the wavevector at Γ will be lost. Yet, the completely symmetric scattering tensors reflect the two-phonons density of states [30]. In Raman spectra

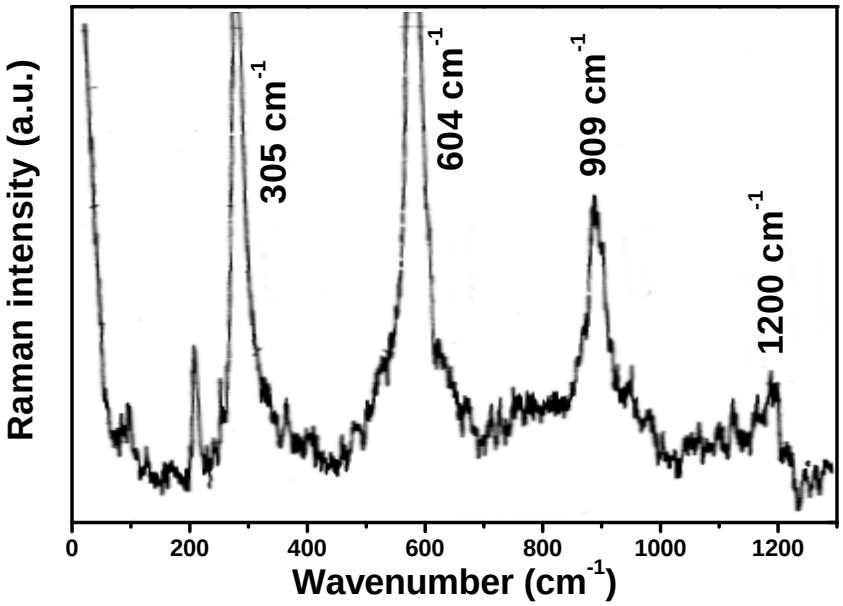

Figure 4.2: *Raman spectrum of bulk CdS elaborated from [111]. The spectrum was acquired at 4 K using an exciting wavelength of 488 nm.*

of many zinc-blende and wurtzite semiconductors, multiple phonons processes are visible, in particular for two-phonons process the selection rules become

$$\hbar\omega_s = \hbar\omega_i \pm \hbar(\omega_j + \omega_j) \tag{4.14}$$

where ω_j is the frequency of the j-th phonon. The multi-phonon process seems to be particularly important in II-VI semiconductor, where the overtone lines have high intensity also at high order number n, sometimes even more intense than the first order. This behavior can be explained by the strong coupling between phonons and polarons existing in such materials. According to [110], the Raman scattering cross section $d\Omega^n/d\sigma$ of bulk CdS, which is proportional to intensity goes as

$$\frac{d\Omega^n}{d\sigma} \sim \begin{cases} C^{2n} & n = 1, 2 \\ C^6 \left|\log C\right| & n = 3 \\ C^6 & n \geq 4 \end{cases} \tag{4.15}$$

where n is the order of the mode and C is the phonon-polaron coupling constant that in CdS assumes a value of 0.7 [110]. Experimental observations [111] show that the ratio between the first and second order longitudinal phonon lines goes like

$$\frac{I_{\omega_0}}{I_{2\omega_0}} \sim \left(1 + \frac{\omega_0}{\Delta\omega}\right)^2 \tag{4.16}$$

where I_{ω_0} and $I_{2\omega_0}$ are the intensities respectively of the first and second order, ω_0 is the phonon frequency and $\Delta\omega$ is the difference between the exciting frequency and the first order peak. This strong phonon-polaron coupling in CdS arises from its highly polar nature in respect with the other III-V and II-VI semiconductors. It can be interpreted in a more physical way observing how those multi-phonons peaks strictly follow the luminescence broad peak and that their intensity increases at the approaching of exciting laser line to energy of the luminescence peak.

This can be explained with the fact that equilibrium positions of the atoms are different for different electronic states (excited states), i.e. a sort of Frank-Condon principle applied to solids [112].
In figure 4.2 is shown a Raman spectrum of bulk cadmium sulfide elaborated from [111]. The Raman spectra of hexagonal CdS are characterized by the large predominance of LO modes and by the strong intensity of higher order LO modes $n \geqslant 2$. The intensity of higher order LO modes results to be enhanced in the spectral region of photoluminescence emission bands thanks to a mechanisms of exciton-phonon and polariton-phonon couplings [30, 112]. It can be seen how the fourth order LO mode is still visible, and the 2LO mode has an intensity even higher than the LO. The ratio between the intensities of the different modes is described by equation 4.15 [111]. A similar behavior involving multiphonons process is observed also in Raman spectra of CdS quantum dots.

4.3 Absorption Spectroscopy Principles

The absorption spectroscopy is perhaps the most important technique to characterize the electronic properties of semiconductor quantum dots. Since the quantum dots produced by colloidal methods can be always in solution, organic or aqueous. The absorption measurements are performed almost exclusively on solutions.
The absorption of a solution, or more in general of a dielectric media is ruled by the Lambert-Beer law

$$A = -\log\left(\frac{I}{I_0}\right), \quad A = \epsilon(\hbar\omega)\ell c = \alpha(\hbar\omega)\ell \tag{4.17}$$

where A is the absorbance and I and I_0 are the outgoing and incoming light intensities respectively. A more useful expression of the absorbance is put it into relationship with the concentration c, the light path through the cell ℓ and of course with the material properties by the molar extinction coefficient ϵ. The extinction coefficient $\alpha(\hbar\omega)$ can be derived quantum mechanically for one single quantum dot of radius R as follows [113]

$$\alpha(\hbar\omega) = A\sum_j \delta(\hbar\omega - E^j_{1,0}) \tag{4.18}$$

where A is a constant proportional to the square of the matrix element of the dipole moment between conduction and valence wavefunctions. It has been summed over all the possible electronic transitions $E^j_{1,0}$ with $n = 1$ and $l = 0$ see subsection 4.3. This relation is valid at very low temperature (close to 0 K) where the absorption peaks are very narrow, but it does not hold anymore at higher temperatures where the shortening of states lifetime produces a lorentzian broadening. The equation 4.18 thus becomes

$$\alpha(\hbar\omega) = \frac{A}{\pi\sqrt{2\pi}}\sum_j \frac{\Gamma}{\left[(\hbar\omega - E^j_{1,0})^2 + \Gamma^2\right]} \tag{4.19}$$

where Γ is the damping coefficient of the electronic transition. The equation 4.19 is valid again only one single nanocrystal. Nevertheless, for an ensemble of quantum dots one must account the size distribution centered at the mean radius $\bar{R}$. Therefore the extinction coefficient will be given by the convolution between $\alpha(\hbar\omega)$ and the size distribution function $P(R)$ (typically a

Gaussian or an asymmetric Gaussian)

$$\bar{\alpha}(\hbar\omega) = \frac{1}{\bar{R}^3}\int_0^{+\infty} R^3\alpha(\hbar\omega)P(R)dR \tag{4.20}$$

where $\bar{R}$ is the average radius of the nanocrystals. The $I(\hbar\omega) = \bar{\alpha}(\hbar\omega)\ell$ is expected to have a voigt lineshape, nonetheless, one can state that the spectrum is much less sensitive to the Γ parameter than to the size distribution σ, as it arises also from experimental results 5.2.1. Typically, for a given value of σ, no significant difference can be observed for, say, $7\,meV < \Gamma < 13\,meV$ [113]. From a point of view closer to the experiments, the absorption coefficient is in relationship with the light intensity as follows [43]

$$\alpha(I) = \frac{\alpha_0}{1 + I/I_{sat}} \tag{4.21}$$

where the saturation intensity is $I_{sat} = \hbar\omega N(\alpha_0\tau)^{-1}$ with τ the electronic state lifetime, α_0 the maximum value of the absorption coefficient and N the number of nanoparticles. Introducing the dependency from the resonance frequency ω_0, equation 4.21 becomes, in the case of inhomogeneously broadened lineshape

$$\alpha(\omega, I) = \alpha_0(\omega)\left[1 - \left(1 - \frac{1}{\sqrt{1 + I/I_{sat}}}\right)\frac{\Gamma^2(I)}{(\omega - \omega_0)^2 + \Gamma^2(I)}\right] \tag{4.22}$$

Where the linewidth $\Gamma(I)$ is intensity-dependent as $\Gamma(I) = \Gamma_0(1 + \sqrt{1 + 1 + I/I_{sat}})$. In the limit case $I/I_{sat} \ll 1$, i.e. when high incoming light power is used, equation 4.23 assumes the more simple form

$$\alpha(\omega, I) = \alpha_0(\omega)\frac{4\Gamma_0^2}{(\omega - \omega_0)^2 + 4\Gamma_0^2} \tag{4.23}$$

In basis to the consideration done, the absorption band lineshape will be a gaussian distribution of lorentzian subbands.

4.4 Experimental Apparatus

In this chapter are described the instruments and the experimental setups utilized to perform the absorbance, photoluminescence and mainly Raman measurements on cadmium sulfide nanocrystals. The absorption measurements were carried out using commercial type instruments, while photoluminescence and Raman scattering measurements were performed by two distinct home-build optical setups.

4.4.1 Absorbance spectrometer

The absorbance measurements were performed with a Perkin-Elmer Lambda EZ201 spectrometer equipped with two light sources, a tungsten lamp for the IR-visible range and a deuterium lamp for the UV range. The bay has been modified in order to allocate both cuvettes either thin glasses. It is possible to perform absorbance measurements on solutions and thin film. With this spectrometer, scans from the near-IR (1000 nm) to the near-UV (200 nm) are possible. With the slowest scanning speed, the uncertainty in the wavelength position is of 0.1 nm. The resolution of the instrument in the visible range is of $\sim$2 nm ($\sim$ 10 meV).

4.4.2 Photoluminescence Spectrofluorimeter

The photoluminescence measurements were performed by an assembled optical setup. It is made up by a 75 W xenon lamp equipped by an output power attenuator. The white light provided by the lamp is monochromatized by a first monochromator. By this monochromator is possible to have monochromatic light for excitation in the near IR, visible and UV ranges (0-1400 nm). The monochromatized light is focused on the sample through a system of lenses and mirrors. The sample (solution) is loaded into a UV grade quartz cuvette. The emitted radiation is collected at 90 degrees in respect with the exciting radiation and is focused by a system of lenses into a second monochromator. This monochromating unit has a resolution (band pass) of 0.1 nm @ 435.8 nm (1 meV @ 2.84 eV) using a slit of 10 μm. The light detection unit constituted by a photomultiplier working in the wavelength range of 190-900 nm. To enhance the signal, the acquisition is done by a signal recovery procedure. The incoming light is modulated by a chopper and the signal acquired by a lock-in locked on the frequency of the chopper. The digitized data are then acquired by a computer.

4.4.3 Raman Spectroscopy Setup

The instrumentation required for Raman spectroscopy measurements, in particular the monochromator unit is far more complicated and sophisticated than the ones used for absorbance and fluorescence. The main reason is that the in comparison with the other two techniques, in Raman spectroscopy a particularly high spectral resolution is required. The spatial resolution is also very important especially in the study of nanostructured materials. A high spatial resolution allows to select a very small area of the sample from where the signal is collected, therefore, to get the information only from the area of interest or at least to reduce it as much as possible. In this way, the signal contribution from other not interesting areas of the sample will be drastically reduced. Unfortunately, the spatial resolution is limited by the well known diffraction limit which does not allow to push it below $\sim$500 nm.
By this Raman setup it is possible to work with three different spatial resolutions corresponding to three different instrumental configurations. The *macro*-Raman configuration is used to collect the scattered radiation from homogeneous samples with large area where a not particularly high spatial resolution is required, e.g. samples in UHV chamber or liquids and solution in glass cuvette. With this configuration, the spatial resolution can be in the best cases of some microns. With the *micro*-Raman configuration, the spatial resolution can pushed down to $\sim 500\,nm$ in the x and y directions. This high resolution is used essentially for spectroscopy of solids bulk and nanostructured semiconductors. This optical setup is also equipped with a *nano*-Raman facility. In this configuration, a nanometer resolution is available, however, it is not yet fully operative and it was not used for the measurements on CdS quantum dots and it will not be described here. In this study, only *micro*-Raman configuration was used, thus will be described more in detail in respect with the other two. However, it is worthwhile to remark the three optical configurations differ between them only in the light focusing and light collection optics. The optical setup consist of a visible and UV light Laser source, a Coherent Innova 200 Ar^+ laser which can provide a wide spectral range from the visible to the near UV (from 514 nm to 350 nm). Light power of > 2 W in the visible and of $\sim$1 W in the UV are available. Along the light path, from the laser output to the entrance slit of the monochromator, the laser beam can be opportunely polarized with a Fresnel prism, and reduced in power when necessary, by a set reflective or absorptive filters. Moreover, the Ar plasma lines produced in the laser tube can be

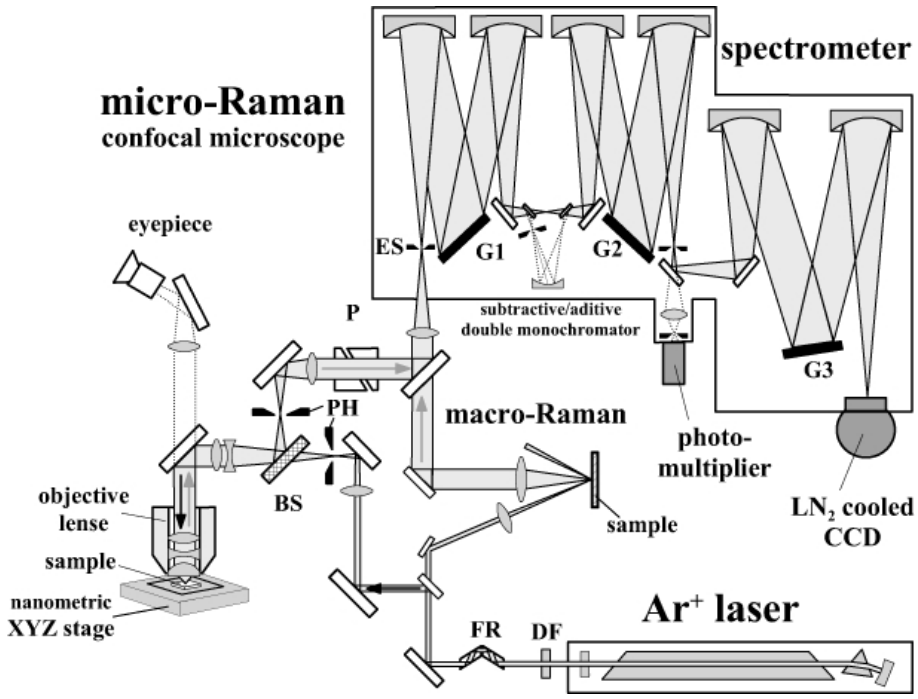

Figure 4.3: *Scheme of experimental Raman setup. In this picture only the macro- and micro-Raman configurations are reported. The monochromator and the laser source are common to the three configurations.*

filtered by interferometric filters specific for each wavelength. However, the plasma lines filter can be easily removed the plasma lines are needed for spectra calibration procedure. The laser light is focused on the sample by a microscope objective which at the same time collects the scattered light. The scattered light is focused on the monochromator entrance slit by a set of parabolic mirror. In order to have a high confocality of the optics, in between of the first two parabolic mirrors, just in their foci is placed a 10 μm pinhole holden by a three stage micrometric positioner. The elevate confocality allows to select the signal only from small portion of the three dimensional focus on the sample to jettison the unwanted radiation, e.g. signals from the lens coating. With a pinhole of 10 μm it is possible to reach a spatial resolution of $\sim$250 nm along the $x - y$ axis and $\sim$500 nm along the z axis. For the sample positioning, the setup is equipped with a x,y,z micrometric screws positioner. However, one last upgrade has equipped it with a two closed-loop piezoelectric stages (x,y) and an open-loop piezo lens mounting (z focus positioning) capable of 2 nm and 0.1 μm translational resolution respectively. Both piezo positioners are driven by an RHK SPM electronics. Thanks to this last upgrade it is possible to perform confocal spectroscopy i.e. to acquire point by point the signal from the sample surface obtaining a mapping of the intensity. To get the intensity mapping, different kind of light signal can be acquired, e.g. scattered laser light, a chosen Raman line or the PL signal. The signal is detected by a photomultiplier or a photodiode and then acquired by the SPM electronic which merges it with the sample position information. The spatial resolution may variate from case to case.

The core of the setup is represented by the Dilor triple grating monochromator which can operate in additive or subtractive mode. This monochromator has a spectral resolution determined experimentally of 2 cm^{-1} in the subtractive mode and 1 cm^{-1} in addictive mode. For the light detection, the monochromator is equipped with a liquid nitrogen cooled CCD Horiba Jobin-

Figure 4.4: *Picture of Raman setup.*

Yvon CD3000v placed after the spectrometer output slit and of a Peltier-effect cooled Hamamatsu photomultiplier placed after the two monochromator grating slits.
The entire optical system is placed on a vibration-damped optical table. The damping is performed in the low frequency range by the laminar flow pneumatic legs, while, in the high frequency range ($\nu > 100$Hz) by an auto-tune active damping technology. This damping is based on the interference between the vibrations of table surface and the oscillations produced of two piezoelectric crystals. This damping systems is of fundamental importance during confocal spectroscopy measurements where the eventual vibrations, when undamped, have amplitudes up to 100 μm. Consequently, they will strongly disturb the positioning performed by the x,y piezo-table which has a maximum scanning area of 16 μm, a value more than 5 times smaller than the amplitude of vibrations. However the vibrations does not come only from the environment but they can be produced also by the instrumentations present on the optical table. It was found that a very important source of vibrations was the Laser equipment, in particular its water cooling system. Due to the pulsed flow produced by the water pump a very strong vibrational noise with a frequency of ~ 50 Hz was transmitted on the table, and it could not be erased by the active damping. However, a series of intervents has allowed to drastically reduce this noise. They consisted in introducing four further pneumatic dampers below the aluminium board bearing the laser tube and rearranging entirely the hydraulic system of the laser cooling in order to quiet the water flow and damp the pressure of the pulses produced by the water pump.

Chapter 5

Experimental Results

The first part of the experimental work consisted in the colloidal growth of organic molecules coated-CdS nanocrystals as described in chapter 3. The CdS nanocrystals samples were grown with different sizes in order to observe the quantum confinement of electrons and phonons in dependence of the size. The optical methods used to study the confinement effect in this material are optical absorption and photoluminescence to study the electronic properties, while Raman spectroscopy were used to investigate the lattice dynamics. The first two are very common and widely used means to probe this kind of materials. In particular, from absorbance spectra a good estimation of the nanocrystals radii can be obtained. Concerning Raman spectroscopy, even though it is getting more and more important as a standard method to probe nanostructures, the interpretation of spectra of nanostructured semiconductors is not always very exhaustive and many details need still to be clarified.
The samples were also characterized by transmission electron microscopy (TEM) to verify the crystallinity, to determine the type of lattice, but mainly to have an estimation of the size and size distribution.

5.1 Samples Characterization

5.1.1 Optical Microscope Imaging

The microscope used is an Olympus model BH-2 equipped with an achromatic objective with a magnification power of 100. In this microscope the standard white light source was replaced by a high power blue LED (450 nm). This allow to increase the resolution thanks to the lower wavelength and higher monochromaticity. Moreover, by polarization techniques it was possible to improve the contrast. Practically, this was done polarizing the illuminating blue light and analyzing by another polarizer the light coming from the sample. The comparison between the vision by crossed and parallel polarizations will reveal important features of the sample. In particular, using crossed polarization it is possible to exclude the scattered light from the sample and to observe only the emitting areas (PL). This proved to be a very important tool to find the nanocrystals agglomerates. In fact, the photoluminescence of CdS nanocrystals is excited by the blue light, thus it can be observed with high contrast by the crossed polarization. The samples to study are prepared by drop casting a chloroform suspension of TGA-CdS nanocrystals powder on a microscope glass plate. Microscope imaging reveals the presence of areas with a different aspect. The entire plate is not uniformly covered by a thin organic layer, probably consisting of

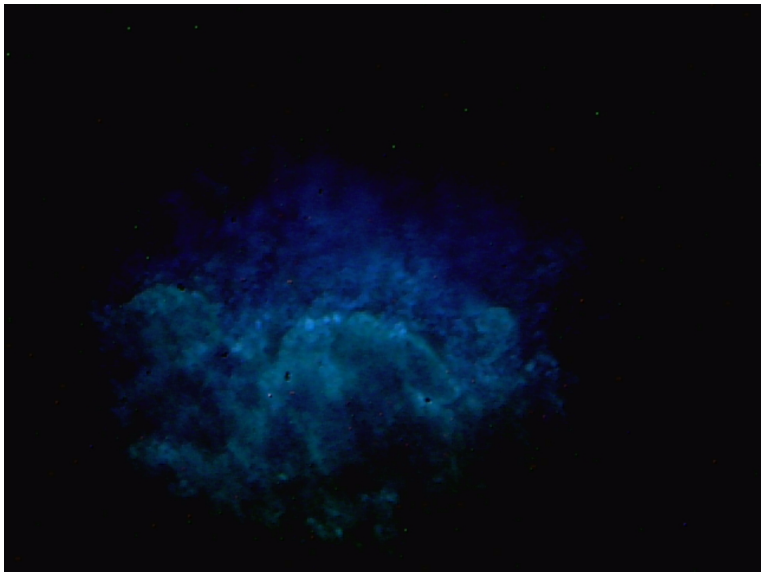

Figure 5.1: *Stone-like CdS nanocrystals agglomerates observed by crossed polarization.*

residual TOPO or excess of TGA. Nevertheless, some areas looks very dry, i.e. free from the organic layer. There, large stones of material constituted by CdS nanocrystals agglomerates are present Fig.5.1. The observation by crossed polarization reveals also a third kind of emitting areas where small amounts of material are present Fig.5.3. In these areas, the material appears layered on the glass surface and seems also to partially maintain the gel-like nature which the quantum dots had before the TOPO layer replacement. It is probable that in these areas a large fraction of the material is constituted by unreplaced TOPO-CdS nanocrystals. The microscope images of figures 5.2 and 5.1 are relative to the same are of the sample containing mostly stone-like CdS nanocrystal agglomerates. While, the figures 5.4, 5.3 are relative to a different area of the sample containing mostly gel-like CdS nanocrystals and residual unremoved TOPO and stearic acid.

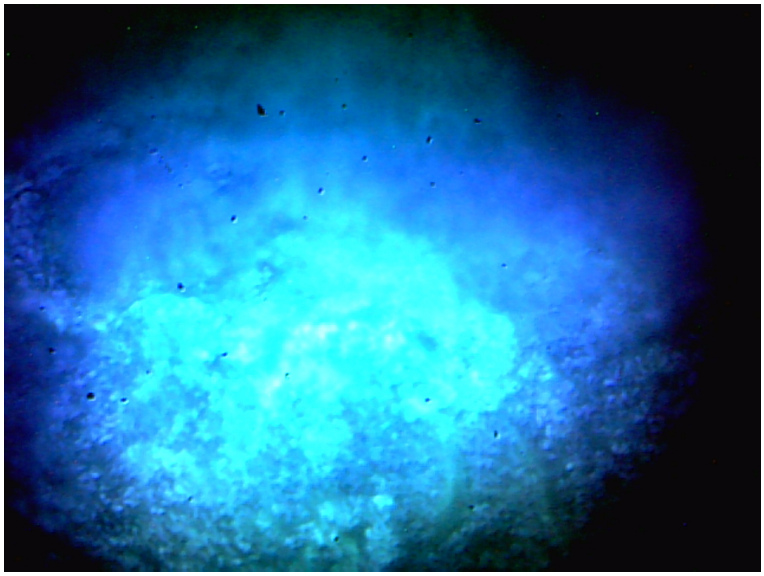

Figure 5.2: *Stone-like CdS nanocrystals agglomerates observed by parallel polarization. The contrast is much lower with respect to the observation with crossed polarization.*

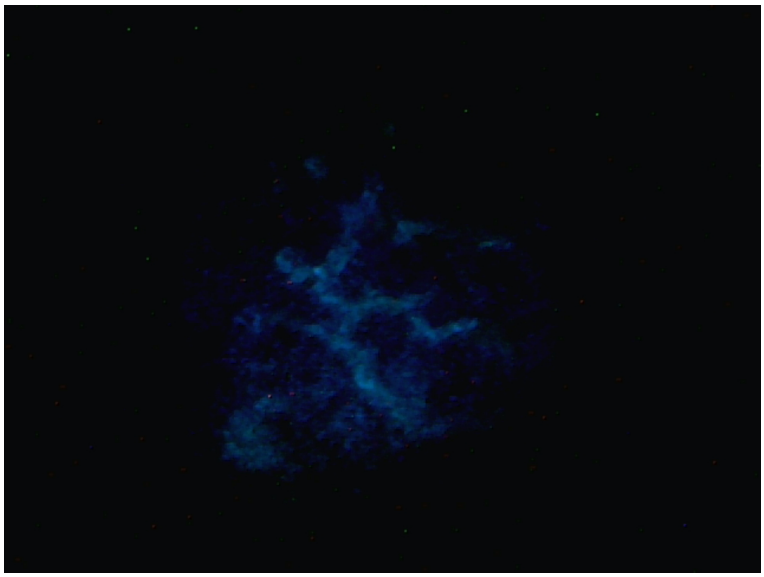

Figure 5.3: *Gel-like CdS nanocrystals agglomerates observed by crossed polarization.*

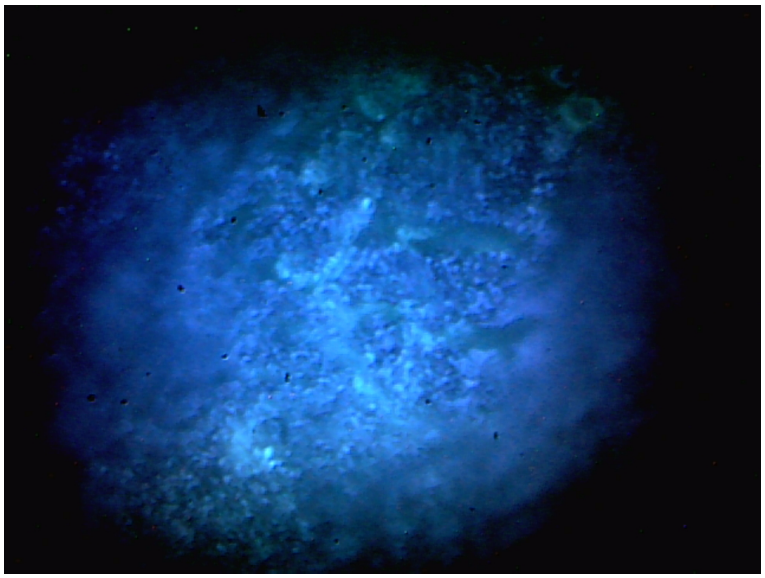

Figure 5.4: *Gel-like CdS nanocrystals agglomerates observed by parallel polarization. The contrast is much lower with respect to the observation with crossed polarization.*

5.1.2 TEM Characterization

Transmission electron microscopy (TEM) experiments were performed with a FEI TECNAI 12 G2 Twin operated at an accelerating voltage of 120 kV, equipped with an electron energy filter (Gatan Image Filter, BioFilter model) and a Peltier cooled charge-coupled device based slow scan camera (Gatan multiscan camera, model 794). The preparation of the samples consisted in solving the nanocrystals gels in chloroform and dropping it on a gold TEM gratings. The quick evaporation of the solvent leaves on the grating a very thin layer of material which can be analyzed by TEM. The accelerating voltages used range from 120 kV to 1 MV. The background of the images results to very noisy due to the presence of organic material mainly constituted by TOPO and residual stearic acid and the cadmium-stearic acid complex.
In the high resolution images obtained by accelerating potential of 1 MV, an atomic resolution was obtained. In figure 5.5, several nanocrystals lying in an area of 25×25 nm are visible. They are randomly oriented respect to their principal axis of symmetry. Some nanocrystals have the wurtzite c axis parallel to the image plane and the atomic planes are easily recognizable. Other nanocrystals have the c axis oriented more or less perpendicularly to the image plane. Even though the images are quite noisy, in these nanoparticles the hexagonal pattern is still recognizable and a Fourier analysis of the image provides the typical wurtzite reciprocal lattice Fig. 5.6. In figure 5.5, the distance between atomic planes was measured providing a value of the crystallographic parameter c ∼7 Å.This value is slightly larger bulk CdS value c=6.7490 Å obtained by X-ray diffraction measurements [28, 29] because of the crystal expansion occurring in nanostructures.

For each sample, a set of lower resolution TEM images (280 kV) were taken in order to carry out a statistical analysis. A large number of nanoparticles allows to use a gaussian statistic to determine the average diameter for each sample. As it can be seen from figure 5.7, all TEM images are rather noisy due to the large amount of organic material. The contours of the nanoparticles result to be in this way not well defined, and the measure of their size, diameter for instance, may result difficult. However, by digital filtration and contrast enhancement of the images, it is possible to better visualize the contours of the nanoparticles. For each sample, excluded sample 4 (t_{gwt}=360 s), by measuring the diameter of about one hundred nanoparticles, it was possible to perform the statistical analysis of diameters. With a number of counts superior to ∼80, the statistic distribution passes from discrete to continuous so that a continuous distribution function can be used. Unfortunately, the asymmetry of the distribution, caused by the processes described in 3.2.3 does not allow to use the Gaussian to fit the experimental data, Thus a more complicated function must be used. In figures 5.8, the histograms of diameter distribution of the four samples are presented. The counts of each bin in the histograms were interpolated by a spline function which was successively fitted by an asymmetric distribution function. The distribution function used is an asymmetric double sigmoidal

$$f(d,\bar{d},\sigma,\sigma_1,\sigma_2) = C + A\left[\left(\frac{1}{1+e^{\left(-\frac{(d-\bar{d})+\sigma/2}{\sigma_1}\right)}}\right)\cdot\left(1-\frac{1}{1+e^{\left(-\frac{(d-\bar{d})+\sigma/2}{\sigma_2}\right)}}\right)\right] \tag{5.1}$$

where d is the variable (quantum dots diameter), A is the weight of the function, C is the offset, $\bar{d}$ is the center value of the peak, i.e. the mean value of diameter, σ is the full width half height of the function, while σ_1 and σ_2 are the asymmetry parameters. This function was used because it enables to fit both kinds of asymmetries present in experimental data. Moreover, when the histogram is symmetric or almost symmetric ($\sigma_1 \approx \sigma_2$), the function 5.1 approximates quite

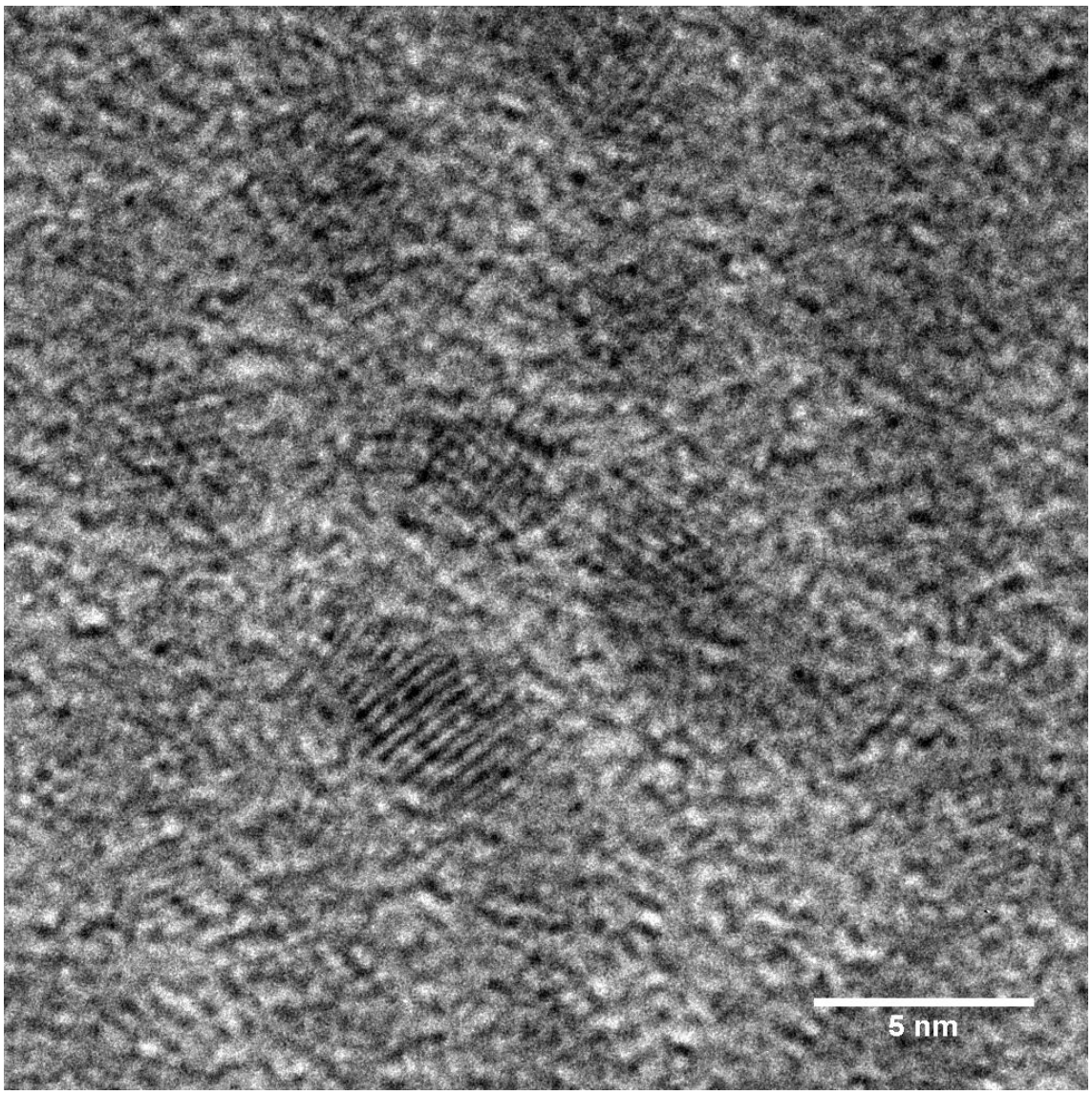

Figure 5.5: *TEM image of CdS nanocrystals, time of growth 120 s. The TEM accelerating voltage is of 1 MV, and the scanned area is of 24.58×24.58 nm.*

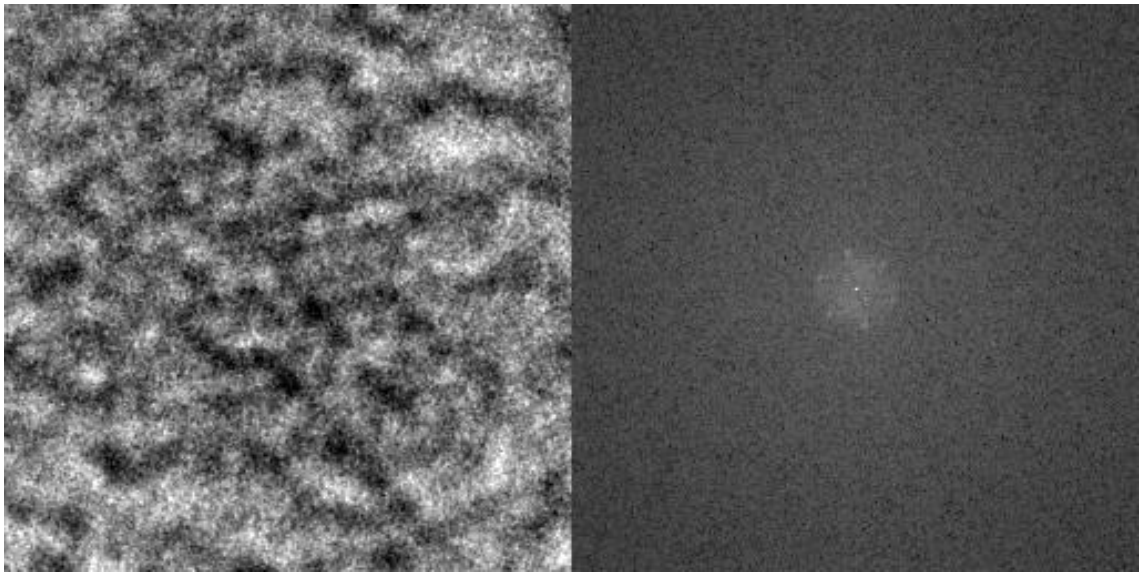

Figure 5.6: *Fourier transform of the top view of a single nanocrystal image extracted from 5.5. The FFT analysis provides the hexagonal reciprocal lattice pattern confirming the wurtzite modification of the grown CdS nanocrystals.*

well a gaussian distribution.
The values of nanoparticle mean diameters $\bar{d}$ with relative widths σ, obtained by the asymmetric fitting of the experimental data are listed in table 5.1. In figure 5.8 and in table 5.1 can be seen

Sample	Growth time (s)	$\bar{d}$ (nm)	σ (nm)
1	30	2.82 ± 0.02	1.68 ± 0.09
2	120	3.37 ± 0.03	0.90 ± 0.11
3	180	3.59 ± 0.01	1.42 ± 0.04
5	480	3.523 ± 0.005	1.12 ± 0.03

Table 5.1: *Results of the statistical analysis on TEM images for samples 1, 2, 3, 5.*

that the measured value of $\bar{d}$ for sample 3 is fairly anomalous. It results to be larger than the value obtained for sample 5, but this is not consistent with principles of colloidal growth described in chapter 3 and with the results of absorption and photoluminescence measurements shown in the next paragraphs. This anomaly probably arises from the worse quality of the TEM images which ends up affecting in a wrong way the size distribution.

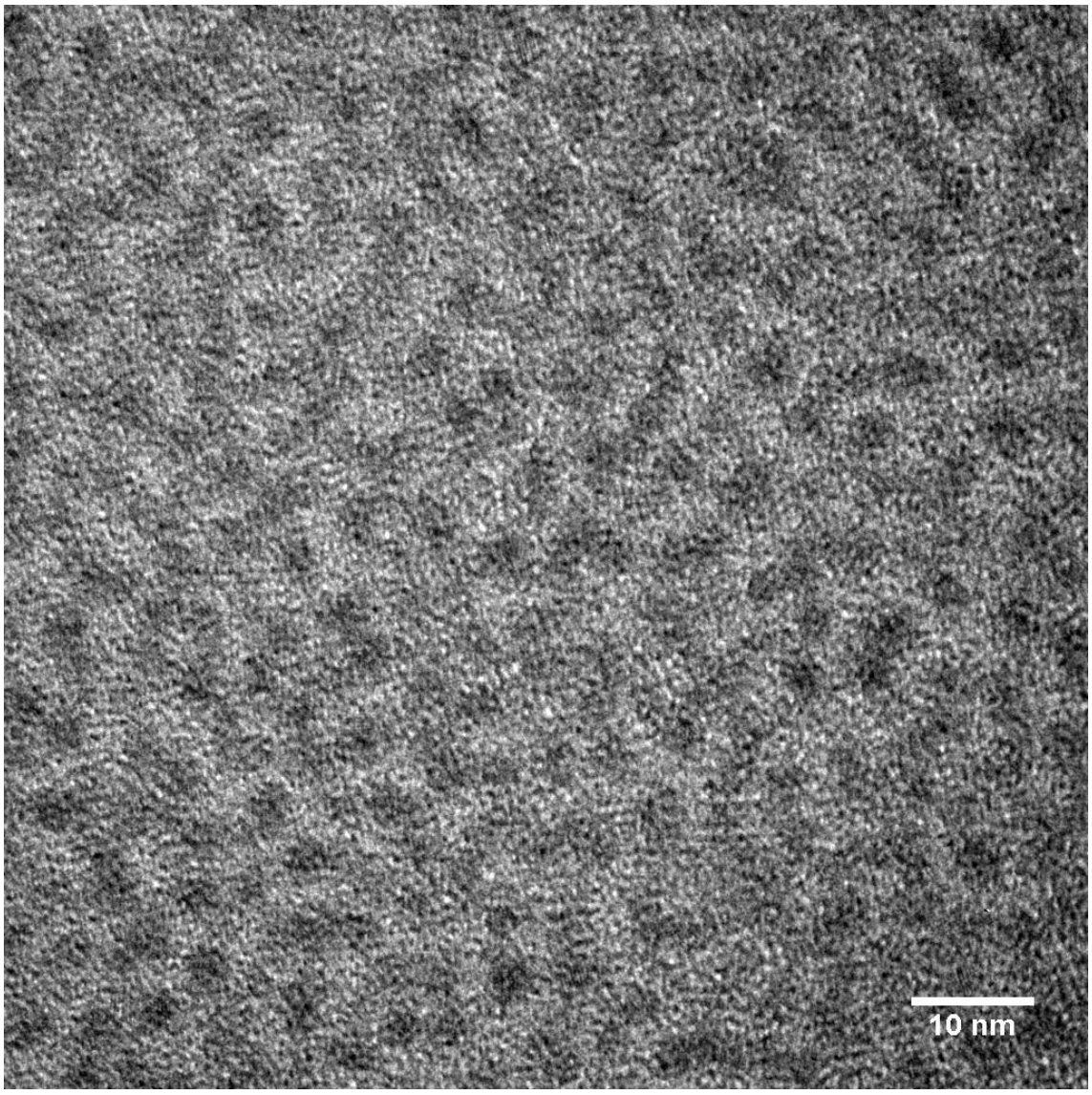

Figure 5.7: *TEM image of CdS nanocrystals sample 2 (time of growth 120 s), scanned area 88 nm×88 nm. The noisy background is due to the organic matrix embedding the nanocrystals (TOPO and stearic acid).*

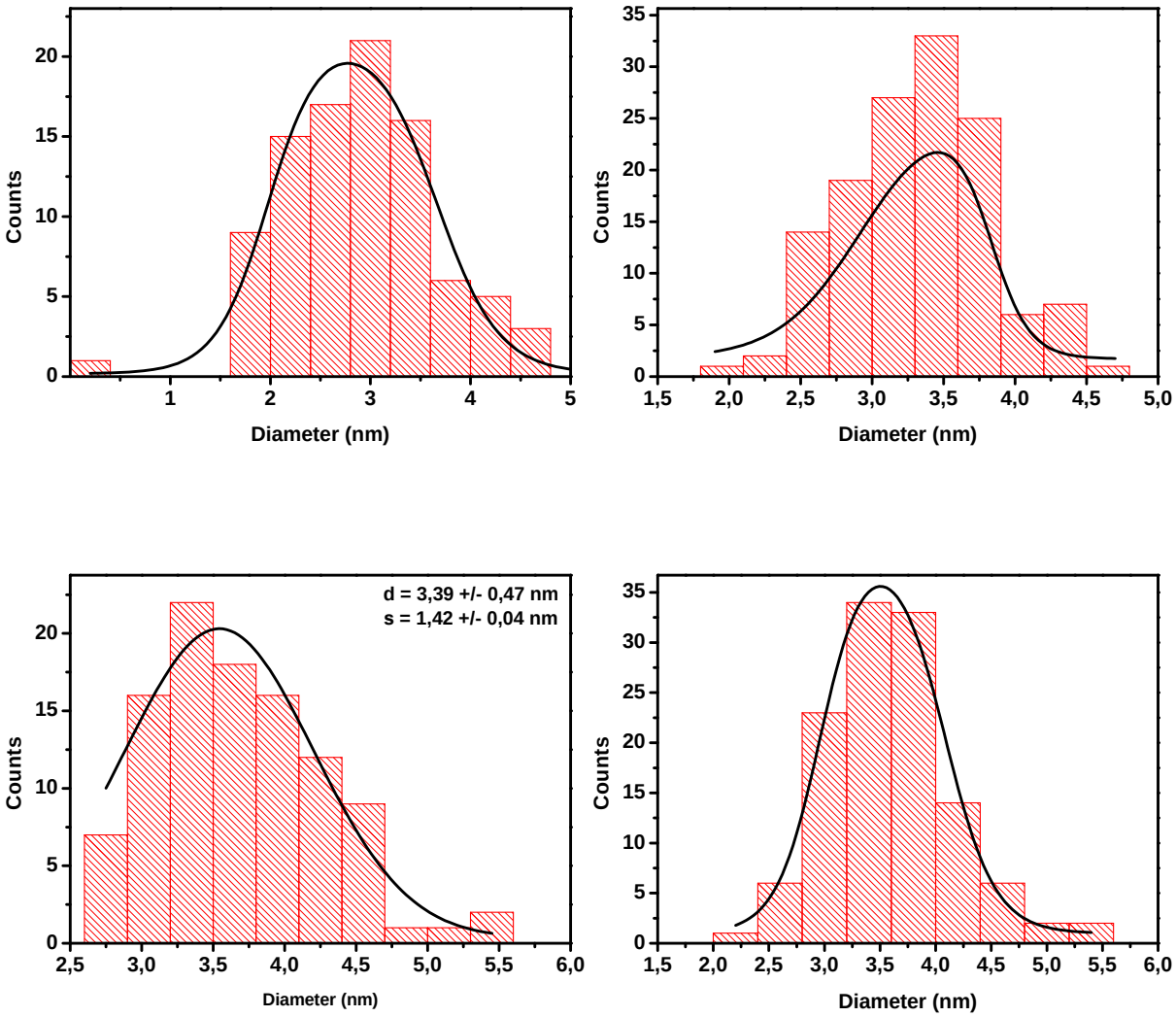

Figure 5.8: *Histograms of nanoparticles diameter measured from 280 kV TEM images. To notice that the statistical analysis of sample 4 (time of growth 360 s) is not present. This is due to the lack of TEM images of this sample caused by problems with TEM facility.*

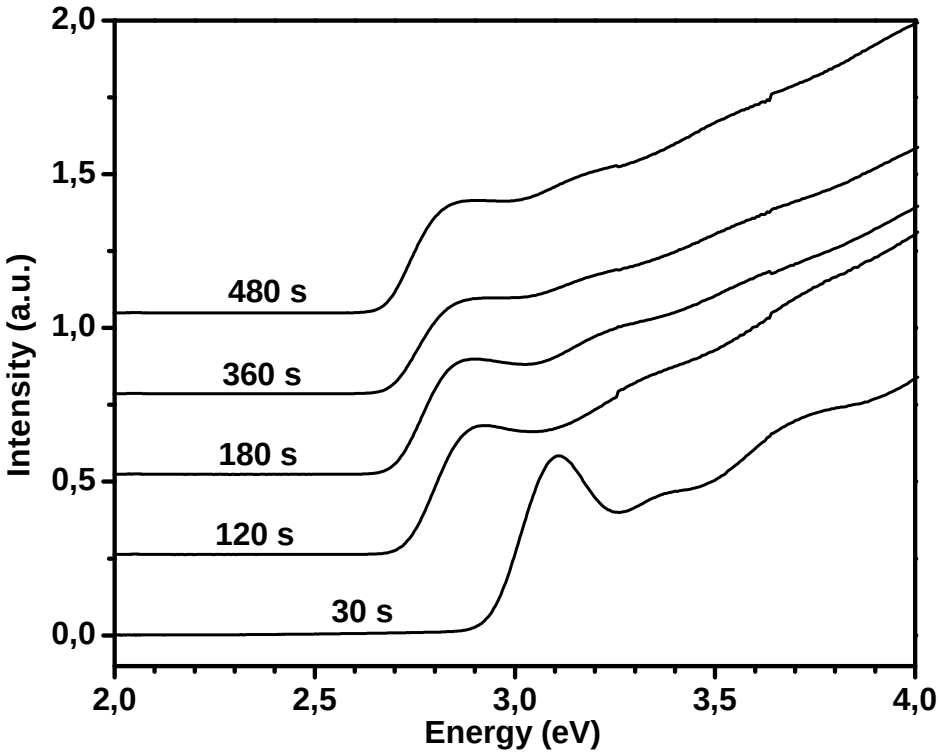

Figure 5.9: *Absorbance measurements of the five TOPO coated CdS nanocrystals samples solved in toluene. The spectra are ordered according to the time of growth reported in y axis. It is clearly visible how the line broadening increases with the growth time reflecting the defocusing of the size distribution.*

5.2 Optical Spectroscopies Results

5.2.1 Absorption Measurements

After the extraction and the purification, absorbance measurements were performed on all the quantum dots samples. The gel-like quantum dots consisting of TOPO-capped CdS nanocrystals were dissolved in toluene and loaded into a UV grade quartz SUPRASIL cuvette. The second cuvette was loaded with the blank solution (toluene). The two cuvettes are matched optically in order to reduce the optical errors. According to Lambert-beer's law $A = \alpha(\omega)\ell c$, already discussed in section 4.3, in order to have an acceptable signal and no saturation it would be opportune to estimate the right concentration to use. However, even though it is possible to calculate extinction coefficient $\alpha(\omega)$, the concentration can not be easily calculated since the solute has an unknown molecular weight. Therefore, the appropriate concentration was found empirically through several successive dilutions or concentrations. The absorption spectra reported in figure 5.9 show the typical features of II-VI semiconductors quantum dots [43]. In the spectrum of sample 1 (t_{gwt} =30 s), the first absorption peak lies at about 3.1 eV (400 nm), an energy much higher than the bulk band gap 2.4 eV (512 nm) [34]. This blue-shift means clearly that there is an opening of the band gap due to the quantum confinement. For the other four samples grown with longer time of growth, the energy of the first absorption peak decreases with respect to sample 1 due to the increasing of the diameter. In addition, with the increasing

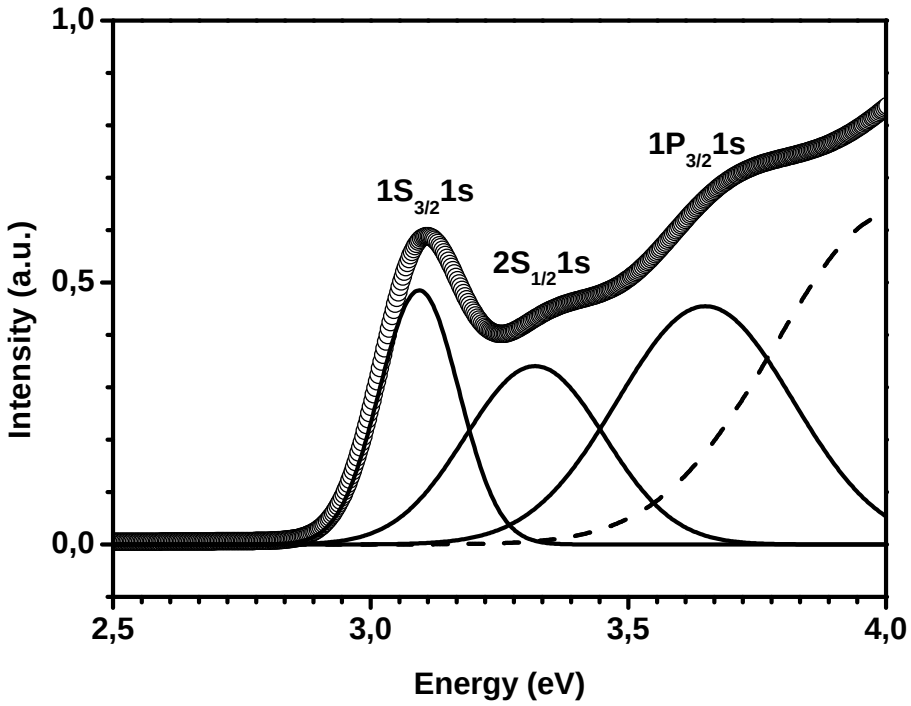

Figure 5.10: *Absorbance spectrum of sample 1 (30 s of growth) fitted using Gaussian lineshapes. Even though the model accounts the presence of only three peak the spectrum was fitted by four peaks. The fourth peak (dashed line) was used in order to fit the unresolved absorption bands at high energies. The background used for the fit was omitted in the figure.*

of the time of growth, there is a progressive broadening of the absorption peaks caused by the broadening of nanoparticle size distribution. This aspect is particularly visible in the first absorption peak. In every spectra, (except in sample 1) a very weak peak appears at about ∼700 nm (not showed in figure 5.9). This weak peak can be assign to the absorption of shallow levels [54].

The fits of absorption spectra was performed using a model accounting the three optical transitions: $1S_{3/2}1s$, $2S_{1/2}1s$ and $1P_{3/2}1p$. These are the transitions observable at room temperature, yet at very low temperature, other transitions are visible [43].

As seen in subsection 2.4.1, the radius dependence of quantum dot band gap is described fairly correctly, in the limit of strong confinement, by the Kayanuma's equation [6]. Corrections to this equation were introduced later by Brus [44]. The strong confinement holds when $r \ll a_B$ where a_B is the Bohr radius which for CdS is of 29 Å. Thus this model can be used since the radius of the studied quantum dots is below 29 Å. The corrected equation of quantum dot band gap in function of the radius was given already in 2.4.1 by equation 2.19. The exciton energy E^*_{Ry} for cadmium sulfide is of 29 meV. Rearranging equation 2.4.1 one obtains the expression of diameter d in function of the energy E. From the numerical evaluations, it can be seen that the Coulombian term $1.786\, e^2/\varepsilon r$ and the corrective term $0.248 E^*_{Ry}$ can be neglected. Therefore,

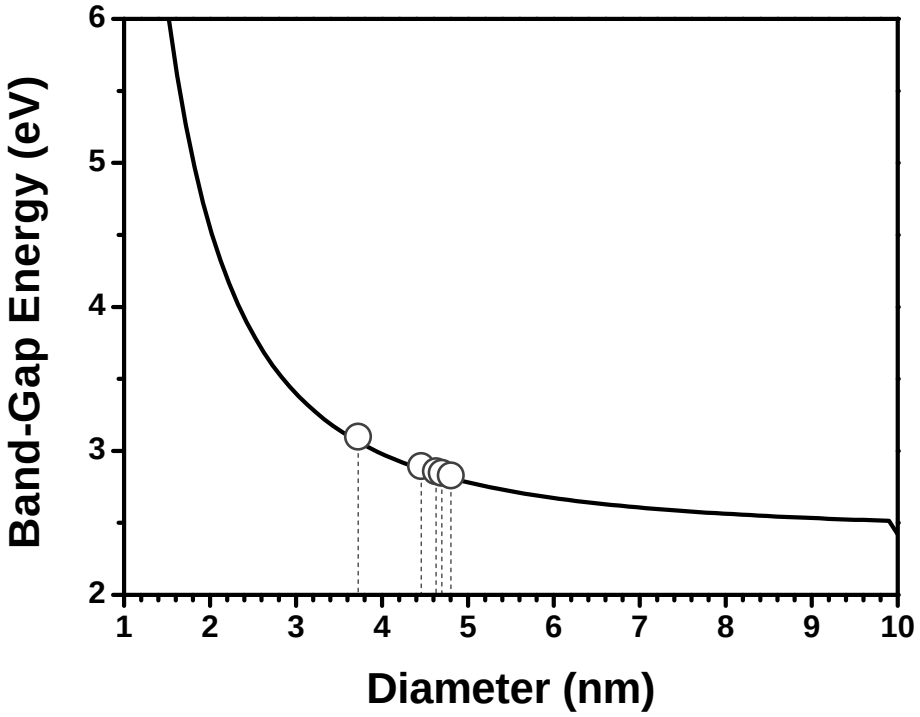

Figure 5.11: *Plot of 5.2 (full line). The experimental values of nanocrystals mean diameter calculated by 5.2 are reported on the curve (dots) with their error.*

the relation of diameter becomes rather simply

$$\bar{d} = \sqrt{\frac{2\pi^2\hbar^2}{\mu(E - E_g)}} \tag{5.2}$$

The error on the nanocrystal diameter was derived from the error propagation theory as follow

$$\Delta\bar{d} = \left|\frac{\partial\bar{d}}{\partial E}\right|_{E_0} \Delta E = \left(\frac{\pi^2\hbar^2}{2\mu}\right)^{-\frac{1}{2}} (E - E_g)^{-\frac{3}{2}}\, \Delta E \tag{5.3}$$

where ΔE is the sum of instrumental error ΔE_{inst} and the fit error ΔE_{fit}. As it is visible in figure 5.11, there is a relatively large difference in diameter, and consequently in energy of the first absorption transition, between the sample 1 (t_{gwt} =30 s) and the other nanocrystal samples grown with longer times. This is due to the very fast growth during the early stages of the growth and a successive depletion of the growing rate.
The results of the fits are reported in table 5.2. In figure 5.10, the result of the multipeak fit performed on sample 1 (t_{gwt} =30 s) absorption spectra is shown. In this case the fit gives the best results because the absorption bands are much more pronounced and sharp than in the spectra of the other samples (especially the first absorption transition).
As already seen, at least in part in section 4.3, the broadening of the absorption peaks is caused by a series factors such as lifetime broadening (thermal broadening), instrumental broadening, size and shape distribution, local environment fluctuation and chemical inhomogeneities [43].

However, these last two contributions can not be easily estimated. In section 4.3 of the previous chapter, we have seen that the absorption band linewidth $\Gamma(I)$ is intensity-dependent and that the lineshape is a gaussian distribution of lorentzian subbands. Thus, from the deconvolution of the gaussian absorption band, a set of subbands with different width, energy and statistical weight can be obtained. The instrumental broadening can be estimated to be of ∼10 meV and the thermal broadening of ∼25 eV, the absorption band can be deconvoluted obtaining the broadening (width) due exclusively to the size distribution

$$\sigma = \sqrt{\sigma_{Abs}^2 - \sigma_{inst}^2 - \sigma_{kT}^2} \tag{5.4}$$

where σ_{Abs} is the natural width of the absorption peak, σ_{inst} is the instrumental broadening and σ_{kT} is the thermal broadening. This width has still the dimension of an energy, thus it must be converted in unit of length (nm). The conversion can be readily done starting from the values of ω_0 and σ obtained by equation 5.4. Rearranging the Kayanuma relation one obtains

$$\sigma_d = \sqrt{\frac{2\pi^2\hbar^2}{\mu\left(\hbar\omega_0 - \hbar\sigma/2 - E_g\right)}} - \sqrt{\frac{2\pi^2\hbar^2}{\mu\left(\hbar\omega_0 + \hbar\sigma/2 - E_g\right)}} \tag{5.5}$$

All the values obtained by absorption measurements are reported in table 5.2.

5.2.2 Photoluminescence Measurements

Analogously to absorbance measurements, photoluminescence spectroscopy was performed on toluene solutions of TOPO coated CdS quantum dots. Also in this case, the concentration of the solution must be kept at an appropriate value in order to avoid the saturation of the signal and to have a reasonable intensity. The samples were excited with low intensity (Xe lamp) by an energy of 3.5 eV.
In figure 5.12 the photoluminescence spectra of the five samples are shown. The intensities has been normalized since the peaks have strong differences of intensity due to the different concentrations used. The energy shift of PL peaks, caused by electronic confinement follows the behavior already observed in absorbance spectra. According to what discussed in subsection 2.4.2, the PL spectra shown in figure 5.12 are only a small portion of the entire emission spectrum. The holes-electrons recombination from the deep and shallow traps gives rise to two broad low energy bands ∼1.7-1.8 eV (red PL). Such spectral range is not reported in the spectra of figure 5.12 since not relevant for the purpose of this study. The electron-hole recombination from the band gap gives rise to the band at higher energy ∼2.9-2.7 eV. However, as it can be seen in 5.13, the energy of this band is slightly red-shifted with respect to the first absorption transition $1S_{3/2}1s$ of about 150 meV. This shift can be attributed at least partly to a strong coupling with the phonon field in agreement with what discussed in [56]. Furthermore, it could be caused the inhomogeneous broadening and nonresonant excitation [43]. Therefore, the energy of photoluminescence band does not match the energy of quantum dot band gap, and in theory it would not possible to obtain E_g. However, since the red-shift of PL band is known, it is possible to estimate the nanoparticle diameters. Using the relation 5.2, the band gap energy is related to the energy of photoluminescence band through $E(R) = E_{PL} + \delta E$ where δE is the red-sift of the PL band with respect to the absorption transition $1S_{3/2}1s$ equivalent in energy to the band-gap. Thus, the mean diameter can be calculated likewise to what was done for the

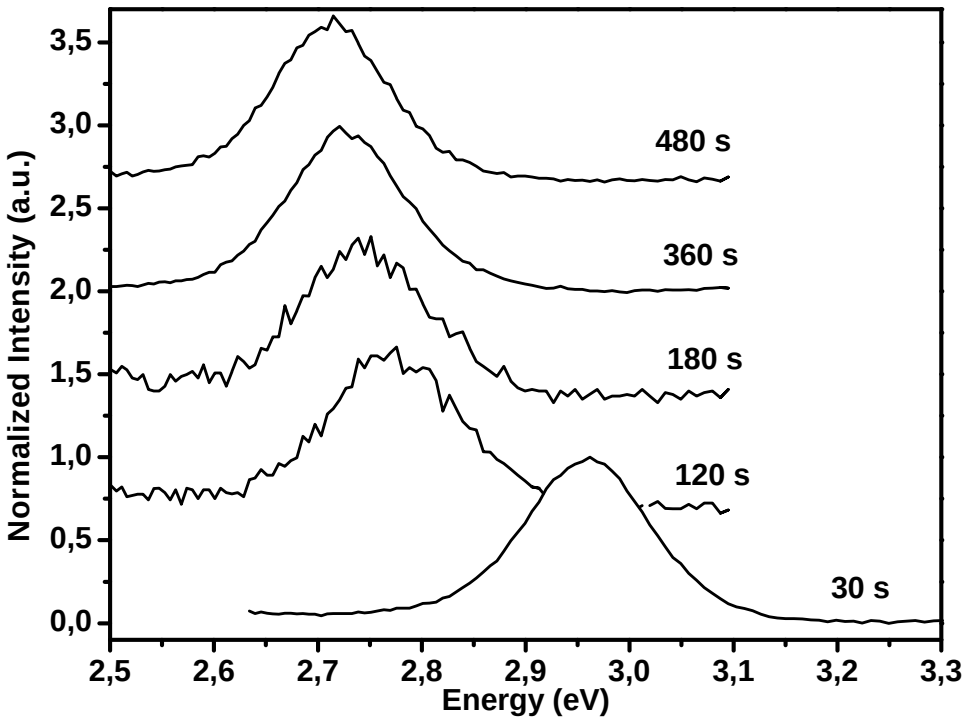

Figure 5.12: *Normalized photoluminescence spectra of every five samples.*

absorption peak

$$\bar{d} = \sqrt{\frac{2\pi^2\hbar^2}{\mu(E + \delta E - E_g)}} \tag{5.6}$$

The calculated values of are reported $\bar{d}$ in table 5.2

The photoluminescence band is the result of a convolution of a large number of subbands having a linewidth determined mainly by the lifetime. Each subband has then a proper statistical weight depending on the number of emitters contributing to that given subband. The causes of photoluminescence peak broadening are similar to the ones already seen for absorption. As seen in the former subsection, it may be caused by local environment fluctuation, chemical inhomogeneities but mainly by the thermal broadening, the instrumental broadening and by size-shape distribution. From the characteristics of the spectroflurimeter reported in 4.4.2, the instrumental broadening can be evaluated to be in the optimal case of $\sim$1 meV. Thus, it can be assumed that the lifetime broadening together with size and shape distribution remain the two main causes of line broadening. The lifetime broadening can be evaluated in first approximation to have a width of $\sim$25 meV which is essentially the thermal broadening kT. This value was measured also in a single quantum dot measurement performed at 300 K [114] where the linewidth was of $\sim$25 meV. It is thus possible to separate the two main sources of broadening, i.e. lifetime and size distribution deconvolving the photoluminescence peak with two gaussian functions. the width σ of the sole statistical contribution can be obtained through the relation

$$\sigma = \sqrt{\sigma_{PL}^2 - \sigma_{kT}^2} \tag{5.7}$$

where σ_{PL} and σ_{kT} are the widths of the observed PL peak and of the thermal broadening respectively. This width is expressed in energy but it can be converted into the width expressed

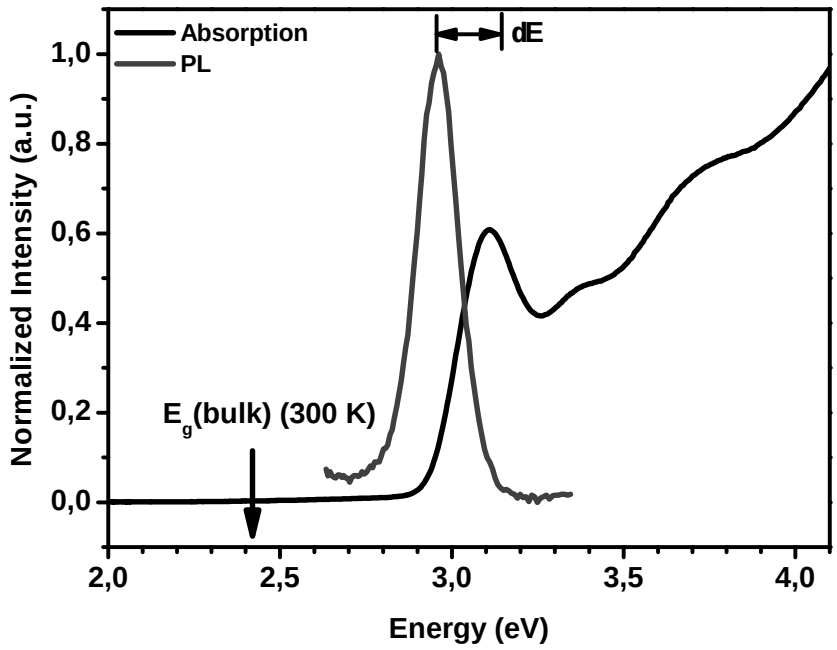

Figure 5.13: *Absorbance and photoluminescence spectra of sammple 1 (30 s of growth) quantum dots.*

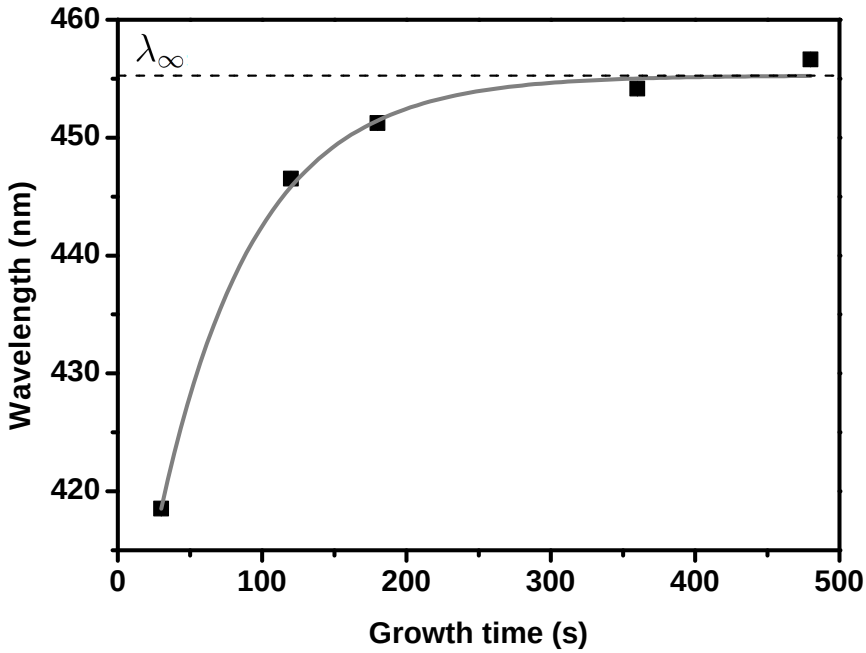

Figure 5.14: *Photoluminescence center-peak values plotted against the time of growth. The point of sample 1 is in the region of fast growth, while the rest of the samples lies in the quasi-stationary region where the precursors are almost totally consumed.*

in term of diameter. As explained in subsection 5.2.1, in a first approximation it is possible to estimate the width of diameter distribution. By the same principle, it is thus possible to estimate the diameter distribution σ even from the width of PL band. However, in this case it is necessary to include in the calculus the red-shift δE. The equation 5.5 already used to calculate the σ from the absorbance peak becomes for PL

$$\sigma = \sqrt{\frac{2\pi^2\hbar^2}{\mu\hbar\left(\omega_0 + \delta E - \sigma/2 - E_g\right)}} - \sqrt{\frac{2\pi^2\hbar^2}{\mu\hbar\left(\omega_0 + \delta E + \sigma/2 - E_g\right)}} \tag{5.8}$$

As it can be seen, the quantity δE is summed to the energy of the PL peak in order to account for its red-shift with respect to the $1S_{3/2}1s$ transition. Of course the non very accurate value of δE will introduce a certain error in this calculation. Nevertheless, even though the equation 5.8 is a not linear in δE, the error will be partially canceled out by the subtraction. The values of σ obtained by this method are listed in table 5.2 of the next subsection.
In figure 5.14, the photoluminescence center peak is plotted against the time of growth. The experimental data can be fitted very well by a function $\lambda(t) = \lambda_\infty[1 - \exp(-t/\tau)]$. It is clearly visible that just after the injection of sulfur precursor, the growth is very rapid and this regime is kept for about 2 minutes. At larger growth times, the growth rate decreases dramatically and the function tends asymptotically to a limit value λ_∞. This value is the photoluminescence band of the quantum dots whose radius is determined approximately by the stoichiometric condition 3.27. When the growth becomes stationary, it means also that one of the precursor (the one in defect) has been completely consumed and the Ostwald ripening is active.

5.2.3 Comparison of Quantum Dots Size and Size Distribution

The summary of average diameter $\bar{d}$ and the width of size distributions σ obtained by the methods quoted in the subsections 5.1.2, 5.2.1 and 5.2.2 are reported in table 5.2. It is fairly clear that there is not a good agreement between the diameter values obtained indirectly by absorption/photoluminescence measurements and the radius obtained by statistical analysis on TEM images. The diameter values obtained by TEM images result to be smaller in respect to the diameter obtained by absorption measurement. It can be observed that the diameters differ in average by $\sim$1 nm and such difference remains nearly constant at the varying of the diameter. Concerning the size distribution, the difference is even more marked. Regardless of the type of distribution used, sigmoidal asymmetric or gaussian, from the width σ it can be seen that the measured distribution is much broader in the case of statistical analysis of TEM images. In this case, it can be noticed how the width σ is totally disregarded from the mean diameter value, conversely the σ obtained from the absorption and photoluminescence measurements are dependent from $\bar{d}$. The σ's evaluated from the width of photoluminescence peaks have values analogue to the width obtained by absorption measurements. The large difference between the

Sample	t_{growth} (s)	$\bar{d}$ (nm)			σ (nm)		
		TEM	Abs.	PL	TEM	Abs.	PL
1	30	2.82 ± 0.02	3.725 ± 0.166	3.693 ± 0.148	1.68 ± 0.09	0.189	0.15
2	120	3.37 ± 0.03	4.457 ± 0.259	4.321 ± 0.217	0.90 ± 0.11	0.384	0.24
3	180	3.59 ± 0.01	4.629 ± 0.284	4.445 ± 0.237	1.42 ± 0.04	0.410	0.25
4	360	n.a.	4.696 ± 0.29878	4.533 ± 0.234	n.a.	0.41921	0.260
5	480	3.523 ± 0.3149	4.802 ± 0.006	4.608 ± 0.243	1.12 ± 0.03	0.434	0.265

Table 5.2: *Summary of average diameters and widths of diameter distributions obtained by statistic analysis of TEM images, absorption and photoluminescence measurements. The $\bar{d}$ and σ obtained by TEM are not available because of the TEM images are not available.*

width of size distribution obtained by the statistical analysis on TEM images and the widths obtained by the optical spectroscopies can be ascribed to the large difference of statistical significance. The statistical analysis on TEM images was done measuring the diameter of 100-120 nanoparticles, a number relatively small compared to the number of quantum dots contributing to the optical signal (Gaussian peak). Therefore, it is reasonable to think that in the case of the optical spectroscopies, the statistics is much better. Comparing the distribution obtained from the optical spectroscopies, the results from the absorption measurement are expected to be more reliable. It is reasonable to guess this, since a selective excitation of the quantum dots may occur (spectral hole burning) [43], and the width of PL peak could be affected by this effect. For this reason, further on, only the size distribution obtained from absorption peak will be take into account.

5.3 Raman Scattering Measurements

5.3.1 Experimental Procedures

The morphology of the TGA coated CdS nanocrystals is showed and described in subsection 5.1.1, it appears to be rather inhomogeneous, therefore to get good Raman spectra specific

areas must be opportunely chosen. Preliminary measurements showed that the laser beam when focused on stone-like CdS nanocrystal agglomerates visible in figure 5.2, gets easily damaged even using low power >1 mW cm^{-2}, with a consequent depletion of the signal, apparition of thermal effects and strong photoluminescence signal coming from the neighbor material. Conversely, when the laser beam is focused on different areas such as the gel-like spots 5.4, higher power can be used without burning the nanocrystals agglomerates and using appropriate laser power it is even possible to exclude thermal effects. Also the unwanted photoluminescence is dramatically reduced in these area. The fact that the stone-like agglomerates are much more easily damaged by the laser than the gel-like is that this second type of agglomerates are in a good thermal contact with the glass substrate. Therefore, the heat is partially transferred to it, vice versa, stone-like areas are constituted by a large volume of material in poor thermal contact with the glass substrate, and locally the temperature can reach very high values (hundreds of degrees) damaging the sample.
As already mentioned and proofed by the TEM images and absorbance/PL measurements, the nanocrystals samples have a certain size distribution which is maintained even after the TOPO replacement by thioglycolic acid. Since the light spot on the sample has a diameter of about 1 μm, i.e. an area much larger than the area scanned by TEM (88 nm$\times$88 nm), the signal will be the averaged over signals from particles of different sizes. It is of fundamental importance to know the size distribution.

5.3.2 Spectra Acquisition and Calibration

All the Raman spectra were acquired using long integration time in order to improve the signal to noise ratio. Usually the integration time is of 600 s for each cycle (3 cycles). This allows to remove all the not repeating events such as a cosmic particle striking one or more pixels of the CCD sensor. When the intensity of the Raman signal is sufficiently strong, shorter integration times can be used also. For the acquisition of these Raman spectra, two different integration times were used, 300 s and 600 s, in the case of stronger or weaker signal respectively.
All the acquired spectra were accurately calibrated by an experimental procedure. The calibration consists in acquiring after every long integration time spectrum, another spectrum in the same spectral region together with Ar^+ plasma lines. The plasma lines are allowed to pass by removing from the optical path the plasma lines interferometric filter. The very intense sharp lines appearing in the spectrum are fitted by a Gaussian lineshape. The use of gaussian lineshape is justified by the fact that the natural broadening of the plasma lines can be neglected with respect to instrumental broadening (Gaussian). Therefore, the plasma lines linewidth can be considered at any rate the instrumental resolution. Once the position ω_{pl} of the plasma lines are determined, their value are plotted against the literature values of Ar^+ atomic spectra and fitted by a polynomial equation. Usually, the light dispersion can be considered linear in the range of about 1000 cm^{-1}, thus a linear relation can be used.

$$\tilde{\omega} = a + b\,\tilde{\omega}_{exp} \tag{5.9}$$

where $\tilde{\omega}_{exp}$ is the measured wavenumber, while a and b are the intercept and the angular coefficient of the calibration curve. The Raman spectrum of interest (without plasma lines) is finally scaled by the equation obtained from the fit.
The error in wavenumbers affecting each spectrum can be calculated by the propagation errors

$$\Delta\tilde{\omega} = \left|\frac{\partial\tilde{\omega}}{\partial a}\right|_{\tilde{\omega}'} \Delta a + \left|\frac{\partial\tilde{\omega}'}{\partial b}\right|_{\tilde{\omega}'} \Delta b \tag{5.10}$$

where $\tilde{\omega}'$ is the value assumed by function 5.9 in a specified value of wavenumber, e.g. the position of one peak, while Δa and Δb are the errors of the calibration curve coefficients. To calculate this error, the error of the spectrum fit must be added too, i.e. the error of the peak center position $\tilde{\omega}_{fit}$. In total, the error on phonon frequency $\tilde{\omega}'$ is

$$\Delta\tilde{\omega} = \Delta a + |\tilde{\omega}|_{\tilde{\omega}'}\,\Delta b + \tilde{\omega}_{fit} \tag{5.11}$$

The errors calculated like this are reported as error bars in the graphics of figures 5.22, 5.23 and 5.26.
The calibrated spectra were successively multi-peak fitted. The fits are based on a model accounting two peaks to describe the asymmetric broadened LO peak, as well as the 2LO. This model was already used in many publications about Raman spectroscopy on II-VI semiconductors [25, 115, 116]. The fits were performed using Voigt lineshape, a convolution between lorentzian lineshape and gaussian lineshape.

$$\begin{aligned} V(\omega-\omega_0,\sigma,\gamma) &= G(\omega_0,\sigma) * L(\omega-\omega_0,\gamma) = \int_{-\infty}^{+\infty} G(\omega',\sigma)L(\omega-\omega',\gamma)d\omega' \\ &= \frac{\gamma}{\pi\sqrt{2\pi\sigma^2}}\int_{-\infty}^{+\infty}\frac{e^{-\frac{\omega'^2}{2\sigma}}}{(\omega-\omega')^2+\gamma^2}d\omega' \end{aligned} \tag{5.12}$$

This lineshape was used since the signal observed is a convolution of the Gaussian instrumental broadening and the Lorentzian broadening due to finite phonon lifetime. The Voigt-line parameters ω_0, σ, γ and A are respectively the frequency central position, the gaussian width, the lorentzian width and the integral area of the peak (normalization constant). The Gaussian width σ is imposed as fixed parameter defined by the average value of plasma lines width used to calibrate the spectrum. The other parameters were let free to variate until convergence. In every spectrum, a luminescence background, in some cases is very strong is always present. This background is removed introducing in the fit a function approximating such broad background. However, the background curve is not reported in the spectra of figures 5.17, 5.18, 5.19, 5.20 and 5.21.

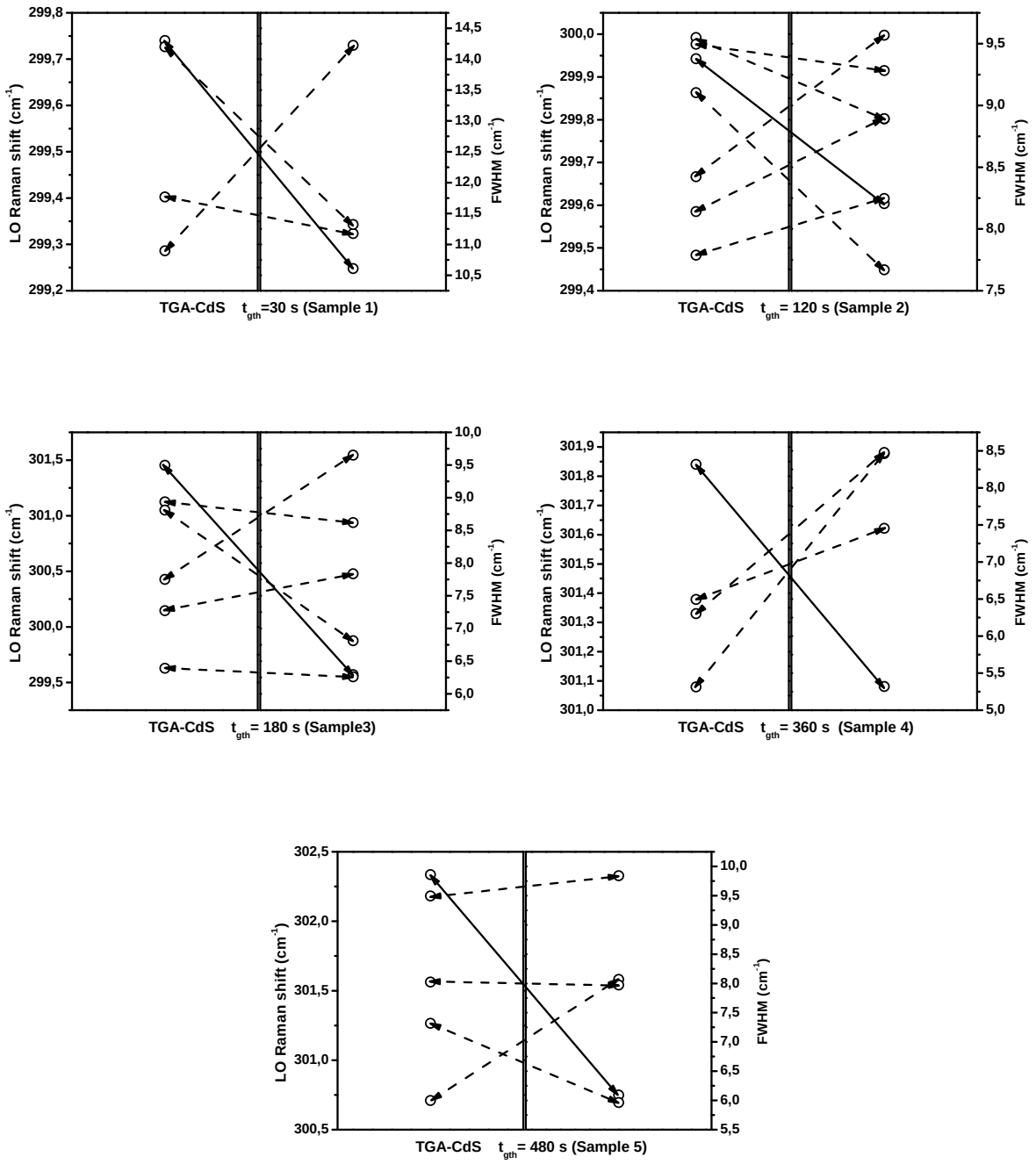

Figure 5.15: *Correlation diagrams between frequency ω and FWHM (γ of lorentian contribution) of phonon peaks relative to measurement on the five TGA-CdS quantum dots samples grown with 30 s, 120 s, 180 s, 360 s, 480 s. Each diagram is constituted by two quadrants. In the left hand quadrant the experimental $\tilde{\omega}_{LO}$ are plotted in the vertical scale, while in the right hand quadrant the experimental linewidth γ_{LO} are reported. The continuous arrowed line represents the measurements with the smallest thermal effects, while the dashed arrowed lines represent the ones with higher thermal contributions.*

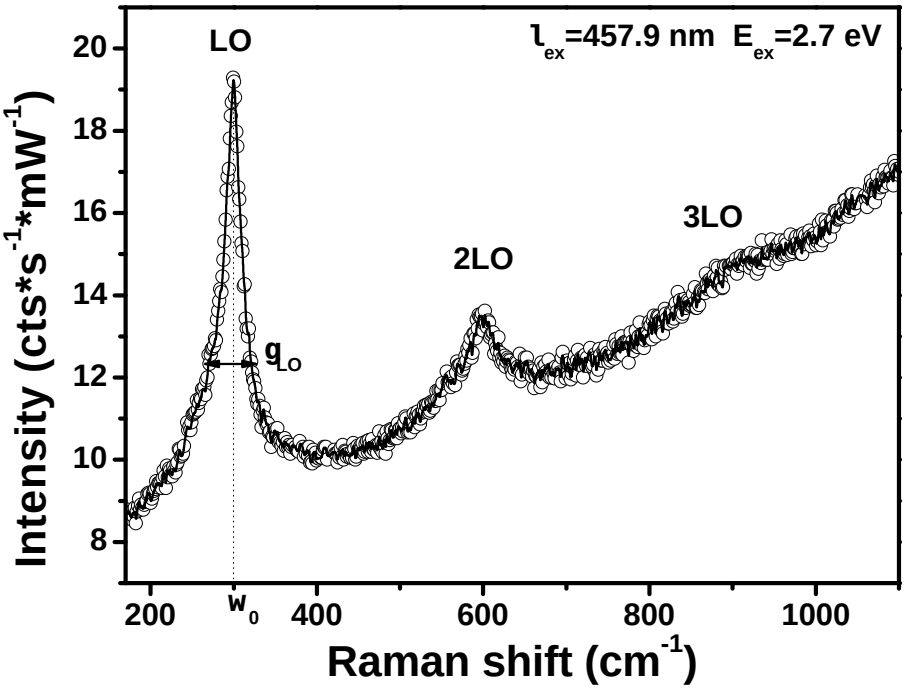

Figure 5.16: *Raman spectrum of CdS quantum dots taken on sample 1 (t_{gwt}=30 s). The strong slope of the background is due to the quite intense luminescence emission.*

5.3.3 Spectra Selection

As already seen in section 5.1.1, the TGA-CdS quantum dots samples was spin casted on microscope glasses 10×10 mm and the Raman spectra acquired from different areas of each sample. For each sample, from four to seven Raman spectra were acquired. In spite the use of very low laser power, residual thermal effects were still visible as the not negligible deviations from the mean frequency. To take the average value as final result would not be correct since the average frequency will contain the thermal effects as well. Thus, for each sample, it is necessary to select a spectrum where the thermal effect is the small as possible.
A typical Raman spectrum of spectrum of CdS quantum dots is shown in figure 5.16. As seen in subsection 5.3.2, the Raman line is expected to have a Voigt lineshape that is characterized by the parameters center peak frequency $\tilde{\omega}_0$, the gaussian width σ and the lorentzian width γ. This last width and the frequency are the two parameters affected by the thermal effects. As a consequence, the increase of temperature of the material is visible in Raman spectra as a broadening of the phonon line (increasing of γ), a red-shift of the frequency $\tilde{\omega}_0$ and asymmetric line broadening caused by the potential anharmonicity [117]. Based on what discussed above, to identify the spectrum having the smallest value of γ_{LO} and largest of $\tilde{\omega}_{LO}$ will mean to identify the spectrum with the smallest thermal effects. The selection is done making use of correlation diagrams shown in figures 5.15. Each correlation diagram represent one sample, for which from 4 to 7 spectra were acquired. In the left hand quadrant of the diagrams in the vertical scale the LO phonons frequencies are plotted, while in the right hand quadrant the width values γ of the LO phonon peaks are plotted. The data points of $\tilde{\omega}_{L0}$ and γ_{LO} belonging to the same

spectrum are correlated by a double arrowed line. It can be observed that the correlation lines have different lengths, slopes and sign of the slopes. The behavior of these lines were chosen as criteria to select the spectra with low or null thermal effect. The correlation lines having a positive slope represent the LO peak with larger γ and smaller $\tilde{\omega}_0$, while correlating lines with negative slopes represents LO peak with smaller γ and larger $\tilde{\omega}_0$. Therefore, the latter cases represent the spectra having the smallest thermal contribution. Among them, the spectrum with the smallest thermal contribution is the one with the longest correlating line. In diagrams of figure 5.15, the measurement with the smallest thermal contribution is represented by a full line, while the dashed lines represent the discarded spectra. The measurements with the smallest thermal effect are thus considered the most reliable and were chosen to carry out the study of phonon confinement.

5.3.4 Description of the Spectra

When Raman spectroscopy is performed on samples consisting of randomly oriented nanocrystals, the selection rules, valid for single crystals having a specific geometrical orientation with respect to polarized light, become negligible. Thus, all Raman active modes are theoretically observable since there will be a contribution of every mode in any direction of the space. Nonetheless, several experimental made on CdS, CdSe and CdTe nanocrystals, e.g. [25, 115] show that the $A_1(LO)$ mode with the relative overtones is largely predominant. This feature can be explained by the fact that $A_1(LO)$ Raman tensor is always symmetric with any orientation of the light. Moreover, only the intensity of LO modes will result to be enhanced in resonance condition due to the strong interaction between the electrons and the macroscopic longitudinal field produced by LO phonons (Frölich interaction), see subsection 4.2.2. The ratio between the intensities of the multi-phonons and the single-phonon scattering is also related to the nanoparticles size. According to [21], this intensity ratio results to be smaller in smallest particles due to the reduction of the coupling between lattice vibrations and the lowest excited electronic state. The spectra of CdS nanocrystals samples were acquired in an wavenumber interval going from 160 cm^{-1} to 1200 cm^{-1}. It was not possible to extend the interval to lower wavenumbers due to the strong Raleigh scattering. All the spectra are characterized by the $A_1(LO)$ phonon mode with its two overtones, processes of two and three phonons respectively. The one phonon process appears as an intense line at about 300 cm^{-1}. The two phonon process appears at about 600 cm^{-1} with much less intensity, finally is still observable the three phonon processes at about 900 cm^{-1}. The one phonon peak is clearly asymmetrically broadened due to the phonon quantum confinement effect. Moreover, a shoulder at lower wavenumbers, about 270 cm^{-1} indicates the presence of another peak. This peak is in some cases described as a surface mode [24, 118], while in other cases it is interpreted as an effect of the new selection rules coming from the reduced size effects [20, 25, 115]. The most important feature of these nanocrystals spectra is however the shifting toward lower wavenumbers with respect to the bulk line. In smallest particles the crystalline structure tends to expand in order to minimize the total energy of the crystal. Due to this expansion, there will be also an increasing of the interatomic distance which will decrease the force constant and therefore the frequency of oscillation, see subsection 2.3.1. The fitted Raman spectra are shown in figures 5.17, 5.18, 5.19, 5.20 and 5.21.
The diameter dependence of LO and 2LO modes are shown in figures 5.22 and 5.23. The values of diameters used are obtained from absorbance spectra according to what was discussed in subsection 5.2.1. In both graphics it is observable in figure 5.22 that for samples 1, 2 and 3 the phonon frequencies are red-shifted with respect to the bulk frequency (302.2 cm^{-1} at 300 K

[27]). Nevertheless, in samples 4 and 5, the phonon frequency is anomalously higher than the bulk frequency. The behavior of 2LO phonon shown in figure 5.23 is more reliable since all the frequencies are red-shifted in respect to the bulk frequency (604 cm^{-1} [111] and ω_{2LO}=604.4 cm^{-1}). Moreover, the trend of phonon frequencies is much closer to what expected. In figures 5.24 are shown the diameter dependence of the phonon linewidths γ_{LO} and γ_{2LO}. It can observed in both graphics that the linewidth decreases at the increasing of nanoparticle diameter. This behavior can be explained by the fact that in largest nanoparticles, due to their higher thermal-dissipative capability, the thermal effects are less relevant than in the smaller nanoparticles, and consequently the linewidth will be narrower.

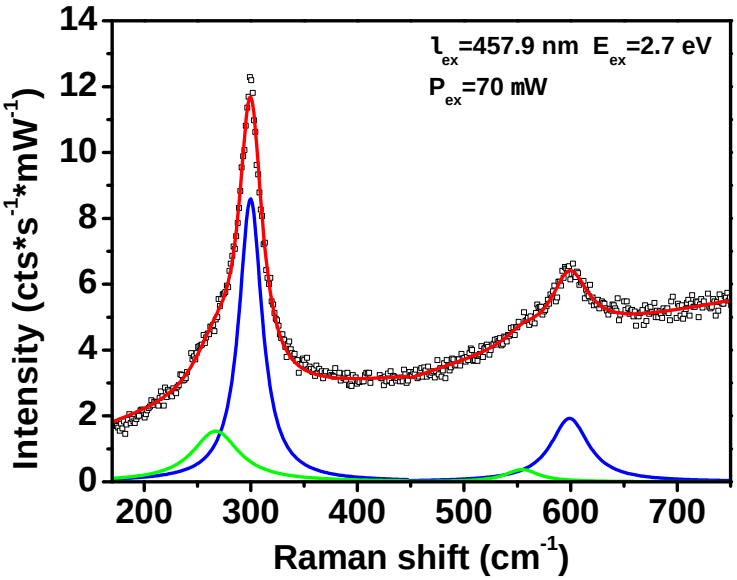

Figure 5.17: *Raman spectrum of TGA-CdS nanocrystals* $\boldsymbol{t}_{growth}$*=30 s (sample 1). The scattered points are the experimental data, the red continuous line is the result of the fit, the blue lines are the LO an 2LO peaks, while the green lines are the supposed surface modes SO and 2SO. The fit was performed in two distinct spectral regions and the background was subtracted by a suitable curve not reported in the image.*

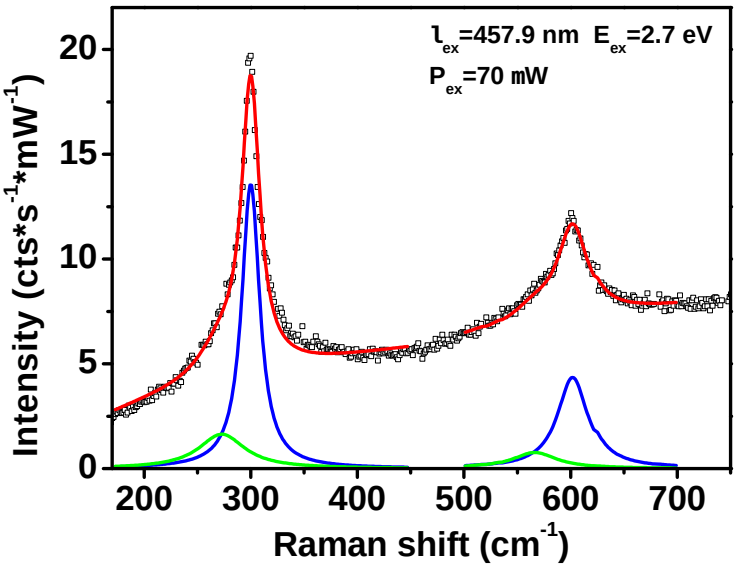

Figure 5.18: *Raman spectrum of TGA-CdS nanocrystals* $\boldsymbol{t}_{growth}$*=120 s (sample 2). The scattered points are the experimental data, the red continuous line is the result of the fit, the blue lines are the LO an 2LO peaks, while the green lines are the supposed surface modes SO and 2SO. The fit was performed in two distinct spectral regions and the background was subtracted by a suitable curve not reported in the image.*

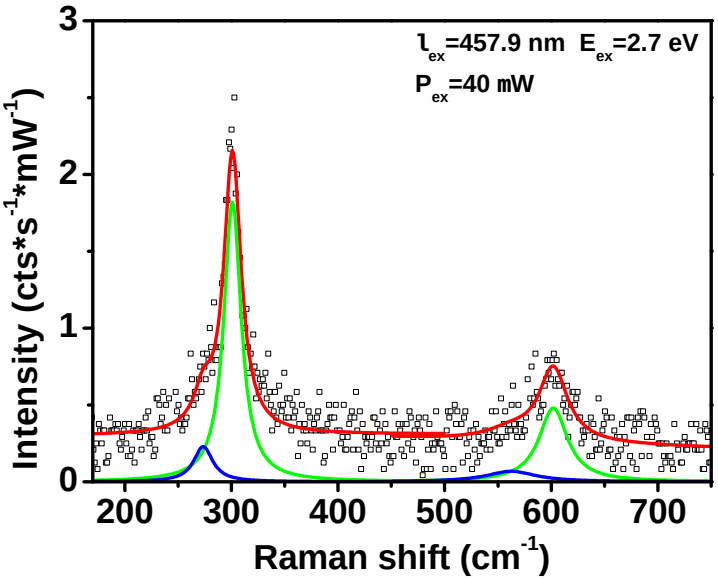

Figure 5.19: *Raman spectrum of TGA-CdS nanocrystals* t_{growth}*=180 s (sample 3). The scattered points are the experimental data, the red continuous line is the result of the fit, the blue lines are the LO an 2LO peaks, while the green lines are the supposed surface modes SO and 2SO. The fit was performed in two distinct spectral regions and the background was subtracted by a suitable curve not reported in the image.*

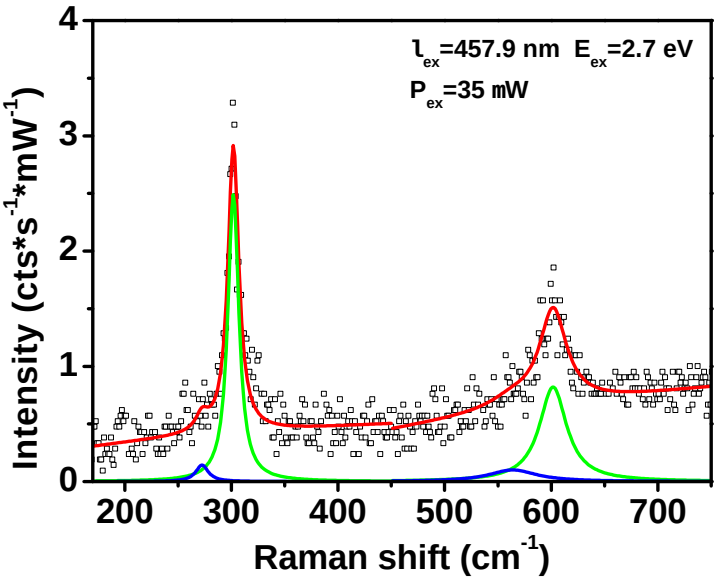

Figure 5.20: *Raman spectrum of TGA-CdS nanocrystals* t_{growth}*=360 s (sample 4). The scattered points are the experimental data, the red continuous line is the result of the fit, the blue lines are the LO an 2LO peaks, while the green lines are the supposed surface modes SO and 2SO. The fit was performed in two distinct spectral regions and the background was subtracted by a suitable curve not reported in the image.*

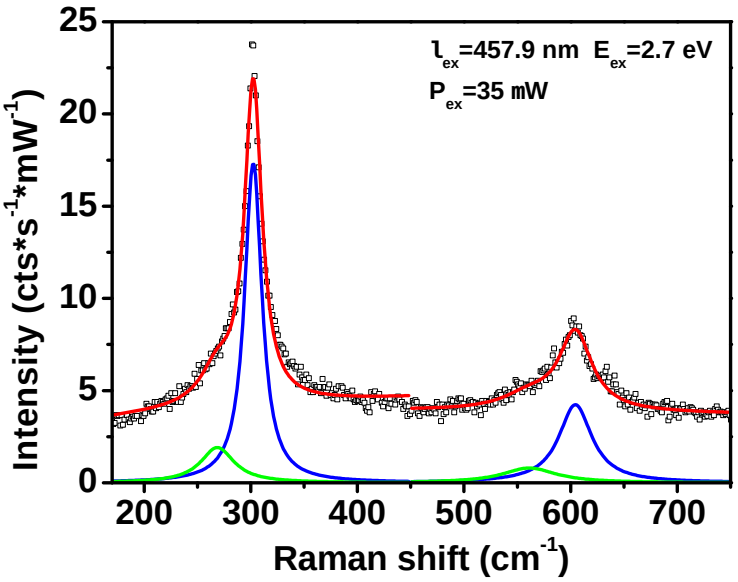

Figure 5.21: *Raman spectrum of TGA-CdS nanocrystals* $t_{growth} = 480\,s$ *(sample 5). The scattered points are the experimental data, the red continuous line is the result of the fit, the blue lines are the LO an 2LO peaks, while the green lines are the supposed surface modes SO and 2SO. The fit was performed in two distinct spectral regions and the background was subtracted by a suitable curve not reported in the image.*

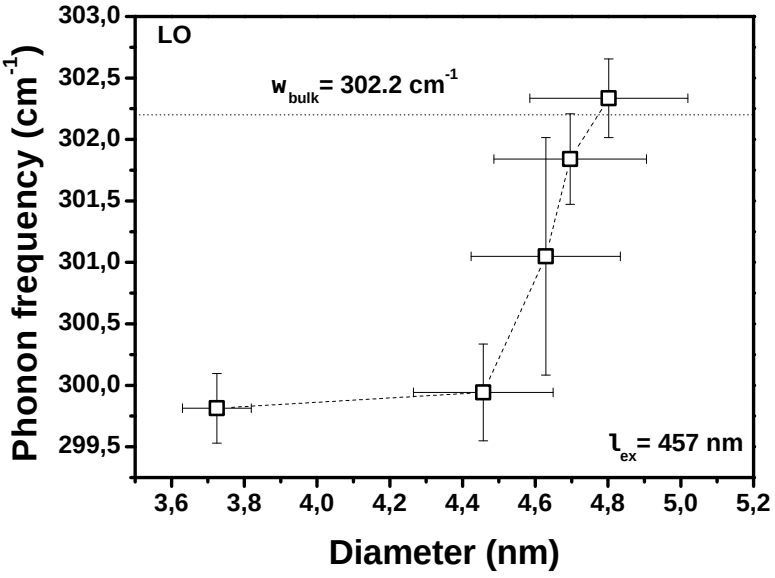

Figure 5.22: *LO Raman shift in dependence of particle diameter.*

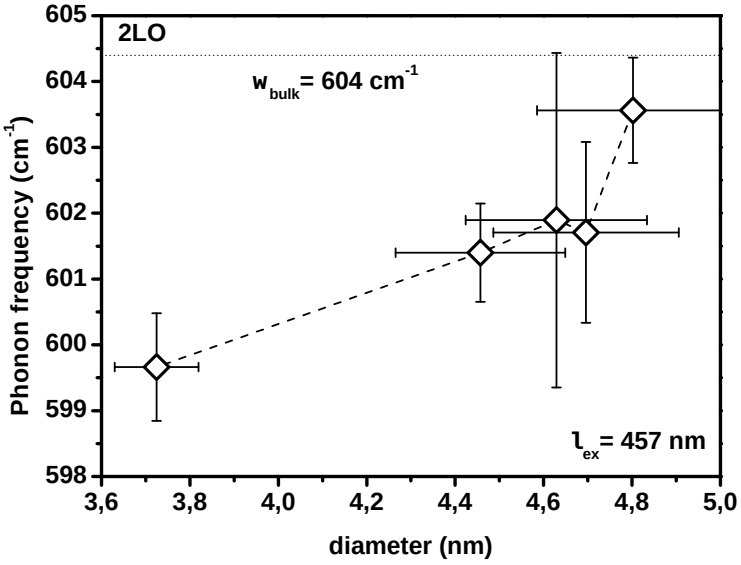

Figure 5.23: *2LO Raman shift in dependence of particle diameter.*

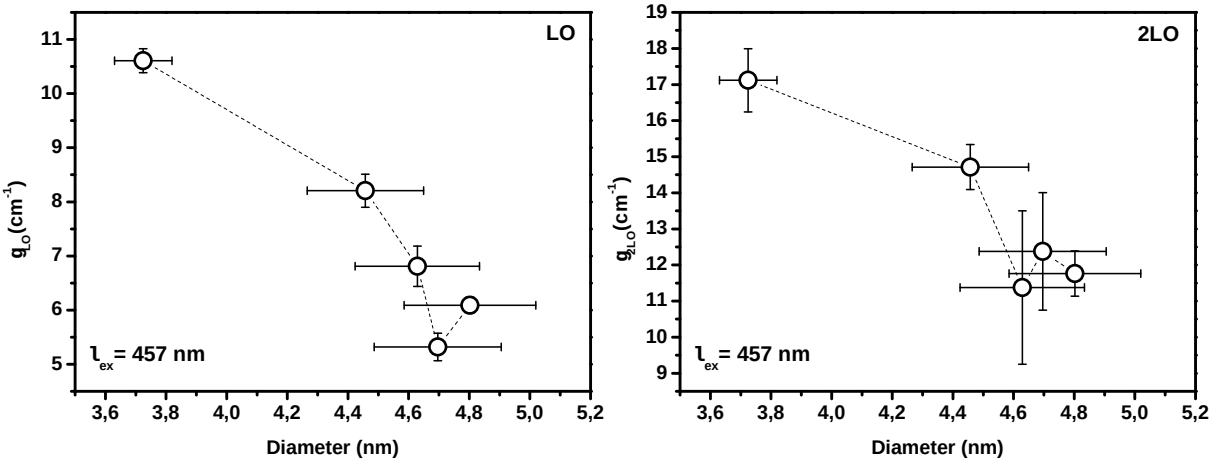

Figure 5.24: *Experimental diameter dependence respectively of γ_{LO} (left) and γ_{2LO} (right).*

5.4 Comparison with Theory

The main aim of this Raman scattering study is to verify and derive structural information by cross checking experimental Raman data with the available theories describing the quantum confinement of phonons in 0-dimensional nanostructures. The theories taken into account are the one based on the continuum model described in subsection 2.5.2 and the theory on surface phonons in subsection 2.5.3.
These two theories are somewhat complementary since the continuum model can be used to interpret the red-shift of the line at the decreasing of the size, while the apparition of extra peak can be explained by the presence of surface modes. However, continuum model can also explain the presence of extra peaks as a manifestation of phonon confinement.

5.4.1 Comparison with Continuum Model

According to [9], the quantum confinement of phonons in nanostructures produce the apparition of LO and TO extra-peaks with frequencies ω_n given by the equation 2.31. The first order LO peak can be calculated using the values of mean diameter of the nanoparticles $\bar{d}$ obtained by equation 5.2, and using the material parameter $\beta_L = 5.04\, ms^{-1}$ taken from [9]. The μ_n are the roots of a zero order Bessel function j_0. Here it was calculated ω_n only for $l = 0$ and $n = 1, 2, 3$, therefore it necessary to evaluate the three roots of Bessel functions. They have the following values: $\mu_1 = 2.405$, $\mu_2 = 5.520$ and $\mu_3 = 8.654$. Another parameter occurring in the equation 2.31 is the longitudinal phonon frequency of bulk CdS ω_{LO}. The frequency value used was taken from [27] and it is of 302.2 cm^{-1}. This value of ω_{LO} is relative to Raman measurements performed at room temperature (T=300 K) which is reasonably, the same temperature at which the Raman measurements of the present study were performed (neglecting the laser heating). In figure 5.25, it can be observed how the size reduction produces multiple phonon peaks of order $n = 1, 2, 3$. The splitting between these multilines increases with the reduction of the diameter and simultaneously there is a red-shift of the phonon frequencies. For the first order phonon peak ($l = 0$ and $n = 1$), the confinement effects start to be visible only at low values of diameter, $\bar{d} \lesssim$6 nm, while for the other order modes, namely $n = 2.3$, the quantum effects are still visible even for larger sizes. The intensity of these modes is the highest for $n = 1$, while it decreases progressively at the increase of n [20]. Now, let examine the comparison between the theoretically predicted and experimental data. In figures 5.26, the experimental frequencies of LO and 2LO (half frequency) modes together with the calculated phonons frequencies with $l = 0$ and $n = 1$ are plotted in dependence of the nanoparticle mean diameter. The frequency of 2LO phonon is about the double of the LO, thus dividing it by 2 one gets with a good approximation the $\omega_{2LO}/2$ frequency. It appears clear soon that there is not a good agreement between the experimental ω_{LO} and the theoretical phonon frequencies $l = 0$ and $n = 1$. Conversely, there is a surprising good agreement between the theory and the experimental $\omega_{2LO}/2$. In this case, within the error, the experimental frequency values match very well the theoretically predicted frequencies.

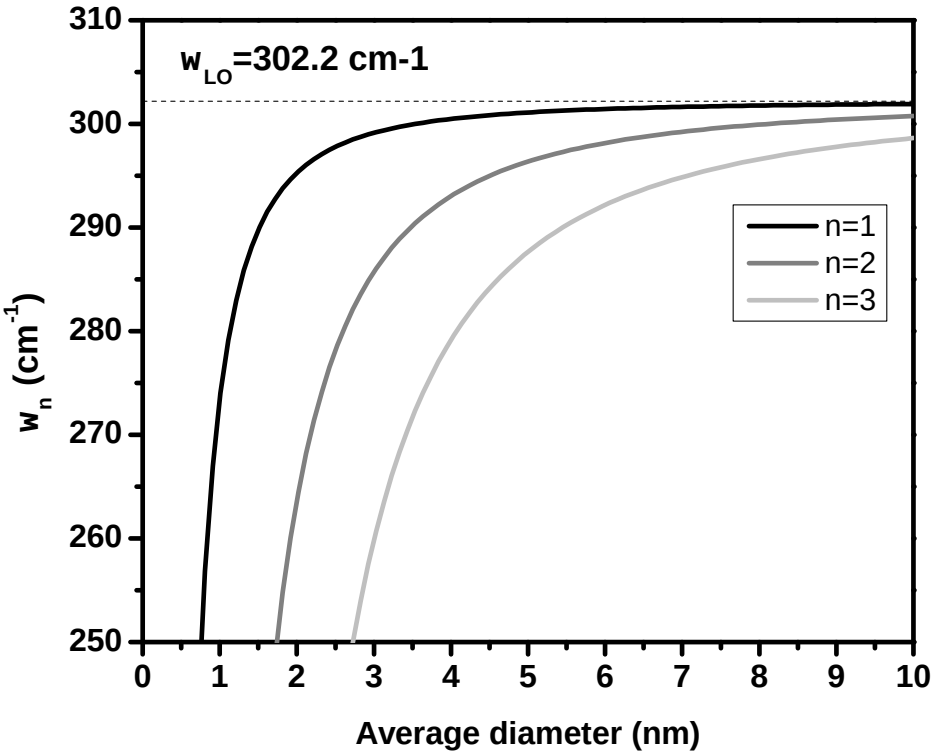

Figure 5.25: *Plots of ω_n against the nanoparticles mean diameter $\bar{d}$. The three curves are relative to the quantum numbers $l = 0$ and $n = 1, 2, 3$.*

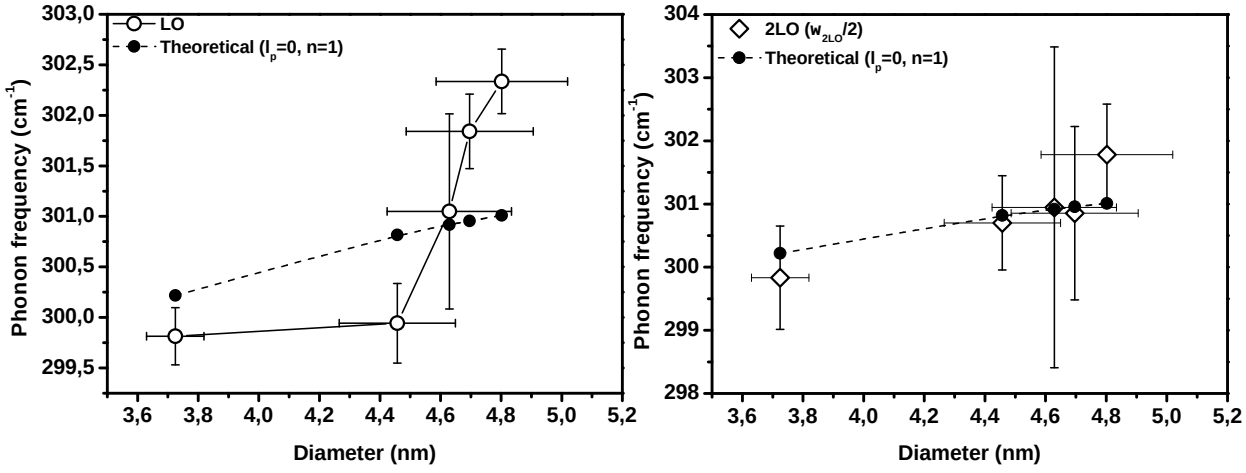

Figure 5.26: *Diameter dependence of experimental LO phonon frequencies and theoretically predicted frequencies for mode with $l = 0$ and $n = 1$ (left). Diameter dependence of experimental 2LO phonon half frequencies and theoretically predicted frequencies of mode with $l = 0$ and $n = 1$ in dependence of the quantum dots diameters (right) . The quantum dots diameters are obtained by the energy of $1S_{3/2}1s$ absorption transition.*

ε_m	1	1.5	2	2.5	3
ω_{srf} (cm^{-1})	285.82	280.40	276.09	272.56	269.63

Table 5.3: *Values of ω_{srf}'s calculated by equation 2.41 using several arbitrary ε_m's.*

5.4.2 Interpretation by Surface Modes

The multipeak fits of Raman spectra shown in the figures 5.17, 5.18, 5.19, 5.20 and 5.21 put in evidence the presence of two additional peaks close to ω_{LO} and ω_{2LO} respectively. This mode, in basis of what discussed in section 2.5 and according to several publications [10, 15–17, 22–24] can be attributed to surface modes. However, none of these articles give an exhaustive physical explanation. The Raman spectra of samples 3 and 4 (figures 5.19 and 5.19) will not be discussed here, since the spectra result to be rather noisy and the peak position of surface mode is expected to have a strong uncertainty. The Raman spectra of samples 1, 2 and 5 shown in figures 5.17, 5.18 and 5.21 have instead a good signal to noise ratios and the position of the surface mode peak is sufficiently reliable. In subsection 2.5.3, we have seen that the surface modes in quantum dots can be described like surface modes of a dielectric sphere of arbitrary radius. It turns out that the surface modes frequencies ω_{srf} are quantized according to a quantum number l with $1 < l < \infty$. The mode with $l = 1$, due to its dipolar charge fluctuation, it is reckoned to be the most intense [10, 59]. The intensity of this mode would be thus strongly dependent from the light polarization. However, since the nanoparticles are randomly orientated in the sample, the polarization is not mode selective. The modes with $l > 1$ also depend from the light polarization, but their dependence decrease progressively at the increasing of l. Conversely, for $l = \infty$, the mode are highly localized on the surface and it is fully independent from polarization. Based on what discussed above and in subsection 2.5.3, the experimentally observed SO mode is expected to be the one with $l = 1$. In figure 2.13 are reported the surface phonon frequencies for a dielectric sphere (CdS) in dependence of l. One can observe that for $l = 1$, the expected frequency is $\omega_{SO} = \omega_{l=1} \simeq 298$ cm^{-1}, a value quite far from the experimental value ($\omega_{SO} \simeq 270$ cm^{-1}). Nevertheless, it must be considered that in the calculation $\varepsilon_m = 1$ was assumed, i.e. the quantum dots were considered to have a free surface. In reality, the quantum dots samples are coated by a thin layer of organic molecules, thioglycolic acid in this case. Therefore it would be thus necessary to use a more realistic value of ε_m instead of $\varepsilon_m = 1$ used here. In table 5.3 are reported the values of surface phonon frequency ω_l with $l = 1$ calculated using different values of arbitrary dielectric constants of the medium ε_m. These values have been calculated using equation 2.41 with $l = 1$. It is evident that the surface phonon frequency decreases at the increasing of ε_m. The calculated surface phonon frequencies reported in table 5.3 are consistent to what observed experimentally $\omega_{SO} \approx 270$ cm^{-1}. Moreover, the frequencies calculated by equation 2.41 have values closer to the experimental ω_{SO}, when ε_m=2.5 and 3 are used. These values of dielectric constant are indeed very close to the dielectric constant of the liquid thioglycolic acid $\varepsilon_{\mathrm{TGA}}$=2.26, which forms a thin coating layer on the nanocrystal surface. However, it is worth to point out that the dielectric constant of the coating layer is not exactly the $\varepsilon_{\mathrm{TGA}}$, since the density of TGA on the quantum dot surface is not the same as the liquid. Moreover, some residual TOPO is still present on the quantum dot surface which makes increase the ε_m of the coating. Unfortunately, equation 2.41 does not express explicitly the dependence of the surface frequency from the diameter of the nanoparticle.

5.5 Discussion

As discussed in chapter 3, there are essentially two strategies to grow quantum dots of different size. One strategy accounts to change the surfactant concentration (TOPO) at a given temperature and with a certain precursors concentration. The other strategy accounts to extract aliquots of solution during the growth (arrested growth). However, even in this case, the presence of TOPO is needed to moderate the growth. The first strategy would be of course the standard one, but to have a set of quantum dots samples obtained from a single growth, the second strategy is largely preferable. The reason for this preference is that if multiple growths are performed, even using materials with the same purity, the same precursors concentration and the same temperature of growth, fluctuations of stoichiometry and morphology may always occur. Since Raman spectroscopy is rather sensitive to these variables, especially to stoichiometry, the spectra will be affected by their unwanted effects. Therefore, even though only small amounts of material are obtainable, and the samples contain a lot of unreacted material to eliminate, the second strategy was chosen to carry out this study.
The investigation of phonon confinement in semiconducting quantum dots requires the knowledge of the nanoparticles size and their size distribution. For this reason, a large parte of the study was devoted to the measurement of these quantities by direct and indirect methods. As already reported in subsection 5.1.2, the direct method used is based on the statistical analysis of nanoparticles diameters directly measured on the TEM images. The center position of the size distribution is thus the average diameter determined by a continuous distribution function associated with the histogram. The nanoparticles diameters were measured exclusively on TEM images with an accelerating voltage of 280 kV. Nevertheless, this is not completely correct since the electrons diffraction changes at the varying of accelerating voltage (energy of electrons), and the size of the nanoparticle results to be slanted. Thus, to have a correct measure of the nanoparticles diameter, it would be necessary to take the same image spot with several voltages and correct the obtained diameters by a calibration curve. The size distribution, namely σ should be in first approximation not affected by effects of electron diffraction. This is substantially true since the distribution is absolute, i.e. it does not change at the varying of its center position, $\bar{d}$ for instance. However, the size distribution is affected by other factors and results to be much broader than the one estimated from absorption measurements. As already discussed in subsection 5.1.2, the background noise in the TEM images introduces uncertainty in the measurement of nanoparticle diameters. The filtering of the image reduces the noise and helps to distinguish better the nanoparticles contours. However, it may in turn introduce further errors due to the possible cutting of pixels belonging to the nanoparticle, and due to the algorithm used to modify the image. Another source of error in the evaluation of nanoparticles diameter is their intrinsic morphology. In subsection 3.3.4, it was shown how the shape of a single II-VI nanocrystal is not spherical, rather it is a hexagonal prism capped with two hexagonal frustums. Moreover, the length of the prism may vary from particle to particle (see figure 3.5). It would be thus more correct to provide a distributions for each diameter, one for the long axis and one for the short axis of the nanocrystal, as well as of the shape distribution, e.g. the distribution of the ratio between the minor and major diameters. However, this more accurate statistical analysis was not possible to perform because of the random orientation of nanoparticles in the organic matrix. In conclusion, to have a more reliable statistic, it would be necessary to have a monolayer of nanoparticle on a suitable substrate, for example highly oriented pyrolytic graphite (HOPG) or to bind the quantum dots covalently on a gold substrate (by sulfur bonds). Moreover, to improve the statistic, it would be necessary to calibrate the val-

ues of quantum dot diameters by the acquisition of the images of the same area with different voltages.

The absorption spectroscopy revealed to be a technique of simple application for this type of material which provides at the same time excellent results. It was a fundamental tool to determine the mean size of nanocrystals, as well as to get an estimation of their size distribution. In figure 5.9, the dependence of the energy of the $1S_{3/2}1s$ transition from the time of growth can be observed. In particular, the growth rate is extremely rapid during the early stages of the growth, while it suddenly drops after two minutes. This behavior can be better visualized in the plot of time of growth dependence of the photoluminescence band wavelength. In figure 5.14, λ_{PL} was plotted versus the time of growth starting from the instant of sulfur-1-ODE mixture injection. It is clearly visible the condenser charge-like function behavior followed by the experimental data. The asymptotic value λ_∞ is the photoluminescence center peak of the quantum dots at the end of the growth, i.e. when all the precursors have been consumed and had provided material for the nanocrystals accretion. This suggests that just after the sulfur injection, the size selection by aliquots extraction is difficult to obtain since the nanoparticles grow very rapidly at this stage, see section 3.2.2. Experimentally, it was found that the time necessary for an aliquot extraction ($\sim$60 s) is comparable or even longer than the time taken by the growth to become nearly stationary. Furthermore, the extraction of aliquots during the nearly-stationary growth does not produces instead a big difference among the nanocrystals diameters. The five samples studied here are a clear example of this situation, where the sample 1 was extracted during the fast growth phase and has a diameter much smaller than sample 2, while the other four samples were extracted during the nearly stationary phase and their diameters do not differ too much. For this reason, it was not possible to extract aliquots of solution between the first (30 s) and the second extraction (120 s). Furthermore, a defocusing of the size distribution is observed with longer growth times. This results mainly in the broadening of $1S_{3/2}1s$ absorption peak. This nanoparticles size coarsening is caused essentially by the Ostwald ripening process occurring already when a quite large amount of nanocrystals is formed. At this stage of the growth, the Ostwald ripening causes a partial dissolution of the smallest nanoparticles and an accretion of the largest resulting in a broadening of the size distribution. The average diameter of the nanoparticle was estimated also from the photoluminescence emission band. However, the obtained values can not be considered as reliable as the values obtained by absorption. This is because the energy of the PL peak does not match exactly the band-gap energy, yet it is red-shifted of δE. For CdS, this shift is of $\sim$150 eV, nevertheless, it is just an estimated value that may introduce uncertainty in the evaluation of $\bar{d}$. The estimation of $\bar{d}$ by the energy of photoluminescence band becomes rather important when the absorption measurements are not available, or when the $1S_{3/2}1s$ peak is extremely broadened (large time of growth) and a too large uncertainty in the energy values holds.

In subsections 5.2.1 and 5.2.2, it was described how to obtain the size distribution from the width of absorption and photoluminescence peaks. In both case, it was of fundamental importance to eliminate the instrumental and the thermal contribution to the broadening. Comparing the widths obtained by the three methods, statistic on TEM images, absorbance and photoluminescence, it is clear how the width σ_{TEM} obtained by the statistical analysis on TEM images, is much larger than the values obtained by the other two techniques. Conversely, comparable σ was obtained by absorption and photoluminescence measurements. The large difference between σ_{TEM} and the σ_{Abs}-σ_{PL} could be attributed to the huge difference in the number of particles involved in the statistics. σ_{TEM} is indeed relative to a statistic done on a sample of $\sim$100 nanoparticles, while for σ_{Abs} and σ_{PL} the number of quantum dots involved in the statistic

is extremely larger. This will result in a focusing of the size distribution. However, for sure also the size distribution obtained by absorption and PL may contain uncertainties due to neglecting of the inhomogeneities and chemical fluctuations broadenings or to the rough estimation of the thermal and instrumental broadenings. In conclusion, the σ's obtained by the optical techniques are more reliable for the reasons explained above, and among them, the values of σ_{Abs}'s are expected to be more reliable. This because in the PL emission of quantum dots, a selective excitation may occur (hole burning) causing the partial depletion of a part of the PL peak [43]. The Raman scattering measurements provided interesting results, yet not always in accordance with what was expected and with the existing theory. The first Raman measurement were carried out on as grown stearic acid-coated CdS quantum dots sample drop casted on microscope glass, using an exciting wavelength of 514 nm. In spite of the encouraging initial result obtained with this sample, the successive measurements performed on the TOPO-coated CdS quantum dots samples did not given significative results. The main problem encountered was to find an area of the sample with a sufficiently intense Raman signal. This difficulty was due to the non elevate concentration of quantum dots in the gel mainly made up by organic material (TOPO, stearic acid, cadmium stearate). Another problem affecting these measurements was the decaying of signal caused by the gel melting and stirring operated by unavoidable laser heating of the sample. Moreover, when the laser power was too high, it even ended up damaging the sample. Finally, the use of 514 nm as exciting wavelength makes fall the Raman and photoluminescence signals in the same spectral region, resulting in a partial coverage of the Raman signal by the photoluminescence band. In order to overcome this last hitch, other laser lines (457 nm and 364 nm) were used. By using an exciting wavelength $\lambda_{exc} = 457$ nm, the photoluminescence background was partially reduced while it was completely removed when a UV laser line $\lambda_{exc} = 364$ nm was used. Nonetheless, in both cases the problems of signal decay or absence of signal still persisted. One try to solve this problem was to increase the volume of the scattering area, i.e. lowering the spatial resolution from $\sim$1 μm to some hundreds of micrometers (*macro*-Raman). This allowed to use much higher laser power, thus to get a stronger signal. By the *macro*-Raman configuration of the optical setup, Raman spectroscopy where performed on quantum dots in a chloroform and/or hexane solution loaded in a quartz cuvette with a 90 degrees scattering geometry. Yet, also in this case, using both visible either UV light, any quantum dots Raman signal were detected, probably again due to the low concentration of scattering bodies (CdS nanocrystals). Moreover, a large signal from the solvents was present. It was thus quite clear that the lack of signal was due principally to the low concentration of the scattering nanocrystal. The nearly complete elimination of thick organic layer made up mainly by trioctylphosphine oxide was indeed the solution of the problem. The first trial in this sense was to prepare pyridine coated CdS quantum dots according to the procedure described in chapter 3. However, the pyridine-CdS quantum dots samples still presented a waxy aspect, probably due to the not complete TOPO or stearic acid replacement, and during the Raman measurements the same problems occurred in TOPO-CdS Raman measurements were experienced. The Raman measurements performed on thioglycolic acid coated quantum dots was instead successful. The short and highly polar TGA molecules make the quantum dots be much more closely packed, thus a higher number of nanocrystals will be present in the same volume giving rise to a stronger signal. Moreover, the material does not melt easily with laser heating allowing the Raman signal to be stable in time. The first set of measurements on TGA-CdS quantum dots were performed using an exciting wavelength of 514 nm (2.4 eV). With this exciting energy, no resonance enhancement can be obtained since the band gap of the studied quantum dots ranges from 2.7 eV to 3 eV. Therefore, one finds out that only with elevate laser power, a sufficiently intense Raman signal could be

obtained. In these experiments, the lowest power used was of 100 mW, below such value no Raman signal was detected. Yet, the resulting spectra were affected by a strong thermal effect which could not be minimized, even using the correlation diagrams, and the phonon frequencies values were not reliable. The use of a much lower laser power, for instance far below 1 mW, reduced or at least minimized the problem of sample heating. The use of an high energy exciting laser line causes an intensity enhancement due to the resonant scattering which allows to use lower exciting light power. A higher enhancement would be obtained by UV light (364 nm), but in this case, a rearrangement of the optical setup would be necessary and plasma lines are not easily removable. Hence, the best compromise was to use $\lambda_{exc} = 457$ nm (2.7 eV) which can still produce an intensity enhancement especially in largest quantum dots, where the band gap is better matched by the laser line energy. With these conditions, the Raman spectra was obtained quite easily using laser powers between 70 μW and 35 μW. The obtained spectra have a good signal to noise ratio which allows to determine by multipeak fit the positions of the peaks with a good accuracy. Unfortunately, a quite strong photoluminescence background is always present in the spectra which partially hides some spectra details. However, in spite of this photoluminescence background, it is possible to recognize in every spectra a shoulder on the LO and 2LO peaks caused by the presence of another peak.
In figure 5.22 is shown the comparison between the theoretically predicted (continuum theory) and experimental phonon frequencies data. It is evident immediately that there is a not very good accordance between theory and experiment, in particular for the largest nanoparticles. First of all one can observe that size dependence of experimental ω_{LO} data is similar to an exponential function, while the theory says that the phonon frequency value grows similarly to $\sqrt{1 - R^{-2}}$, where R is the radius of the quantum dots. For samples 1 and 2, growth time 30 s and 120 s, the experimental values of ω_{LO} lie below the theoretical curve. Admitting the continuum model to be correct, in these two cases the discordance can be explained by the possible residual anharmonic effect due to the sample heating. In fact, although the use of correlation diagrams, anharmonic effect could be still present since for these samples a slightly higher laser power was used (70 μW). The experimental ω_{LO} value of sample 3 (growth time 180 s) is in a good accordance with theoretical data, even though the error in this case is rather large due to the multipeak fit performed on a noisy spectrum. In samples 4 and 5, growth times 360 s and 480 s respectively, the experimental data are not in good agreement with the theory. Here, the anharmonic effect can not be invoked otherwise, if present, it produced a frequency red shift. Conversely, the experimental ω_{LO} frequencies are blue-shifted with respect to theoretically predicted data. A much better accordance with the experimental values of $\omega_{2LO}/2$ does exist instead. In this case, except for the frequency of sample 5, the experimental points matches fairly well the phonon frequencies calculated by continuum model. A possible explanation for this better accordance is that the double phonon process is more selective, thus the influence of any possible cause affecting the LO phonon frequency will result to be reduced. However, to confirm this hypothesis further experiments would be necessary.
According to [16, 17, 23, 24], the peak which gives rise to a shoulder on the LO and 2LO peaks can be interpreted as a surface mode. The nanostructures, in particular the quantum dots have an elevate surface-volume ratio, thus the contribution of surface is expected to be relevant. The surface modes in nanostructure can be seen also as an effect of the quantum confinement since bulk and surface vibrations can be done distinguished anymore. In subsection 2.5.3, by using the plane dielectric-vacuum interface dispersion relation, an estimation of the surface phonon wavevector was obtained. This calculation was done in order to verify whether the periodicity of the mode, which is inversely proportional to the wavevector, has the order of magnitude of

the nanostructure. This can be useful to establish whether a relation between the nanoparticle size and the frequency of the surface phonon does exist. Inserting the numerical values, a periodicity in the order of 1-2 nm results. This periodicity is in the order of magnitude of the size of the studied quantum dots. From the comparison between the theoretical surface modes frequencies calculated by equation 2.41 ($l = 1$), and the experimental frequencies, one observes that comparable values can be obtained only with values of the medium dielectric constant ε_m of about 2-2.5. This value is very close to the dielectric constant of the liquid thioglycolic acid $\varepsilon_{\mathrm{TGA}} = 2.25$. Therefore, even though the layer of thioglycolic acid on the quantum dots surface is very thin, it is able to strongly affect the surface phonon frequency. However, one must consider that a small percentage of TOPO is still present on the quantum dot surface that will make increase the dielectric constant of the medium.

Chapter 6

Summary

In conclusion, cadmium sulfide quantum dots grown by colloidal chemistry methods were studied by Raman scattering, absorbance and photoluminescence spectroscopies and the morphology were characterized by transmission electron microscopy (TEM).
To produce cadmium sulfide nanocrystals a relatively simple and efficient method of growth was developed. Thjis method does not require the use of expensive and air sensitive sulfur precursors, as well as of organic phosphines. By this method, in only one growth procedure (aliquots extractions), nanocrystals with very small diameter (3 nm $\lesssim \bar{d} \lesssim$ 5 nm) were grown. This synthesis can be however still improved in order to obtain quantum dots with a narrower size distribution and a more uniform shape. One problem affecting this synthesis was the use of a poorly soluble cadmium precursor (cadmium stearate) which resulted to be very hard to eliminate during the purification phase. For this purpose, the use of shorter chain fatty acid-cadmium compound will solve the problem (e.g. cadmium myristate). Several trials were also done to reduce the injection time and the quantum dots extraction time in order to further reduce the size distribution. However, these improvements were not used to grow the sample studied here. The absorption and photoluminescence spectroscopies were used to study the electronic properties. Moreover, exploiting the relationship existing between the size and the band gap, from the energy of the first absorption transition, obtained by absorption spectroscopy measurements, the quantum dots mean diameters were determined. The same calculation was done using the energy of the photoluminescence band. From the width of absorption and photoluminescence, an estimation of the quantum dots diameters distribution was obtained. Transmission electron microscopy (TEM) images of the TOPO-CdS quantum dots samples were acquired to determine their morphology as well as the size distribution by a statistical analysis. Unfortunately, the presence in the samples of the trioctylphosphine oxide coating layer produced a strong noisy background in the images. This problem could be solved in the future performing TEM on quantum dots coated with short molecules ligands, e.g. thioglycolic acid, pyridine or thiophenol. Even better results can be obtained depositing a monolayer of quantum dots on a substrate. From the comparison between the width of size distribution measured by the three means, large differences appear. The widths obtained by absorption and photoluminescence measurements result in average the half of the width obtained by statistical analysis on TEM images. This fact was explained by the higher statistical significance in absorption and photoluminescence measurements, due to the much larger number of nanoparticles involved in the statistic with respect to TEM images.
Micro Raman measurements were performed on CdS quantum dots grown with different average sizes. The first measurements were carried out directly on as grown TOPO coated CdS

quantum dots drop-casted on a microscope glass. Due to the gel-like consistence of the material, it was extremely difficult to find a sufficiently strong and stable Raman signal. The quantum dots has thus treated to replace the TOPO coating layer with a short molecular chain. The molecules used for this purpose were pyridine and thioglycolic acid. The pyridine coated quantum dots still presented a waxy aspect and behaved similarly to TOPO-CdS. Successful Raman measurement were instead performed on the thioglycolic acid capped CdS quantum dots thanks to their powder-like consistence.

The micro-Raman measurements were performed using two exciting laser wavelength, 514 nm and 457 nm. The spectra obtained with λ_{ex} =514 nm were affected by thermal effects due to the high laser power used $\sim$10 mW, necessary to get a reasonably signal. With λ_{ex} =457 nm (2.7 eV), being the exciting radiation energy closer to the absorption band, a certain resonant effect was obtained producing a better signal to noise ratio. This allowed to use much lower laser powers ($\sim$ 30-40μW) minimizing the thermal effects. The thermal effect were further minimized selecting by a correlation diagram the spectra with the smallest thermal contribution. By using an UV exciting laser line, it will be perhaps possible to better distinguish the hidden details of the spectra, since in this case the spectral Raman scattering spectral range will be far from the photoluminescence emission. The same result might be obtained also using a low energy laser line ($\lambda_{exc} = 632$ nm), but in this case there will be any resonance effect.

Besides an asymmetric broadening of the peak, the Raman spectra show a clear size dependence of the LO and 2LO phonon frequencies. In every spectra, an additional peak, which is not present in CdS bulk spectra appears at $\sim$270 cm^{-1}. By the comparison of the experimental data with theoretical calculations (dielectric continuum model), it turns out that a not there is a not good agreement between the experimental LO peak frequency and the theoretical prediction. Nevertheless, a better agreement between the half frequency of the second order phonon process ω_{2LO}/2 and the theoretical prediction is observed. The peak occurring at $\sim$270 cm^{-1} is not be well described by the continuum model. Conversely, interpreting it as a surface mode (SO), the theory provides values of surface phonon frequencies reasonably close to the experiment. However, no explicit nanoparticle diameter dependence of the surface phonon frequency was found.

Future development of this kind of study will consist in the Raman spectroscopy of CdS quantum dots embedded in a polymeric matrix and compare the results with the TGA coated CdS quantum dots. A challenging project is then to perform a single quantum dot Raman and PL spectroscopy. This can be done depositing a quantum dots monolayer covalently bound to a substrate, and collect the weak signal which is enhanced placing a metallic nanometric tip on a single nanostructure, apertureless scanning near-field optical microscope (aSNOM) [119]. The Raman setup is actually equipped to perform these nanometer spatial resolution spectroscopies, namely *nano*-Raman and *nano*-PL, but it still needs further development and improvements to be fully operative. The same kind of study carried out in this thesis can be extended also to quantum dots of other materials such as CdSe or CdTe, ternary compounds (e.g. CdS_xSe_{1-x}) or nanostructured chalcopyrites, ($CuIn_xGa_{1-x}Se_2$ with $1 < x < 0$). These materials are viewed as very interesting material for photovoltaic applications [120], and recent reports show that is possible to grow them even by colloidal methods [121, 122].

Chapter 7

Acknowledgements

I would like to thank all the guys of my research group (NOL), in particular Prof. Wolfgang Richter and Eugen Speiser for the transmitted experience and know how. All the guys of the mechanical workshop for the realization of custom designed mechanical components. Silvia Masala of ENEA of Portici (NA) and fellows at the Department of Chemistry of University of Salerno for absorbance and photoluminescence measurements. Casalboni research group at Department of Physics of University of Roma Tor Vergata for absorbance measurements. People of ISPESL of Monteporzio Catone (RM) for nice TEM pictures of quantum dots. Finally, my beloved girlfriend Annalisa for her important psychological support, during hard times, and not only.

Bibliography

[1] C. B. Murray, D. J. Norris, and M. G. Bawendi. Synthesis and characterization of nearly monodisperse CdE (E = sulfur, selenium, tellurium) semiconductor nanocrystallites. *J. Am. Chem. Soc.*, **115**:8706–8715, 1993.

[2] M. C. Schlamp, X. Peng, and A. P. Alivisatos. Improved efficiencies in light emitting diodes made with CdSe/CdS core/shell type nanocrystals and a semiconducting polymer. *J. Appl. Phys.*, **82**:5837–5842, 1997.

[3] Y. Shen and Y. Lee. Assembly of CdS quantum dots onto mesoscopic TiO_2 films for quantum dot-sensitized solar cell applications. *Nanotechnology*, **19**:045602–045609, 2008.

[4] S. Biswas, M.F. Hossain, and T. Takahashi. Fabrication of Grätzel solar cell with TiO_2/CdS bilayered photoelectrode. *Thin Solid Films*, **517**:1284–1288, 2008.

[5] M. Bruchez, M. Morrone, P. Gin, S. Weiss, and A. P. Alivisatos. Semiconductor nanocrystals as fluorescent biological labels. *Science*, **281**:2013–2016, 1998.

[6] Y. Kayanuma. Wannier exciton in microcrystal. *Sol. State Comm.*, **59**:405–408, 1986.

[7] H. Fu, V. Ozolins, , and A. Zunger. Phonons in GaP quantum dots. *Phys. Rev. B*, **59**:2881–2887, 1999.

[8] W. Cheng, S. Ren, and P. Y. Yu. Theoretical investigation of the surface vibrational modes in germanium nanocrystals. *Phys. Rev. B*, **68**:193309, 1999.

[9] M.P. Chamberlain, C. Trallero-Giner, and M. Cardona. Theory of one-phonon Raman scattering in semiconductor microcystallites. *Phys. Rev. B*, **51**:1680–1693, 1995.

[10] S. Hayashi. Optical studiy of electromagnetic surface modes in microcrystals. *Jap. J. App. Phys.*, **23**:665–676, 1984.

[11] H. Richter, Z. P. Wang, and L. Ley. Raman spectroscopy of optical phonons confined in semiconductor quantum dots and nanocrystals. *Solid State Commun.*, **39**:625, 1981.

[12] W. S. 0. Rodden, C. M. Sotomayor Torres, and C. N. lronside. Three-dimensional phonon confinement in CdSe microcrystallites in glass. *Semicond. Sei. Technol.*, **10**:807–812, 1995.

[13] C. Raptis, D. Nesheva, Y. C. Boulmetis, Z. Levi, and Z. Aneva. Exciton related resonant Raman scattering from CdSe quantum dots in an amorphous GeS_2 thin film matrix. *J. Phys.: Condens. Matter*, **16**:8221–8232, 2004.

[14] S. V. Karpov, G. K. Muzafarova, and M. A. Yastrebova. Quantum Confinement Effect in the Vibrational Spectrum of CdS_xSe_{1-x} Quantum Dots in a Fluorophosphate Glass Matrix. *Phys of. the Sol. State*, **43**:1169–117, 2001.

[15] Yu M. Azhniuk, A. G. Milekhin, A. V. Gomonnai, V. V. Lopushansky, V. O. Yukhymchuk, S. Schulze, E.I. Zenkevich, and D. R. T. Zahn. Resonant Raman scattering studies of $Cd_{1-x}Zn_xS$ nanocrystals. *J. Phys.: Condens. Matter*, **16**:9069–9082, 2004.

[16] Yu M. Azhniuk, A. V. Gomonnai, V. V. Lopushansky, Yu I. Hutych, I. I. Turok, and D. R. T. Zahn. Resonant Raman scattering studies of $Cd_{1-x}Zn_xS$ nanocrystals. *J. Phys.: Conf. Series*, **92**:012044, 2007.

[17] V. M. Dzhagan, M. Ya Valakh, A. E. Raevskaya, A. L. Stroyuk, S. Ya Kuchmiy, and D. R. T. Zahn. Size effects on Raman spectra of small CdSe nanoparticles in polymer films. *Nanotechnology*, **19**:305707, 2008.

[18] A. E. Raevskaya, A. L. Stroyuk, S. Ya Kuchmiy, V. M. Dzhagan, M. Ya Valakh, and D. R. T. Zahn. Optical study of CdS- and ZnS-passivated CdSe nanocrystals in gelatin films. *J. Phys.: Condens. Matter*, **19**:386237, 2007.

[19] Yu M. Azhniuk, V. M. Dzhagan, A. E. Raevskaya, A. L. Stroyuk, S. Ya Kuchmiy, M. Ya Valakh, and D. R. T. Zahn. Optical studies of CdSe/HgSe and $CdSe/Ag_2Se$ core/shell nanoparticles embedded in gelatin. *J. Phys.: Condens. Matter*, **20**:455203, 2008.

[20] R. Kostic and N. Romcevic. Raman spectroscopy of CdS nanoparticles. *Phys. Stat. Sol. c*, **1**:2646–2649, 2004.

[21] J.J. Shiang, S.H. Risbud, and A.P. Alivisatos. Resonance Raman studies of the ground and lowest electronic excited state in CdS nanocrystals. *J. Chem. Phys.*, **98**:8433–8442, 1993.

[22] A. Milekhin, M. Friedrich, D.R.T. Zahn, L. Sveshnikova, and S. Repinsky. Optical investigation of CdS quantum dots in Langmuir-Blodgett films. *Appl. Phys. A*, **69**:97–100, 1999.

[23] J. Pan, X. Xu, S. Ding, and J. Pen. Raman scattering of CdS microcrystals in organic media. *J. of Lum.*, **45**:45–47, 1990.

[24] Y. Hwang, S. Park, and D. Kim. Size-dependent surface phonon mode of CdSe quantum dots. *Phys. Rev. B*, **59**:7285–7288, 1999.

[25] A. G. Rolo and M. I. Vasilevskiy. Raman spectroscopy of optical phonons confined in semiconductor quantum dots and nanocrystals. *J. of Raman Spettr.*, **38**:618–633, 2007.

[26] E. S. Rittner and J. H. Schulman. Studies on the coprecipitation of cadmium and mercuric sulfides. *J. Phys. Chem.*, **47**:537–543, 1943.

[27] U. Venkateswaran, M. Chandrasekhar, and H. R. Chandrasekhar. Luminescence and Raman spectra of CdS under hydrostatic pressure. *Phys. Rev. B*, **30**:3316–3319, 1984.

[28] T. Suzuki, T. Yagi, S. Akimoto, T. Kowamura, S. Tayoda, and S. Endo. Compression behavior of CdS and BP up to 68 GPa. *J. Appl. Phys.*, **54**:748–751, 1983.

[29] A. N. Mariano and E. P. Warekois. High pressure phases of some compounds of groups II-VI. *Science*, **142**:672–673, 1963.

[30] W. Richter. *Resonant Raman Scattering in Semiconductors*. Springer tracts in modern physics, Springer-Verlag, Berlin, Heidelberg, New York,: Hoeler, 1976.

[31] S. Ninomiya and S. Adachi. Optical properties of wurtzite CdS. *J. Appl. Phys.*, **78**:1183–1190, 1995.

[32] D.R.T. Zahn, G. Kudlek, U. Rossow, A. Hoffmann, I. Broser, and W. Richter. Phase transition from the cubic to the hexagonal modification in thin CdS films on InP(110). *Adv. Mater. Opt. Electron.*, **3**:11–14, 1994.

[33] A. Baldareschi and N. C. Lipari. Energy Levels of Excitons Semiconductors with Degenerated Bands. *Phys. Rev. B*, **3**:439–451, 1971.

[34] D. Vogel, P. Krueger, and J. Pollmann. Self-interaction and relaxation-corrected pseudopotentials for II-VI semiconductors. *Phys. Rev. B*, **54**:5495–5511, 1996.

[35] O. V. Farberovich, S. I. Kurganskii, and E. P. Domashevskaya. Problems of the opw method ii. calculation of the band structure of ZnS and CdS. *Phys. Stat. Sol.*, **97**:631–640, 1980.

[36] J. P. Elliot and P. G. Dawber. *Symmetry in Physics, volume 1: Principles and Simple Applications.*, volume **1**. Macmillan Publisher Ltd, 1st edition edition, 1984.

[37] F. Gao, Q. Lu, S. Xie, and D. Zhao. A Simple Route for the Synthesis of Multi-armed CdS Nanorods-Based Materials. *Adv. Mat.*, **14**:1537–1540, 2002.

[38] W. W. Yu, Y. A. Wang, and X. Peng. Formation and Stability of Size-, Shape-, and Structure-Controlled CdTe Nanocrystals: Ligand Effects on Monomers and Nanocrystals. *Chem. Mater.*, **15**:4300–4308, 2003.

[39] Q. Li, B. Sun, I. A. Kinloch, Dan Zhi, H. Sirringhaus, and A. H. Windle. Enhanced self-assembly of pyridine-capped CdSe nanocrystals on individual single-walled carbon nanotubes. *Chem. Mater.*, **18**:164–168, 2006.

[40] M. A. Nusimovici, M. Balkanski, and J. L. Birman. Lattice dynamics of wurtzite CdS II. *Phys. Rev. B*, **1**:596–602, 1970.

[41] R. J. Briggs and A. K. Radmas. Piezospectroscopic study of the Raman spectrum of cadmium sulphide. *Phys. Rev. B*, **13**:5518–5529, 1976.

[42] P. Y. Yu and M. Cardona. *Fundamentals of Semiconductors*. Springer-Verlag, 1983.

[43] S. V. Gaponenko. *Optical Properties of Semiconductor Nanocrystals*. Cambridge University Press, 2005.

[44] L. E. Brus. Electron electron and electron hole interactions in small semiconductor crystallites: The size dependence of the lowest excited electronic state. *J. Chem. Phys.*, **80**:4403–4409, 1984.

[45] Y. Kayanuma. Quantum-size effects of interacting electrons and holes in semiconductor nanocrystals with spherical shape. *Phys. Rev. B*, **38**:9797–9804, 1988.

[46] H. M. Schmidt and H. Weller. Quantum size effects in semiconductor crystallites: Calculation of the energy spectrum for the confined exciton. *Chem. Phys. Lett.*, **129**:615–618, 1986.

[47] T. Takagahara. Effects of dielectric confinement and electron-hole exchange interaction on excitonic states in semiconductor quantum dots. *Phys. Rev. B*, **47**:4569–4584, 1993.

[48] J. Xia. Electronic structure of zero-dimensional quantum well. *Phys. Rev. B*, **40**:8500–8507, 1989.

[49] M. Sweeny and J. Xu. Hole energy levels in zero-dimensional quantum balls. *Solid State Comm.*, **72**:301–304,, 1989.

[50] P. C. Sercel and K. J. Vahala. Analytical formalism for determining quantum-wire and quantum-dots band structure in the multiband envelope-function approximation. *Phys. Rev. B*, **42**:3690–3710, 1990.

[51] S.W. Koch, Y.Z. Hu, B. Fluegel, and N. Peyghambarian. Coulomb effects and optical properties of semiconductor quantum dots. *Journal of Crystal Growth*, **117**:592–597, 1992.

[52] D. J. Norris and M. G. Bawendi. Measurement and assignment of the size-dependent optical spectrum in CdSe quantum dots. *Phys. Rev. B*, **53**:16338–16346, 1996.

[53] J.J. Ramsden, S. E. Webber, and M. Grätzel. Luminescence of colloidal cadmium sulfide particles in acetonitrile and acetonitrile/water mixtures. *J. Phys. Chem.*, **89**:2740–2743, 1985.

[54] M.G. Bawendi, M.L. Steigerwald, and L. E. Brus. The quantum mechanics of large semiconductor clusters ("quantum dots"). *Annu. Rev. Phys. Chem.*, **41**:447–496, 1990.

[55] N. Chestnoy, T. D. Harris, R. Hull, and L. E. Brus. Luminescence and photophysics of cadmium sulfide semiconductor clusters: the nature of the emitting electronic state. *J. Phys. Chem.*, **90**:3393–3399, 1986.

[56] A. Uhrig, A. Wörner, C. Klingshirn, L. Banyai, S. Gaponenko, I. Lacis, N. Neuroth, B. Speit, and K. Remitz. Nonlinear optical properties of semiconductor quantum dots. *J. Cryst. Growth*, **117**:598–602, 1992.

[57] I.H. Campbell and P.M. Fauchet. The effects of microcrystal size and shape on the one phonon Raman spectra of crystalline semiconductors. *Sol. Stat. Comm.*, **58**:739–741, 1986.

[58] E. Roca, C. Trallero-Giner, and M. Cardona. Polar optical vibrational modes in quantum dots. *Phys. Rev. B*, **49**:13704–13710, 1994.

[59] Bo E. Sernelius. *Surface Modes in Physics*. WILEY-VCH Verlag Berlin GmbH, 2001.

[60] R. Ruppin. Surface Effects on Optical Phonons and on Phonon-Plasmon Modes. *Surf. Sci.*, **34**:20–32, 1973.

[61] K. Rajeshwar, N. R. de Tacconi, and C. R. Chenthamarakshan. Semiconductor-Based Composite Materials: Preparation, Properties, and Performance. *Chem. Mater.*, **13**:2765–2782, 2001.

[62] M. Chu and G. Liu. Synthesis of liposomes-templated CdSe hollow and solid nanospheres. *Mat. Lett.*, **60**:11–14, 2006.

[63] O. Palchik, R. Kerner, A. Gedanken, A. M. Weiss, M. A. Slifkin, and V. Palchik. Microwave-assisted polyol method for the preparation of CdSe "nanoballs". *J. Mater. Chem.*, **11**:874–878, 2001.

[64] I.N. Stranski and L. Von Krastanow. *Akad. Wiss. Lit. Mainz Math-Natur. K1 IIb*, **146**:797, 1939.

[65] M. Volmer and A. Weber. *Z. Phys. Chem.*, **119**:277, 1926.

[66] D. J. Eaglesham and M. Cerullo. Dislocation-Free Stranski-Krastanow Growth of Ge on Si(100). *Phys. Rev. Lett.*, **64**:1943, 1990.

[67] S. Ruffenach, B. Maleyre, O. Briot, and B. Gil. Growth of InN quantum dots by MOVPE. *Phys. Stat. Sol. (c)*, **2**:826–832, 2005.

[68] G. S. Huang, X. H. Tang, B. L. Zhang, Y. C. Zhang, and S. C. Tjin. LP-MOVPE growth of InAs quantum dots using tertiarybutylarsine (TBA) in pure N_2 ambient. *J. Crystal Growth*, **268**:444–448, 2004.

[69] N. Lovergine, M. Longo, A. M. Mancini, G. Leo, M. Mazzer, M. Berti, and A. V. Drigo. Stranski-Krastanow self-organized growth of nano-scale ZnTe islands on (001)GaAs by metalorganic vapour phase epitaxy. *J. Mat. Science: Mat. in Electr.*, **9**:249–253, 1998.

[70] C. Meyne, U. W. Pohl, W. Richter, M. Straßburg, A. Hoffmann, V. Türck, S. Rodt, D. Bimberg, and D. Gerthsen. Quantum island formation in CdS/ZnS heterostructures grown by MOVPE. *J. Crystal Growth*, **214/215**:722–726, 2000.

[71] A. M. Kapitonov, T. Itoh, U. Woggon, D. Kayser, and D. Hommel. Optical properties of epitaxially grown submonolayer CdSe/ZnSe nanostructures. *Phys. Rev. B*, **70**:195304, 2004.

[72] Z. Zhong and G. Bauer. Site-controlled and size-homogeneous Ge islands on prepatterned Si(001) substrates. *Appl. Phys. Lett.*, **84**:1922, 2004.

[73] C. B. Murray, C. R. Kagan, and M. G. Bawendi. Synthesis and characterization of monodisperse nanocrystals and close packed nanocrystal assemblies. *Annu. Rev. Mater. Sci.*, **30**:545–610, 2000.

[74] C. R. Bullen and P. Mulvaney. Nucleation and growth kineitcs of CdSe nanocrystals in octadecene. *Nano Lett.*, **4**:2303–2307, 2004.

[75] U. Winkler, D. Eich, Z.H. Chen, R. Fink, S.K. Kulkarni, and E. Umbach. Detailed investigation of CdS nanoparticle surfaces by high-resolution photoelectron spectroscopy. *Chem. Phys. Lett.*, **306**:95–102, 1999.

[76] A.L. Rogach, A. Kornowski, M. Gao, A. Eychmüller, and H. Weller. Synthesis and Characterization of a Size Series of Extremely Small Thiol-Stabilized CdSe Nanocrystals. *J. Phys. Chem. B*, **103**:3065–3069, 1999.

[77] A. Eychmüller and A.L. Rogach. Chemistry and photophysics of thiol-stabilized II-VI semiconductor nanocrystals. *Pure Appl. Chem.*, **72**:179–188, 2000.

[78] A. E. Raevskaya, A. L. Stroyuk, S. Ya. Kuchmiy, Yu. M. Azhniuk, V. M. Dzhagan, V. O. Yukhymchukc, and M. Ya. Valakh. Growth and spectroscopic characterization of CdSe nanoparticles synthesized from $CdCl_2$ and Na_2SeSO_3 in aqueous gelatine solutions. *Coll. and Surf. A: Physicochem. Eng. Aspects*, **290**:304–309, 2006.

[79] D. Berhanu, K. Govender, D. Smyth-Boyle, M. Archbold, D.P. Halliday, and P. O′Brien. A novel soft hydrothermal (SHY) route to crystalline PbS and CdS nanoparticles exhibiting diverse morphologies. *Chem. Commun.*, pages 4709–4711, 2006.

[80] C. Jiang, S. Xu, D. Yang, F. Zhang, and W. Wang. Synthesis of glutathione-capped CdS quantum dots and preliminary studies on protein detection and cell fluorescence image. *Luminescence*, **22**:430–437, 2007.

[81] W. Yang, W. Li, H. Dou, and K. Sun. Hydrothermal synthesis for high-quality CdTe quantum dots capped by cysteamine. *Mat. Lett.*, **62**:2564–2566, 2008.

[82] V. LaMer and R. Dinegar. Theory, production and mechanism of formation of monodispersed hydrosols. *J. Am. Chem. Soc.*, **72**:4847–4854, 1950.

[83] T. Sugimoto. Preparation of monodispersed colloidal particles. *Advances in Colloid and Interface Science*, **28**(1):65–108, 1987.

[84] L. Liu and S. H. Risbud. Quantum-dots size-distribution analysis and precipitation stages in semiconductor doped glasses. *J. Appl. Phys.*, **68**:28, 1990.

[85] E. E. Lees, M. J. Gunzburg, T. Nguyen, G. J. Howlett, J. Rothacker, E. C. Nice, A. H. A. Clayton, and P. Mulvaney. Experimental Determination of Quantum Dot Size Distributions, Ligand Packing Densities, and Bioconjugation Using Analytical Ultracentrifugation. *Nano Lett.*, **8**:2883–2890, 2008.

[86] I. M. Lifshitz and V. V. Slyozov. Kinetics of diffusive decay of supersaturated solid solutions. *J. Phys. Chem. Solids*, **19**:35, 1961.

[87] C. Z. Wagner. *Elektrochem.*, **65**:581, 1961.

[88] D. V. Talapin, A. L. Rogach, M. Haase, and H. Weller. Evolution of an ensemble of nanoparticles in a colloidal solution: Theoretical study. *J. Phys. Chem. B*, **105**:12278–12285, 2001.

[89] B. O. Dabbousi, J. Rodriguez-Viejo, F. V. Mikulec, J. R. Heine, H. Mattoussi, R. Ober, K. F. Jensen, and M. G. Bawendi. (CdSe)ZnS Core-Shell Quantum Dots: Synthesis and Characterization of a Series of Highly Luminescent Nanocrystallites. *J. Phys. Chem. B*, **101**:9463–9475, 1997.

[90] J. G. Amar and Fereydoon Family. Critical Cluster Size: Island Morphology and Size Distribution in Submonolayer Epitexyal Growth. *Phys. Rev. Lett.*, **74**:2066–2069, 1995.

[91] Y. Ebiko, S. Muto, D. Suzuki, S. Itoh, K. Shiramine, and T. Haga. Island Size Scaling in InAs/GaAs Self-Assembled Quantum Dots. *Phys. Rev. Lett.*, **80**:2650–2653, 1998.

[92] L. Qu, Z. A. Peng, and X. Peng. Alternative routes toward high quality CdSe nanocrystals. *Nano Lett.*, **1**:333–337, 2001.

[93] Z. A. Peng and X. Peng. Formation of high-quality CdTe, CdSe, and CdS nanocrystals using cdo as precursor. *J. Am. Chem. Soc.*, **123**:183–184, 2001.

[94] D. V. Talapin, I. Mekis, S. Goötzinger, A. Kornowski, O. Benson, and H. Weller. CdSe/CdS/ZnS and CdSe/ZnSe/ZnS core-shell-shell nanocrystals. *J. Phys. Chem. B*, **108**:18826–18831, 2004.

[95] X. Peng, M. C. Schlamp, A. V. Kadavanich, and A. P. Alivisatos. Epitaxial Growth of Highly Luminescent CdSe/CdS Core/Shell Nanocrystals with Photostability and Electronic Accessibility. *J. Am. Chem. Soc.*, **119**:7019–7029, 1997.

[96] W. W. Yu and X. Peng. Quantum dot bioconjugates for ultrasensitive nonisotopic detection. *Angew. Chem. Int. Ed.*, **41**:2368–2371, 2002.

[97] S. Pokrant and K.B. Whaley. Tight-binding studies of surface effects on electronic structure of CdSe nanocrystals: the role of organic ligands, surface reconstruction, and inorganic capping shells. *Eur. Phys. J. D*, **6**:255–267, 1999.

[98] J. E. Bowen Katari, V. L. Colvin, and A. P. Alivisatos. X-ray photoelectron spectroscopy of CdSe nanocrystals with applications to studies of the nanocrystal surface. *J. Phys. Chem.*, **98**:4109–4117, 1994.

[99] J. Taylor, T. Kippeny, and S. J. Rosenthal. Surface stoichiometry of CdSe nanocrystals determined by rutherford backscattering spectroscopy. *J. Cluster Science*, **12**:571–582, 2001.

[100] L. R. Becerra, C. B. Murray, R. G. Griffin, and M. G. Bawendi. Investigation of the surface morphology of capped CdSe nanocrystallites by ^{31}P nuclear magnetic resonance. *J. Chem. Phys.*, **19**:3297–3300, 1994.

[101] W. C. W. Chan and S. Nie. Quantum dot bioconjugates for ultrasensitive nonisotopic detection. *Science*, **281**:2016, 1998.

[102] N. Pradhan, D. M. Battaglia, Y. Liu, and X. Peng. Efficient, stable, small, and water-soluble doped ZnSe nanocrystal emitters as non-cadmium biomedical labels. *Nano Lett.*, **7**:312–317, 2007.

[103] S. F. Wuister, I. Swart, F. van Driel, S. G. Hickey, and C. de Mello Donega. Highly luminescent water-soluble CdTe quantum dots. *Nano Lett.*, **3**:503–507, 2003.

[104] A. M. Smith, H. Duan, M. N. Rhyner, G. Ruan, and S. Nie. A systematic examination of surface coatings on the optical and chemical properties of semiconductor quantum dots. *Phys. Chem. Chem. Phys.*, **8**:3895–3903, 2006.

[105] J. Rodriguez-Viejo, H. Mattoussi, J. R. Heine, M. K. Kuno, J. Michel, M. G. Bawendi, and K. F. Jensen. Evidence of photo- and electro-darkening of (CdSe)ZnS quantum dot composites. *J. Appl. Phys*, **87**:8526–8534, 2000.

[106] J. Aldana, Y. A. Wang, , and X. Peng. Photochemical instability of CdSe nanocrystals coated by hydrophilic thiols. *J. Am. Chem. Soc.*, **123**:8844–8850, 2001.

[107] C.V. Raman. A new radiation. *Indian Journal Of Physics*, **2**:387–398, 1928.

[108] C.V. Raman. A new type of secondary radiation. *Nature*, **121**:619–620, 1928.

[109] R. M. Martin and C. M. Varma. Cascade theory of inelastic scattering of light. *Phys. Rev. Lett.*, **26**:1241–1244, 1971.

[110] R. Zeyher. Theory of multiphonons Raman spectra above the energy gap in semiconductors. *Sol. Stat. Comm.*, **16**:49–52, 1975.

[111] R.C.C. Leite and S.P.S. Porto. Enhancement of Raman cross section due to resonant absorption. *Phys. Rev. Lett.*, **17**:10–12, 1970.

[112] M.L Williams and J. Smith. Multiple-phonon resonant Raman scattering theory. *Sol. Stat. Comm.*, **8**:2009–2011, 1970.

[113] H. Mathieu, T. Richard, J. Alkgre, P. Lefebvre, G. Arnaud, W. Granier, L. Boudes, J. L. Marc, A. Pradel, and M. Ribes. Quantum confinement effects of CdS nanocrystals in a sodium borosilicate glass prepared by the sol-gel process. *J. Appl. Phys.*, **77**:287–293, 1995.

[114] U. Banin, M. Bruchez, A. P. Alivisatos, T. Ha, S. Weiss, and D. S. Chemla. Evidence for a thermal contribution to emission intermittency in single CdSe/CdS core/shell nanocrystals. *J. Chem. Phys.*, **110**:1195–1201, 1999.

[115] C. Trallero-Giner, A. Debernardi, M. Cardona, E. Menéndez-Proupín, and A. I. Ekimov. Optical vibrons in CdSe dots and dispersion relation of the bulk material. *Phys. Rev. B*, **57**:4664–4669, 1998.

[116] B. Schreder, M. Schmitt C. Dem, A. Materny, W. Kiefer, U. Winkler, and E. Umbach. Raman spectroscopy of II-VI semiconductor nanostructures: CdS quantum dots. *J. of Raman Spettr.*, **34**:100–103, 2003.

[117] Z. V. Popovic, Z. Dohcevic-Mitrovic, A. Cros, and A. Cantarero. Raman scattering study of the anharmonic effects in CeO_{2-y} nanocrystals. *J. Phys.: Cond. Matt.*, **19**:496209, 2007.

[118] Y. Hwang, S. Shin, H.L. Park, S. Park, U. Kim, H.S. Jeong, E. Shin, and D. Kim. Effect of lattice contraction on the Raman shifts of CdSe quantum dots in glass matrices. *Phys. Rev. B*, **54**:15120–15124, 1996.

[119] E. Speiser, B. Buick, S. Del Gobbo, D. Calestani, and W. Richter. *Epioptics-9: Proceedings of the 39th Course of the International School of Solid State Physics*, page 82. The Science and Culture Series-Physics. World Scientific Co. Pte. Ltd., 2006.

[120] R. P. Raffaelle, S. L. Castro, A. F. Hepp, and S. G. Bailey. Quantum Dot Solar Cells. *Prog. Photovolt: Res. Appl.*, **10**:433–439, 2002.

[121] S. L. Castro, S. G. Bailey, R. P. Raffaelle, K. K. Banger, and A. F. Hepp. Nanocrystalline Chalcopyrite Materials ($CuInS_2$ and $CuInSe_2$) via Low-Temperature Pyrolysis of Molecular Single-Source Precursors. *Chem. Mater.*, **15**:3142–3147, 2003.

[122] H. Zhong, Y. Li, M. Ye, Z. Zhu, Y. Zhou, C. Yang, and Y. Li. A facile route to synthesize chalcopyrite $CuInSe_2$ nanocrystals in non-coordinating solvent. *Nanotechnology*, **18**:025602, 2007.